공학박사 학위논문

# Uplift Bearing Capacity and Failure Mechanism of Spread Foundations in Sand

## 모래지반에 설치된 확대기초의 인발지지력과 파괴 메커니즘

**2023년 2월**

서울대학교 대학원

건설환경공학부

구 교 영

# Uplift Bearing Capacity and Failure Mechanism of Spread Foundations in Sand

지도교수 김성렬

이 논문을 공학박사 학위논문으로 제출함

**2023 년 2 월**

서울대학교 대학원

건설환경공학부

구교영

구교영의 공학박사 학위논문을 인준함

**2023 년 2 월**

위 원 장 정충기 **(인)**

부위원장 김성렬 **(인)**

위 원 박준범 **(인)**

위 원 김현기 **(인)**

위 원 김재현 **(인)**

# Abstract

# Uplift Bearing Capacity and Failure Mechanism of Spread Foundations in Sand

Gu, Kyo-Young
Department of Civil & Environmental Engineering
The Graduate School
Seoul National University

The shallow foundation supporting the transmission tower is subjected to uplift load due to wind load and breakage of the transmission line. Power transmission towers are mainly installed in mountainous areas, and shallow foundations are mainly applied in consideration of accessibility and construction. Since the shallow spread foundation's margin of safety against uplift resistance is much smaller than that against compression, research for estimation of accurate uplift bearing capacity is important. Therefore, in this study, various centrifugal model experiments and symbolic regression analysis using machine learning techniques were performed to analyze the uplift behavior and uplift failure mechanisms of the foundation embedded in the sand.

In consideration of the realistic conditions, the experimental models target an individual shallow spread foundation of the tower legs, which is installed in sand. Tests of the full model in centrifuge were conducted under various conditions with the different sizes of the foundation and soil density. The ultimate state is reached even with a relatively small uplift displacement, and the load softening behavior is occurred after the peak load. In addition, scale effect on the uplift bearing capacity and peak displacement was confirmed according to the size of the foundation. The uplift bearing capacity became large as the embedment depth ratio and soil density increased. The vertical displacement of the ground surface due to uplift was measured and analyzed. The influence zone was proposed using the internal friction angle of the soil.

In order to analyze the characteristics of the uplift behavior, half-cut model tests in centrifuge were performed to analyze the failure mechanism inside the ground. Compared to the vertical displacement of the ground surface of the half-cut foundation model with the full one, it was determined that the two experiments had the same uplift behavior. Using the PIV technique, the failure surface was analyzed in consideration of the mobilization of the vertical displacement in the ground due to uplifting the foundation. The bilinear failure surfaces were proposed by adopting the symbolic regression analysis using the machine learning technique based on the internal friction angle of soil and the foundation size ground.

Finally, a semi-analytical solution for calculating uplift bearing capacity was proposed based on the limit equilibrium method and Coulomb’s theory. The proposed solutions adopted a slice method to estimate the shear resistance along the failure surface. The suggested solution was verified with the current centrifuge test results and previously published test results. The uplift bearing capacity was well predicted considering the foundation size and soil density. It is believed that it will be used for the preliminary design of the uplift bearing capacity proposed through the results of this study.

**Keywords: spread foundation of transmission tower; uplift bearing capacity; centrifuge test; failure surface; shear resistance**

**Student Number: 2018-34756**

# Contents

# List of Tables

# List of Figures

# Chapter 1. Introduction

## 1.1 Background

Transmission towers are important social infrastructure for supplying electricity. When a transmission tower is damaged, the economic and social problems cause significant cost and considerable time to restore it. Therefore, it is essential to prevent the destruction and secure a reasonable level of safety. To ensure the stability of the transmission tower, foundations are installed to support the tower. These foundation types include spread foundations, mat foundations, piles, and drilled shafts (IEEE, 2001).

Shallow foundations have been widely used to support the transmission towers according to their advantage in construction at less accessible areas, such as mountainous terrain, as shown in Fig. 1.1a. Cast-in-place concrete is usually applied to construct a shallow foundation with a width of several meters (Kananyan, 1966). This foundation type with a definite dimension, which is categorized as a spread foundation, is required to resist a combination of compressive, lateral, and uplift forces typically caused by the tower weight and the wind as shown in Fig. 1.1b and 1.1c (Kulhawy et al., 1983.). These forces are transferred to the bearing ground through the shaft and the slab of the spread foundation as shown in Fig. 1.1d (KEPCO, 2013). The combination of horizontal and vertical uplift forces can result in an inclined load on the spread foundation with an angle of less than 10° to the vertical line (Pacheco et al., 2008). By analyzing the behavior of inclined anchors subjected to inclined load, Roy et al. (2021) found that the interaction between the horizontal and vertical uplift forces to the foundation is insignificant when the inclination is smaller than 60°. Therefore, the resistance to the purely vertical uplift is mostly considered in the practical design of the spread foundation for the transmission tower.

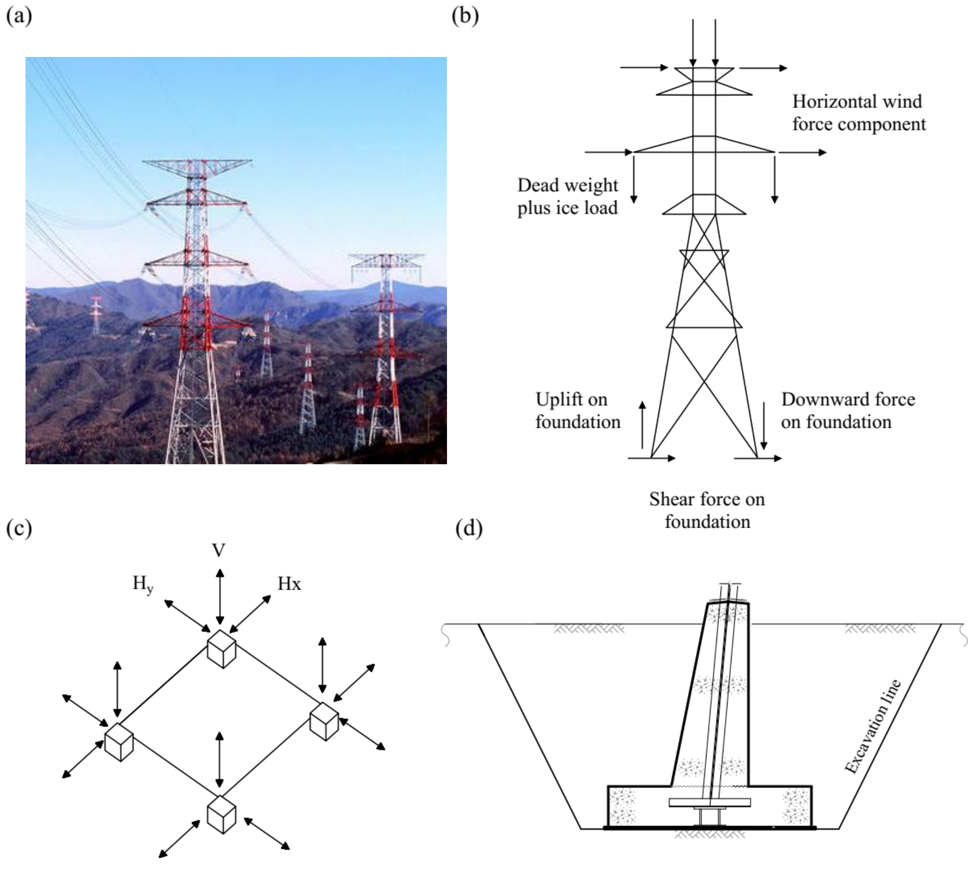

Fig. 1.1 Overview of transmission tower system: (a) transmission tower, (b) force on transmission tower(Kulhawy et al., 1983), (c) resultant force on foundations (Kulhawy et al. 1983), and (d) spread foundation (KEPCO 2013)

Figure 1.1b shows that ensuring the stability of the spread foundation under the resultant compression and uplift force is the main objective of the design in practice (Pacheco et al., 2008). Moreover, the focus should be on the uplift resistance because the margin of safety against uplift loading of the spread foundation is considerably smaller than that against compression (Ding et al., 2021).

The estimation of uplift bearing capacity for the practical design is required to cover 2 main characteristics such as (1) the uplift behavior of shallow foundations and (2) the failure mechanisms to determine shear resistance and soil weight within the failure surface. The uplift bearing capacity ($Q_u$) can be calculated by the sum of the foundation weight, the soil weight within the failure surface, and the resultant shear resistance along the failure surface and foundation slab, as shown in Fig. 1.2.

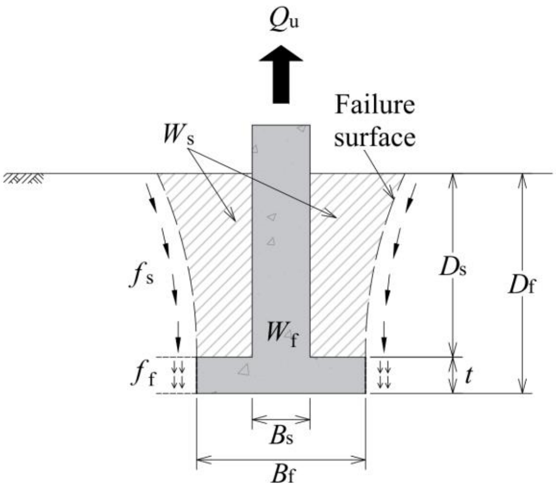

Fig. 1.2 Failure mechanism of spread foundation under uplift loading

Previous studies investigated uplift bearing behavior conducted by experimental model tests at specific g-level and numerical simulations. 1g experiments have been conducted to investigate the effects of embedment depth and relative density on the uplift behavior of anchor plates (Das & Jones, 1982; Ilamparuthi et al., 2002; Kulhawy et al., 1987; Liu et al., 2012; Meyerhof & Adams, 1968; Murray & Geddes, 1988; Sakai & Tanaka, 1998). Accordingly, several analytical formulations were proposed to calculate the uplift bearing capacity of plate anchors and shallow foundations from the 1g model test results. Several researchers have attempted to develop a theoretical method that considers shear resistance along and soil weight inside the failure surface. (Das & Jones, 1982; Deshmukh et al., 2010; Matsuo, 1967, 1968; Meyerhof & Adams, 1968)

However, the analysis based on 1g model test was subjected to the scale effect associated with low simulated stress conditions (Dickin, 1988; Ovesen, 1981; Sakai & Tanaka, 1998). Ovesen (1981) confirmed that the scale effect could be eliminated by reasonably simulating the in-situ stress condition and the ratio of the anchor diameter to the average median size of the soil particles, $D_{50}$.

Several failure surface models were suggested by previous researchers to analyze the uplift behavior and develop the analytical (Balla, 1961; Matsuo, 1967; Meyerhof & Adams, 1968). Typical failure surfaces are vertical, inclined and curved failure surface.

However, Cheuk et al. (2008) and Huang et al. (2015) revealed that the failure surface is a nearly straight line and curves outward near the ground surface through extensive analyses of 1 g and centrifuge test results. In their numerical analysis of the plate anchor under uplift loading, Roy et al. (2018) reported a similar shape of failure surface.

Notably, the linear failure surface may fail to capture different uplift failure mechanisms along the entire embedment depth appropriately, whereas the curved failure surface has been typically suggested from experiments involving foundations with limited dimensions and field stress condition. Existing solutions to these suggested failure surfaces require further verification with experimental data of reduced-scale models subjected to stress conditions similar to those in the field. On this basis, uplift model tests on large-scale and full-scale spread foundations are still necessary to understand the scale effect and supplement the verification of analytical and numerical calculations.

## 1.2 Research objectives

Based on the above discussion, the present study aims to investigate the uplift behavior of a shallow spread foundation in the cohesionless soil by conducting the centrifuge tests and developing the semi-analytical solutions. In summary, the main objectives of the present study are as follows:

(1) To analyze the uplift bearing capacity of the shallow spread foundation considering various influence factors;

(2) To investigate the influence zone of shallow spread foundations in cohesionless soil under uplift loading;

(3) To characterize the failure surface using PIV a modern technique applicable to centrifuge tests;

(4) To propose the semi-analytical solution of uplift bearing capacity of the shallow spread foundation in cohesionless soil using machine learning technique.

## 1.3 Scope of work

Transmission tower foundation system consists of 4 foundations to support the tower. For the basic analysis, the present study targets a single foundation installed in cohesionless soil. A single spread foundation was used to analyze the tower-foundation system. It was assumed that uplift behavior of the single foundation is representative for the 4 foundations supporting the tower. The behavior of the foundation modeled in the experimental simulation and semi-analytical solution are limited to the following conditions.

- Dry uniform silica sand with loose and dense states was considered in analyses of the centrifuge tests and analytical solutions. The fully drained condition is appropriate for the sandy soil in consideration.
- Uplift behavior of spread foundation was analyzed under purely vertical uplift loading because the effect of the inclination of the uplift load was not significant based on preliminary test results.
- Failure mechanisms from half-cut centrifuge model test was assumed that it is representative to the mechanisms of full model test.

## 1.4 Thesis organization and structure

The dissertation comprises seven chapters which are briefly introduced as follows:

In chapter 1: the background, research objectives, scope of work and the structure of dissertation are presented.

In chapter 2: the literature review on the Experimental study and theoretical analysis about the uplift behavior of the shallow spread foundation in horizontal ground is described.

In chapter 3: the centrifuge experiments of full and half-cut model were generally presented. The soil properties and preparation of ground which used in centrifuge model tests were presented. The foundation model of roughness and manufacturing methods were summarized. In addition, the layout of the full and half-cut model tests in centrifuge were explained including the centrifuge machine, sensors, and actuators. Finally, the concept of the genetic analysis to suggest empirical formulation and PIV method to analyze failure mechanisms are introduced.

In chapter 4: the uplift behavior was discussed with the centrifuge test of full foundation model. Influence factors to the uplift bearing capacity and the corresponding displacement at peak load were introduced. The uplift resistance factor was used to explore the scale effect. The empirical equations of uplift resistance factor and peak displacement were proposed using the genetic analysis for symbolic regression. The influence zone was also hypothesized based on the ground surface's vertical displacement.

In chapter 5: the failure mechanisms were analyzed by adopting PIV methods. The bilinear failure surface was proposed by capturing the development of the failure surface. The characteristics of influence factors to the failure surface was investigated, which was used to suggest a new form of failure surface. Finally, the proposed failure surface was compared with the previously suggested failure surface according to the foundation geometry.

In chapter 6: the semi analytical solution for uplift bearing capacity was proposed based on the centrifuge test results. The proposed solutions adopted a slice method to estimate the shear resistance along the failure surface. The suggested solution was verified with the current centrifuge tests results and previously performed tests results.

In chapter 7: the main conclusions of the present study and suggestions for further researches are presented.

# Chapter 2.Literature review

## 2.1 Introduction

Numerous experimental and analytical studies have been conducted on the uplift behavior of the spread foundation. In addition, the suggestions on the anchor plate under uplift loading can be reasonably applied to the spread foundation

Experimental studies on the uplift resistance of shallow foundations have been conducted under normal gravity (1 g) and centrifugal acceleration conditions. These studies were mainly performed to understand the uplift behavior and formation of the failure surface under various conditions, such as different embedment depth ratios (ratio of the embedment depth to the foundation width) and soil types. The majority of small-scale experiments have been conducted on anchor plates under uplift loading (Das & Jones, 1982; Ilamparuthi et al., 2002; Kulhawy et al., 1987; Liu et al., 2012; Meyerhof & Adams, 1968; Murray & Geddes, 1987; Sakai & Tanaka, 1998). The small-scale test results were analyzed using a nondimensional method to compute the uplift bearing capacity by multiplying the weight of the soil above the foundation slab by a non-dimensional factor. Ovesen, (1981b) indicated that the analyses based on small-scale experiments are subject to a scale effect related to the nonlinear behavior of the soil according to different confining pressures. Several centrifuge studies were performed on foundations considering prototype dimensions and field stress conditions to minimize the scale effect (Dickin, 1988; Tagaya et al., 1988).

## 2.2 Experimental study

Numerous experimental and analytical studies have been conducted on the uplift behavior of the spread foundation. In addition, the suggestions on the anchor plate under uplift loading can be reasonably applied to the spread foundation (Das & Shukla, 2013).

1g experiments have been conducted to investigate the effects of embedment depth and relative density on the uplift bearing behavior of anchor plates (Das & Jones, 1982; Ilamparuthi et al., 2002; Kulhawy et al., 1987; Liu et al., 2012; Meyerhof & Adams, 1968; Murray & Geddes, 1988; Sakai & Tanaka, 1998). Accordingly, several analytical formulations were employed to calculate the uplift bearing capacity from the 1g model test results (Das & Jones, 1982; Matsuo, 1967, 1968; Meyerhof & Adams, 1968).

### 2.2.1 1g model experimental test

Das and Jones (1982) and Kulhawy et al. (1987)performed small-scaled model tests with an influence factor on the uplift bearing capacity such as different embedment depths and soil densities. The uplift bearing capacity increased with those variables. Furthermore, they adopted the uplift resistance factor $N_q$ which is normalized uplift bearing capacity in order to analyze test results. The Native soil density had a substantial effect on uplift bearing capacity with deeper embedment depth and backfill density.

$$N_q = \frac{Q_{\mathrm{net}}}{\gamma B_{\mathrm{f}}^2 D_{\mathrm{s}}} = \frac{Q_{\mathrm{u}} - W_{\mathrm{f}}}{\gamma B_{\mathrm{f}}^2 D_{\mathrm{s}}} \tag{2.1}$$

where $Q_{\mathrm{u}}$=uplift bearing capacity, $Q_{\mathrm{net}}$=uplift net bearing capacity, $W_{\mathrm{f}}$=foundation weight, $B_{\mathrm{f}}$=slab width, and $D_s$=embedment depth from the top of the slab to the ground surface (Fig. 1.2).

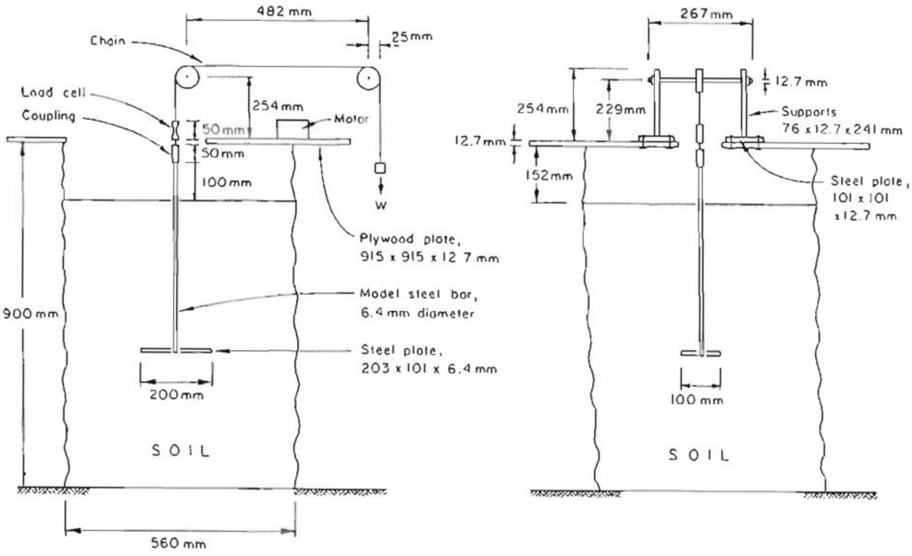

Fig. 2.1 Typical test layout of the model test in 1g by Kulhawy et al. (1987).

A similar conclusion was stated by Dickin (1988) through a centrifuge test on an anchor of a 1 m width. Figure 2.2 shows the layout a typical centrifuge model test. Tagaya et al. (1988) performed a series of centrifuge tests on an anchor plate with a diameter of 2.6–4.7 m in dense sand. They suggested that the normalized uplift capacity increased linearly with the ratio of the embedment depth to the anchor diameter, which is called the embedment depth ratio.

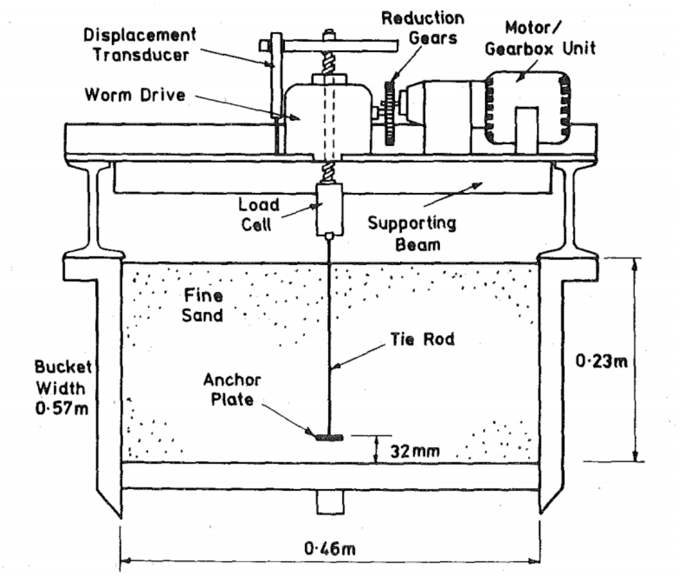

Fig. 2.2 Typical test layout of the model test in centrifuge by Dickin (1988)

Ovesen, (1981) reported the comprehensive analyses based on centrifuge tests. Reduced-scale experiments in 1g condition are subject to a scale effect related to the nonlinear behavior of the soil according to different confining pressures, as shown in Fig 2.3. Baker & Konder, (1966) and performing several centrifuge tests on an anchor of a 29.1 mm diameter under a centrifugal acceleration of 50 g. The centrifuge technique has been applied to overcome the scale effect on the evaluation of the uplift bearing capacity of anchor plates. Figure 2.4 presents the uplift resistance factor of the 3 different anchors having different diameters subjected to different centrifugal acceleration. Even though the diameter is a different diameter, the factor is similar in the same prototype scale. Ovesen (1981) confirmed that the scale effect could be eliminated by reasonably simulating the in-situ stress condition and the ratio of the anchor diameter to the average median size of the soil particles $D_{50}$.

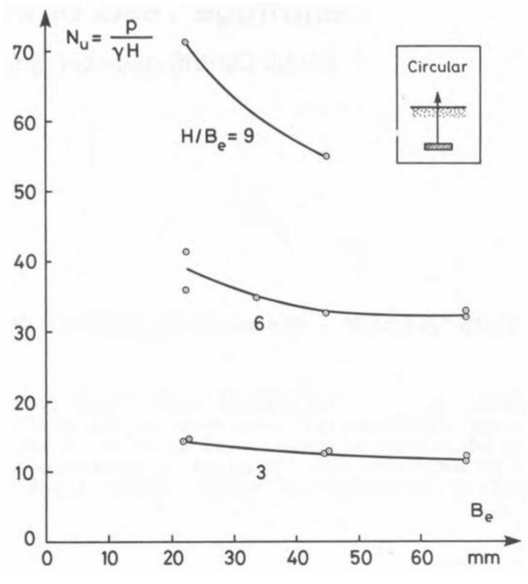

Fig. 2.3 Results of 1g model tests with anchors performed by Baker and Konder (1966).

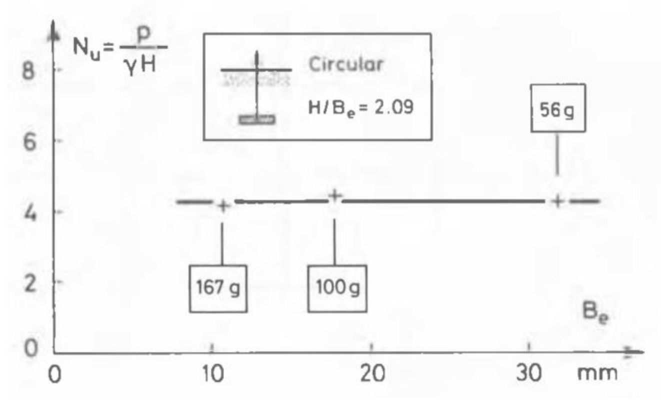

Fig. 2.4 Results of centrifugal tests with three different model anchors corresponding to a prototype, embedment depth=3.70m and width=1.77m by Ovesen (1981)

Sakai and Tanaka (1998, 2007) demonstrated the characteristics of progressive failure and scale effect by using 2D finite element analysis and laboratory tests to investigate the scale effect. The results of numerical simulation were validated with load-displacement curves of 1g test. Analyses showed that scale effect was remarkable with increase in embedment depth ratio, as shown in Fig. 2.5. The concentrated zone of shear strain develops upward, indicating progressive failure of the sand. The direction of the developing shear band is outward in small embedment depth ratio. The range of the shear band is large with increase of embedment depth ratio.

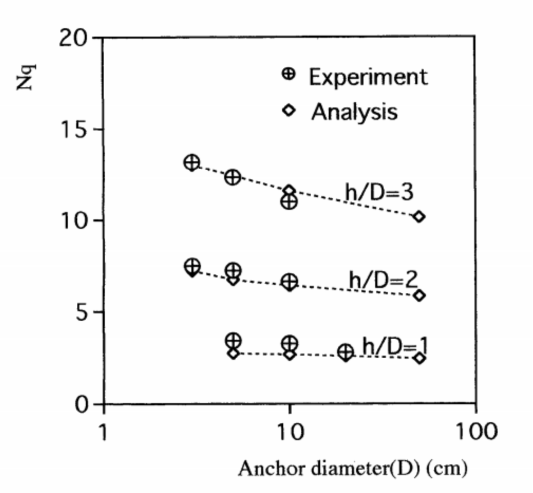

Fig. 2.5 Relationship between peak $N_q$ and $D$ on 1g model tests by Sakai and Tanaka (1998)

Dickin and Leung (1992) performed centrifuge model tests to study the influence of the foundation geometry on the uplift behavior. The test variables consist of soil density and diameter ratio of a shaft diameter to a diameter of foundation slab, $b_s/b_b$. Test results showed the foundation with large $b_s/b_b$ reached peak load at small displacement in Fig 2.6. This effect is more significant in loose sand. The peak displacement is large in loose sand due to the rate of mobilized shear resistance, as shown in Fig. 2.7. The Relative failure displacement can be defined with the ratio of peak displacement to the diameter of foundation slab.

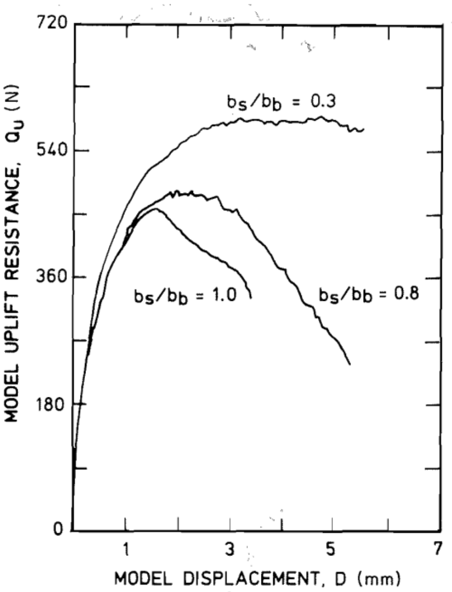

Fig. 2.6 Variation of net uplift resistance with displacement for models of different diameter ratio by Dickin and Leung (1992)

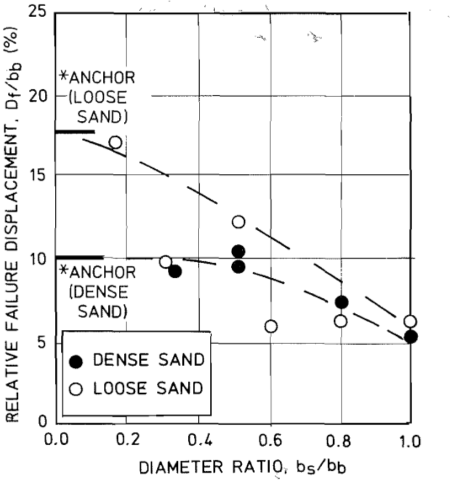

Fig. 2.7 Variation of relative failure displacement $D_f/b_b$ with diameter ratio $b_b/b_s$ in centrifuge tests by (Dickin & Leung, 1992)

### 2.2.3 Field tests

A few trials of field tests on the spread foundation and anchor were reported. Kananyan (1966) conducted a series of field tests on the anchor foundations with various diameters of 0.4–1.2 m and a constant embedment depth of 1 m and reported that the upward displaced area on the ground surface was extended to 1.75 times that of the anchor diameter relative to the center of the anchor. In addition, the failure surface was curvilinear near the anchor plate and circular near the ground surface. Trautmann and Kulhawy (Trautmann & Kulhawy, 1988) attempted proposing a general load–displacement curve for spread foundations with an embedment depth ratio of less than 3 by analyzing the field tests of Kulhawy et al. (Kulhawy et al., n.d.). The uplift bearing capacity, as a load control procedure used in the field tests, was determined by applying the tangent method, probably leading to uncertainty in the accuracy and precision of their analysis.

## 2.3 Failure mechanism

Particle image velocimetry (PIV) has been successfully used to investigate the formation of the failure surface on the basis of soil particle movement analysis. So far, no theoretical failure surface has been proposed through PIV.

### 2.3.1 Failure surface captured by Experimental study

Ilamparuthi et al. (2002) conducted an extensive 1g model test program to study the uplift behavior and failure mechanisms. The full and half-cut model foundations were adopted. Figure 2.2 show the schematic uplift testing arrangement. Test results showed uplift bearing capacity increase with deeper embedment depth. For a particular anchor diameter, however, the peak load rises more quickly as embedding depth increases. Failure modes consist of shallow and deep failure modes. Ground displacement heaves in shallow failure mode as the failure surface reach to the ground surface. Linear failure surface was analyzed by half-cut model test results as shown in the Fig. 2.8. Failure surface of deep failure mode located in subsurface and was bulb shaped.

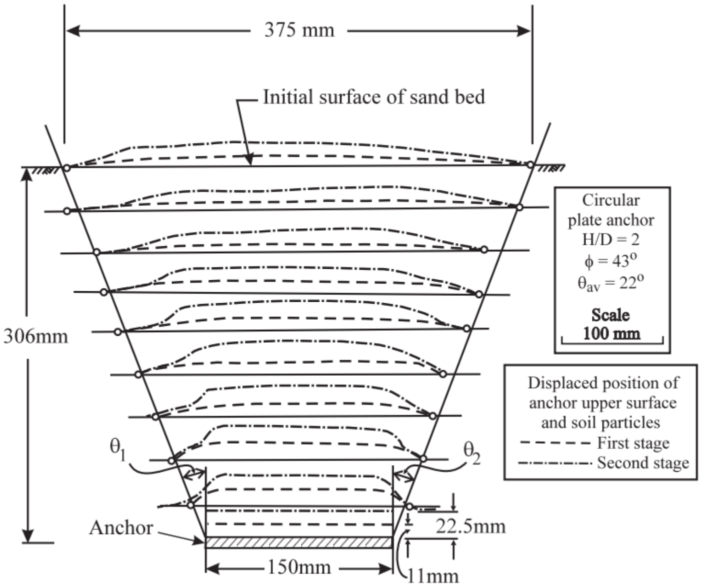

Fig. 2.8 Delineation of failure surface in half-cut model test on shallow anchor in dense sand by (Ilamparuthi et al., 2002).

Liu et al. (2012) carried out the a series of 1g half-cut model test to analyze failure mechanism using PIV method. Liu et al. (2012) stated that the failure surface of an uplift plate anchor is located within the shear band of cohesionless ground, which is bounded by an influence zone. The range of influence zone was determined as the boundary where volume change occurred. In Fig. 2.9., it was reported that volume expansion in dense ground and contracted under loose sand conditions. Under loose sand conditions, the failure surface would be developed close to the vertical part of the plate. If the embedment depth ratio is large, it would not reach the surface in Fig. 2.10. In dense cases, the failure surface is formed outward and was nearly linear at a maximum embedment depth ratio of 5. The angle of the failure surface in the dense sand is approximately 10° to the vertical line, showing 0.25 of the internal friction angle.

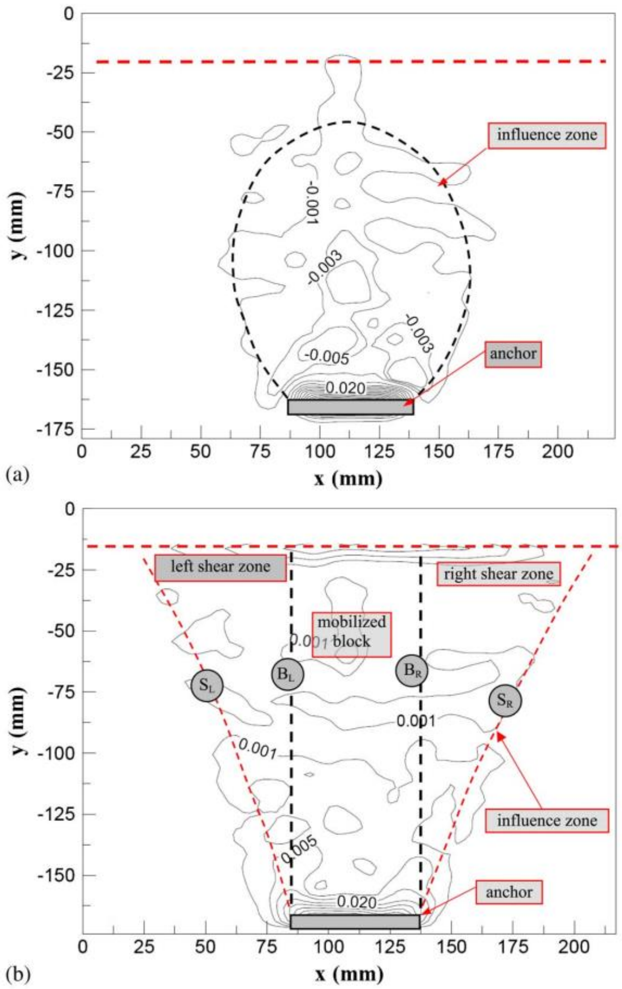

Fig. 2.9 Volume change of soil during anchor uplifting in fine sand by (Liu et al., 2012): (a) loose sand; (b) dense sand

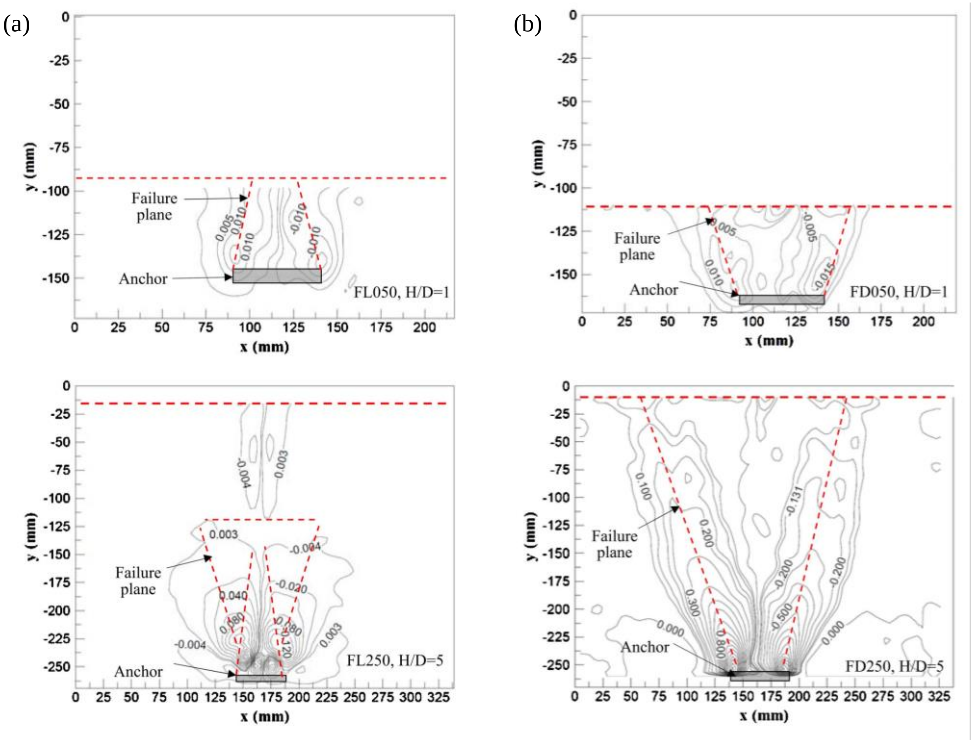

Fig. 2.10 influence of anchor embedment depth on the shear strain field: (a) loose; (b) dense

### 2.3.2 Failure surface suggested by theoretical

Balla (1961), Matsuo (1967) and Meyerhof and Adams (1968) conducted half-cut model tests to determine the shape of the failure surface through the observation of the resultant failure shape.

Meyerhof and Adams (1968) carried out 1g model tests of anchor plate. The test results were shown that the failure surface varied 0.25~0.5$\phi$. 0.3 $\phi$ was suggested as a linear failure surface in Fig. 2.11.

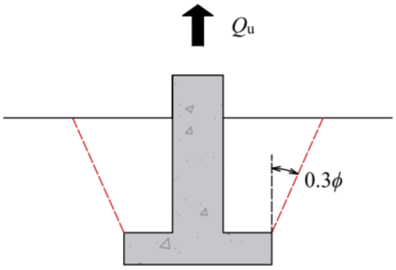

Fig. 2.11 Failure surface proposed by (Meyerhof & Adams, 1968)

Balla (1961) performed 1g model tests to determine the failure surface. Layered test sand was prepared to configure the failure surface. The results were reported that the curving line which is starting from the upper edge of the foundation slab with the vertical tangent line as shown in Fig. 2.12. Furthermore, Balla (1961) suggested a circular failure surface is intersecting the ground surface at an angle of 45°–$\phi$/2. The formulation of failure surface was suggested as follow:

$$\mathrm{r} = \frac{D - v}{\sin\left(\frac{\pi}{4} + \frac{\phi}{2}\right)} \tag{2.2}$$

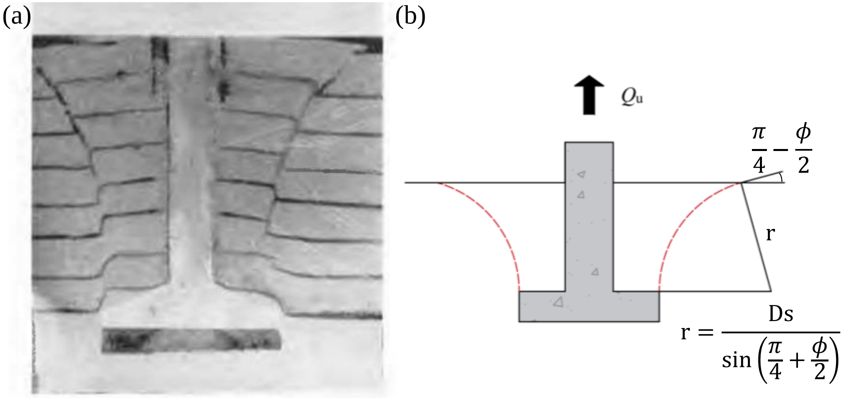

Fig. 2.12 Shape of the failure surface in half-cut model: (a) experimental result by (Balla, 1961); (b) suggested failure surface

Matsuo (1967) proposed a composite failure surface consisting of a logarithmic segment close to the foundation slab and a linear segment near the ground surface in Fig.2.13. The failure surface was divided into two sections. The logarithmic failure surface curve was formed near the vicinity of slab. It appears that the earth pressure state progressively changes from the semi-active condition near the foundation slab to the passive condition in that of the ground surface when the shear failure occurs due to the uplift loading of the footing. The logarithmic failure surface is defined from an imaginary point O of total resistance of the ground is minimal using the two-dimensional moment equilibrium. The failure surface is developing closely to the angle of the passive failure surface, $45\text{-}\phi/2$, which becomes a depth of logarithmic spiral failure surface from the top of the foundation slab. The failure surface near the surface ground forms a 45° angle with the horizontal plane. This is similar to the experimental results of Balla (1961), and is similar to the theoretical equation. The proposed failure surface theoretical equation was compared and verified through 1 g uplift model test.

The angle of the failure surface relative to the vertical line decreases with the increase of embedment depth. Notably, the earth pressure condition is semi-active near the foundation slab and passive near the ground surface.

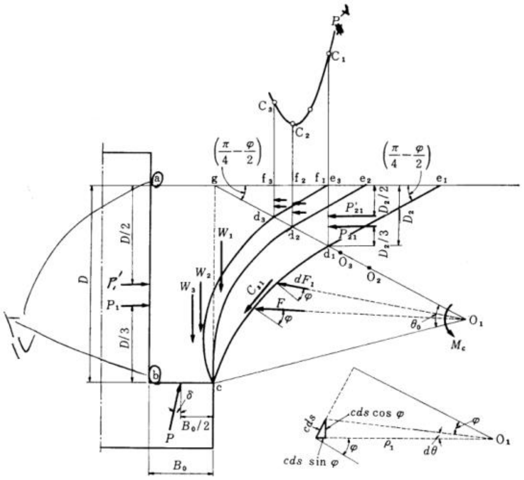

Fig. 2.13 Determination of failure surface of spread foundation by (Matsuo, 1967)

## 2.4 Solutions for the uplift bearing capacity

IEEE (2001) reported typical three types of failure modes: (1) Cone method; (2) Shear method; (3) Curved surface method

### 2.4.1 Cone method

The cone method is a totally empirical approach that, for square and circular foundations, respectively, assumes that the failure surface is a truncated pyramid or cone. From the lower edge of the foundation slab upward and at an angle toward the ground, the failure surface has the shape of a cone. The uplift resistance is assumed by the cone methods to be just the weight of the soil and foundation. This method used uplift resistance factor to calculate uplift bearing capacity. This factor should be changed according to the ground conditions and foundation geometry.

Vermeer & Sutjiadi (1985) suggested the simplified equation for uplift bearing capacity based on the finite element computation and scale-model tests. The failure surface related to the angle of dilatancy depending on relative density was assumed linear line.

$$\mathrm{N}_u = 1 + 2\left(\frac{D}{B}\right)\tan\phi\cos\phi_{cv} \tag{2.3}$$

Where, $\phi_{cv}$is the critical state friction angle

the diameter of a circular foundation of previous studies was converted to an equivalent width of a square foundation.

Murray & Geddes, (1988) carried out the laboratory tests on anchor plate to proposed the formulation of uplift resistance factor using the limit equilibrium analysis. A square anchor plate's failure surface configuration appears to be a straight failure surface that is inclined at an angle of phi to the vertical at the plate's edge. Furthermore, the uplift bearing capacity of circular anchors is approximately 1.26 times larger than the capacity of square anchors in very dense sand.

$$\mathrm{N}_u = 1 + \left(\frac{D}{B}\right)\tan\phi\left(2 + \frac{\pi}{3}\left(\frac{D}{B}\right)\tan\phi\right) \tag{2.4}$$

Ilamparuthi et al. (2002) proposed an uplift resistance factor for a circular anchor plate according to the embedment depth ratio through the 1g model test in Section 2.3.

$$\mathrm{N_{qf}} = e^{(33.5/28)/(H/D)}, \text{ for } 0 \le (\mathrm{H/D}) \le 1.0 \tag{2.5}$$

$$\mathrm{N_{qf}} = (H/D)\mathrm{N_{qf1}}, \text{ for } 1.0 < (\mathrm{H/D}) \le 2.4 \tag{2.6}$$

$$\mathrm{N_{qf}} = (H/2D)(e^{\tan\phi \ln(H/D)})\mathrm{N_{qf1}}, \text{ for } 2.4 < (\mathrm{H/D}) \le 4.2 \tag{2.7}$$

$$\mathrm{N_{qf}} = \left[(H/D) + (H/D)(e^{\tan\phi \ln(D/H)})\right]\mathrm{N_{qf1}}$$

$$\text{, for } 4.2 < (\mathrm{H/D}) \le 6.0 \tag{2.8}$$

$$\mathrm{N_{qf}} = \left[(H/D)(e^{\tan\phi \ln(H/D)})\right]\mathrm{N_{qf1}}, \text{ for } 6.0 < (\mathrm{H/D}) \le 10.0 \tag{2.9}$$

$$\mathrm{N_{qf}} = \left[\mathrm{N_{qf10}} + e^{\tan\phi \ln(H/D-10)}\right], \text{ for } 10.0 < (\mathrm{H/D}) \le 12.0 \tag{2.10}$$

### 2.4.2 Shear method

Shear methods assumed that the shear resistance develops along a cylinder or rectangle shaped failure surface. It is assumed that a failure surface is formed vertically from the edge of the foundation slab to the surface. Since horizontal earth pressure is an important factor in calculating the shear resistance along the failure surface, determination of the horizontal earth pressure coefficient is dominant.

Meyerhof & Adams (1968) suggested the shear method based on the inclined failure surface to the vertical line.

The equation for the uplift bearing capacity of spread foundations were developed using simplifying assumptions due to the complex failure surfaces. Meyerhof & Adams, (1968) assumed a vertical failure surface, as depicted in Figure 2.14, and ignored the uplifted zone that was outside of the vertical failure surface. In a condition of plastic equilibrium, the effect of the shear resistance along the actual observed failure surface and the additional weight of soil included within the failure surface were taken into consideration.

$$Q_u = 2cD(B+L) + \gamma D^2(2sB + L - B)K_u \tan\phi + W \qquad (2.11)$$

where $Q_u$=uplift bearing capacity, c= unit cohesion, $D$ = embedment depth, W = weight of lifted soil mass and weight footing, $B$=slab width, L=slab length and $D_s$=embedment depth from the bottom of the slab to the ground surface (Fig. 2.14).

$$K_u = 0.496\phi^{0.18} \qquad (2.12)$$

where $K_u$ = nominal uplift coefficient of earth pressure on vertical plane through footing edge.

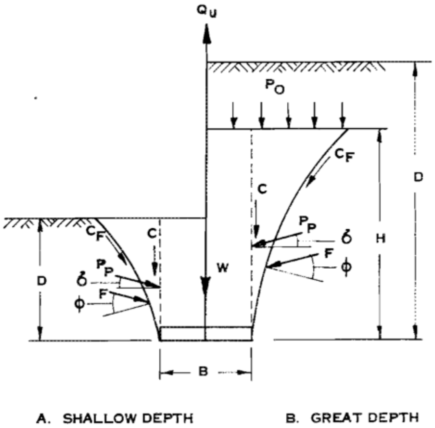

Fig. 2.14 failure mode of strip foundation under uplift load by (Meyerhof & Adams, 1968)

Matsuo (1967) reported Shichiri (1943) method which is consider the soil weight within the failure surface, foundation weight and shear resistance along the failure surface.

$$Q_u = cBD + 2\gamma \frac{\tan\phi}{1+\sin\phi} BD^2 \tag{2.13}$$

### 2.4.3 Curved surface method

The curved surface methods assume that the uplift bearing capacity is given by weight within the curved failure surface zone, plus the shearing resistance along the curved surface. The assumption of a curved surface presumes that a cone of failure always occurs, and most of these methods disregard the backfill variations and soil stress. Since the failure surface depends on the ground condition and the foundation geometry, the uplift bearing capacity is greatly affected by the shape of failure surface.

Theoretical calculations of the uplift bearing capacity of plate anchors and shallow foundations based on small-scale test results have been proposed. Several researchers have attempted to develop a theoretical method that considers shear resistance along and soil weight inside the failure surface.

Several researchers used the Kotter's (1903) equation to calculate shear resistance (Fig. 2.15). Kotter's (1903) equation has the following equation:

$$\frac{dp}{ds} + 2p \tan \phi \frac{d\alpha}{ds} = r \sin(\alpha + \phi) \qquad (2.14)$$

Where, dp = differential reaction pressure on the failure surface

ds = differential length of failure surface

$\phi$ = angle of soil internal friction

$d\alpha$ = differential angle

$\alpha$ = angle of failure plane formed by inclination of tangent at the point of interest with the horizontal.

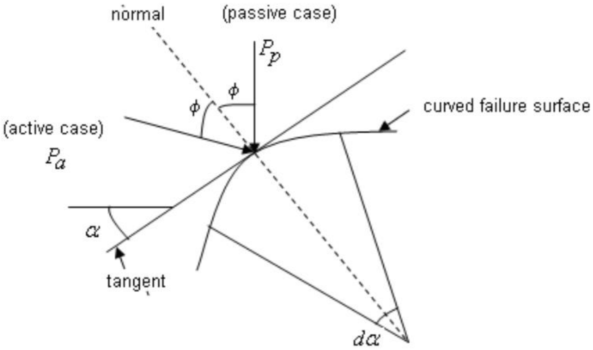

Fig. 2.15 Kotter's equation for a curved failure surface (adopted from (Deshmukh et al., 2010))

Balla (1961) proposed a calculation formula for calculating the uplift resistance of the enlarged base of the circular bottom plate considering the failure surface in section 2.3. Uplift bearing capacity is calculated by the sum of the shear resistance generated in the foundation weight, soil weight within failure surface, and failure surface. The proposed equation is as follows.

$$Q_u = G_1 + G_2 + T_\mathrm{v} \tag{2.15}$$

where $G_1$= Weight soil within failure surface, $G_2$=weight of foundation, $T_\mathrm{v}$=shear resistance along the failure surface.

Balla (1961) adopted Kotter's equation to compute the shear resistance along the failure surface considering a solely passive stress state despite the varied objectives of their studies. Note that the direction of shear force applied in Kotter's equation will be changeable if the different stress states are accounted for along the failure surface. Shear resistance was calculated approximately by assuming a plane stress state. After additional contractions and transformations, the equation is obtained as follows:

$$Q_u = (D - v)^3 \gamma \left[ F_1(\phi, \lambda) + \frac{c}{\gamma} \frac{1}{D - v} F_2(\phi, \lambda) + F_3(\phi, \lambda) \right] + G_2 \tag{2.16}$$

Where $F_1(\phi,\lambda)$, $F_2(\phi,\lambda)$, $F_3(\phi,\lambda)$, are factors depending of the angle of friction and embedment depth ratio.

In addition, the calculation process of F1, F2, and F3 of the proposed equation is quite complicated, so the chart was proposed considering the geometry of foundation and ground conditions instead of the calculation process. In the case cohesionless soils, the calculation of uplift bearing capacity is sum of $F_1$ and $F_2$ and was plotted in Fig. 2.16.

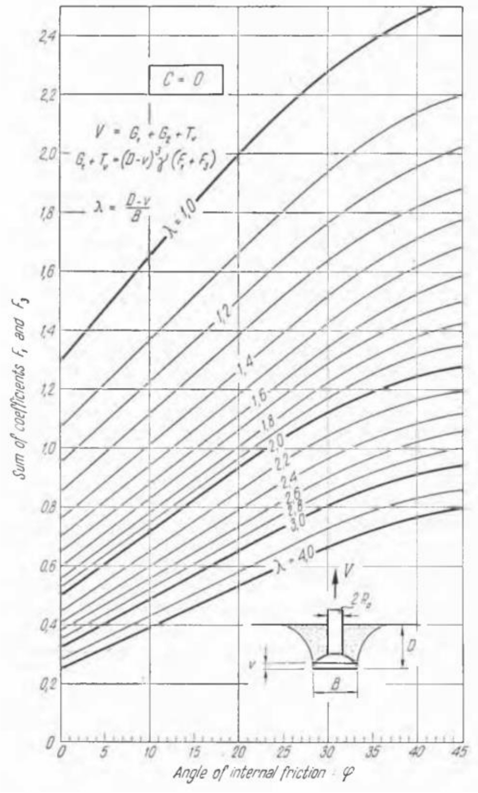

Fig. 2.16 Coefficients of uplift resistance by (Balla, 1961)

Matsuo (1967, 1968) suggested an analytical solution for calculating the uplift bearing capacity of the spread foundations considering the failure surface in section 2.3 (Fig. 2.17). Matsuo (1967) derived his own equation for shear resistance and concluded that the derivative equations are identical with Kotter’s equation.

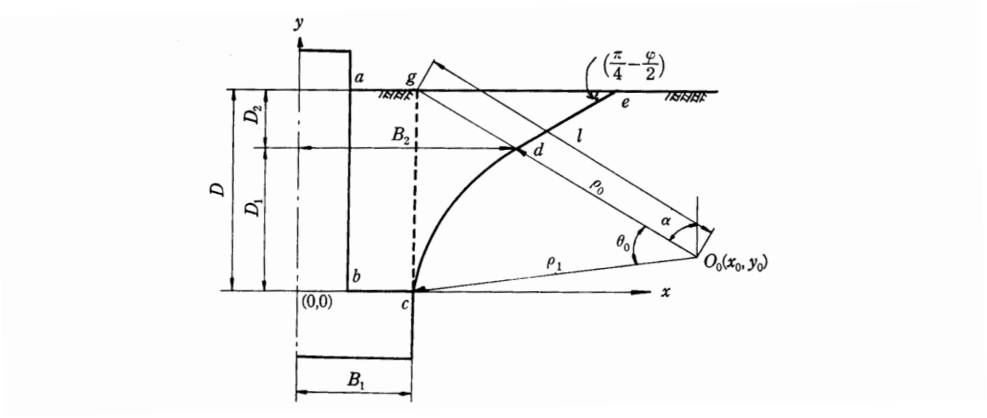

Fig. 2.17 Geometry of failure surface by (Matsuo, 1967)

$$\mathrm{Q}_u = G + \gamma(B_2^3 K_1 - V_3) + \mathrm{c}B_2^2 K_2 \tag{2.17}$$

$$K_1 = \pi\{(a-1)(a^2F_1 + aF_2 + abF_3 + bF_4 + F_5) + b\} \tag{2.18}$$

$$K_2 = \pi\{(a-1)(aF_6 + F_7) + b(b\tan\alpha + 2)\} \tag{2.19}$$

$$a = \frac{x_0}{B_2} \tag{2.20}$$

$$b = \frac{D_2}{B_2} \tag{2.21}$$

where, $G$=the weight of foundation, $B_2$ = the horizontal distance from the centerline of the shaft of the foundation, $F_1 \sim F_7$ are the coefficient, and $V_3$ = The volume of shaft of foundation below the ground surface.

Since the procedure of his solution is also complicated to calculate, the simple formulation was proposed. . (Matsuo, 1967) also proposed a simple formula

For 0.5≤λ≤1,

$$\mathrm{B}_2^3 K_1 = (0.056\phi + 4.000) B_1^3 \lambda^{(0.007\phi + 1.000)} \tag{2.22}$$

$$\mathrm{B}_2^2 K_2 = (0.027\phi + 7.653) B_1^2 \lambda^{(0.002\phi + 1.052)} \tag{2.23}$$

For 1≤λ≤3,

$$\mathrm{B}_2^3 K_1 = (0.056\phi + 4.000) B_1^3 \lambda^{(0.016\phi + 1.100)} \tag{2.24}$$

$$\mathrm{B}_2^2 K_2 = (0.027\phi + 7.653) B_1^2 \lambda^{(0.004\phi + 1.103)} \tag{2.25}$$

For 3≤λ≤10,

$$\mathrm{B}_2^3 K_1 = (0.597\phi + 10.400) B_1^3 \left(\frac{\lambda}{3}\right)^{(0.023\phi + 1.300)} \tag{2.26}$$

$$\mathrm{B}_2^2 K_2 = (0.013\phi + 6.110) B_1^2 \lambda^{(0.005\phi + 1.334)} \tag{2.27}$$

Deshmukh et al. (2010) adopted the linear failure surface of Meyerhof and Adams (1968) and put forward an analytical method to calculate the uplift bearing capacity of square anchors using Kotter's equation. The symmetric trapezoid shape of failure volume was suggested in Fig. 2.18

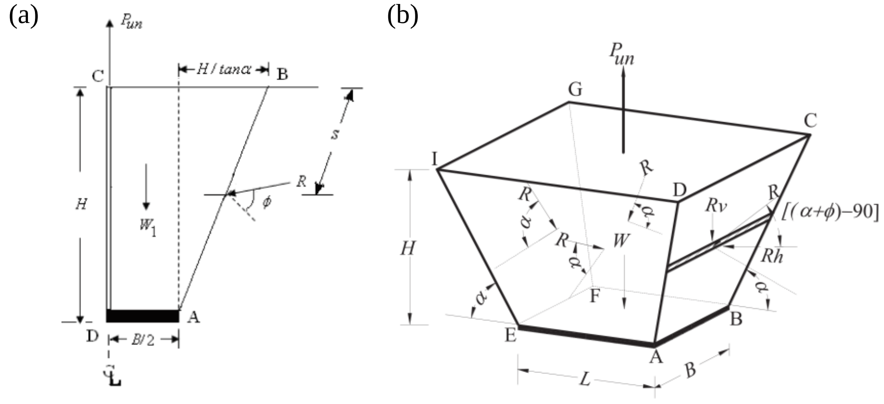

Fig. 2.18 Free body diagram of the rectangular anchor by (Deshmukh et al., 2010)

$$\mathrm{Q}_{net} = R_v + W$$

$$= \frac{\gamma\sin(\alpha+\phi)\sin[(\alpha+\phi)]-90]}{\cos^2\alpha}$$

$$\times\left\{\frac{B^3+L^3}{6}+\frac{2}{3}(b^3+n^3)-\frac{(bB^3+nL^3)}{2}+\frac{BLH}{2}2Hbn\right\} \tag{2.28}$$

$$\mathrm{b} = \left(\frac{B}{2}+\frac{H}{\tan\alpha}\right) and \left(\frac{L}{2}+\frac{H}{\tan\alpha}\right) \tag{2.29}$$

Where, $R_v$ = vertical component of the shear resistance along the failure surface and $W$= the net weight of trapezoid soil mass

All of (Balla, 1961; Deshmukh et al., 2010; Matsuo, 1967) adopted Kotter's equation to compute the shear resistance along the failure surface considering a solely passive stress state despite the varied objectives of their studies. Note that the direction of shear force applied in Kotter’s equation will be changeable if the different stress states are accounted for along the failure surface.

Chattopadhyay and Pise (1986) developed a slice method based on the limit equilibrium for the uplifted pile. The failure surface suggested and expressed by natural logarithmic functions. The uplift capacity is the summation of the shear strength along the failure surface and weights of the soil and pile in the slice method as shown in Fig 2.19. Lin et al. (2015) and Kang et al. (2019) adopted this method to estimate the shear resistance on the failure surface of a belled pier, which may be a similar problem to piles under uplift loading.

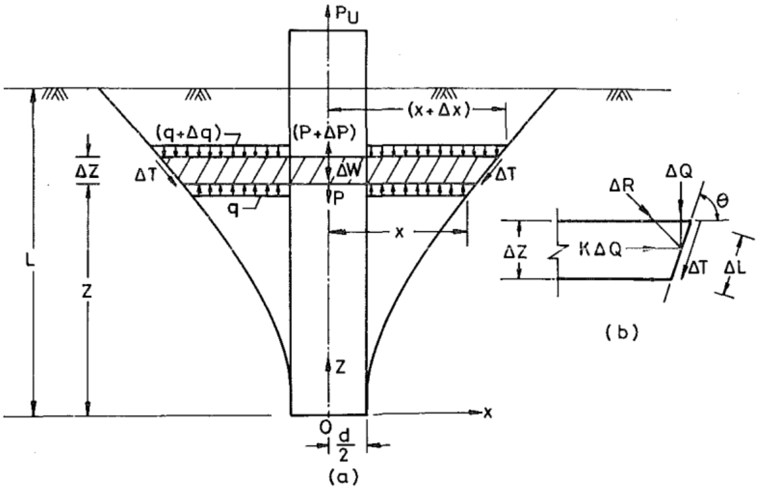

Fig. 2.19 Free body diagram of logarithmic failure surface by (Chattopadhyay & Pise, 1986)

# Chapter 3.Centrifuge test program for uplift behavior

## 3.1 Centrifuge modeling

The centrifugal model experiment was performed in two types: (1) Full model centrifuge test; (2) Half-cut model centrifuge test. Centrifuge experiments were carried out using the Korea Advanced Institute of Science and Technology's centrifuge facility (KAIST) in Fig 3.1. The centrifuge machine has a maximum capacity of 240 g-tons and a nominal radius of 5 meters. Kim et al. (2013) reported that this centrifuge equipment is capable of replicating geotechnical issues. A 50 g centrifugal acceleration was used to test every centrifuge test model.

Fig. 3.1 Centrifuge test machine

This study adopted the scaling law presented by Madabhushi (2017) was adopted in this study. Reduced-scale model for full-scaled field structure is an exact

1/$N$ scale model of the field structure and placed on the bucket which is hanging on the end of the centrifuge arm. The reduced-scale model is rotated and accordingly subjected to the $N$ g level of the radial acceleration field. In centrifuge modelling, 1/$N$ reduced-scale model of a prototype in the enhanced gravity field that is increased by the same geometric factor N relative to the 1g.

Table 3.1 Scaling factors applied in centrifuge experiment.

| Quantity | Scaling Factor (Prototype/Model) |
|---|---|
| Length | $1/N$ |
| Mass | $1/N^3$ |
| Stress | 1 |
| Force | $1/N^2$ |
| Time | $1/N$ |

## 3.2 Soil properties

For the experiments, dry silica sand with two distinct relative densities $D_r$, a poor particle size distribution, and a median particle size $D_{50}$ = 0.237 was utilized in Fig. 3.2. In order to attain uniform ground in medium-dense sand with $D_r$ = 40% and dense sand with $D_r$ = 80%, cohesionless test ground was prepared using the pluviation method. Medium-dense and dense sands had unit weights of 13.60 and 15.04 kN/m$^3$, respectively, with internal friction angles $\phi$ of 38° and 44°. Table 3.2. and Table 3.3 provides specifics on the soil's characteristics.

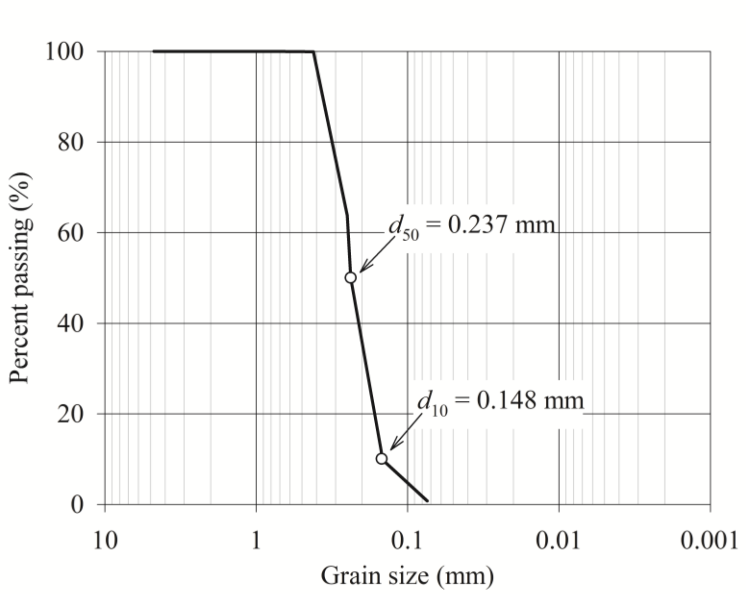

Fig. 3.2 Grain size distribution curve of silica sand.

Table 3.2 Physical properties of silica sand.

| Properties | Values |
|---|---|
| Specific gravity | 2.65 |
| Maximum dry density (t/m$^3$) | 1.64 |
| Minimum dry density (t/m$^3$) | 1.24 |
| Mean particle (mm) | 0.237 |
| Soil classification (USCS) | SP |

Table 3.3 Mechanical properties of silica sand.

| Void ratio | Relative density (%) | Consolidation stress | Peak friction angle (deg) | Critical friction angle (deg) |
|---|---|---|---|---|
| 0.86 | 48 | 100 | 39.7 | 36.6 |
| 0.88 | 44 | 200 | 38.0 | |
| 0.87 | 47 | 400 | 37.9 | |
| 0.81 | 59 | 600 | 36.8 | |
| 0.79 | 64 | 50 | 43.2 | |
| 0.76 | 69 | 100 | 43.9 | |
| 0.77 | 67 | 200 | 41.8 | |
| 0.77 | 66 | 400 | 40.1 | |
| 0.68 | 83 | 100 | 45.2 | |
| 0.71 | 78 | 200 | 43.1 | |
| 0.68 | 84 | 400 | 42.8 | |

## 3.3 Foundation model

In the centrifuge test model, the roughness between the concrete and the ground was simulated by grinding the aluminum foundation surface in accordance with the findings of Han et al. (2018). As shown in Fig. 3.3, the surface profile of the model foundation, which was used to assess the normalized roughness $R_n$, was measured using a device with a resolution of 0.01 μm along the foundation surface at distance of 10 mm. By dividing the total distance normal to the surface ($H_i$) by the total number of window sizes ($L_s$), where $L_s$ was set to $D_{50}$, the normalized roughness was computed. According to empirical suggestion of Han et al. (2018), the value of $R_n$ was roughly 0.0157, which translates to an interface friction angle that is 0.655 times greater than the soil friction angle. This interface friction angle was fairly close to the reported value of $2/3\phi$ that Meyerhof and Adams (1968) had calculated in their theory. In addition, a series of direct shear tests at various confining pressures were carried out to confirm the evaluation of the interface roughness based on the surface profile measurement, as shown in Fig. 3.4.

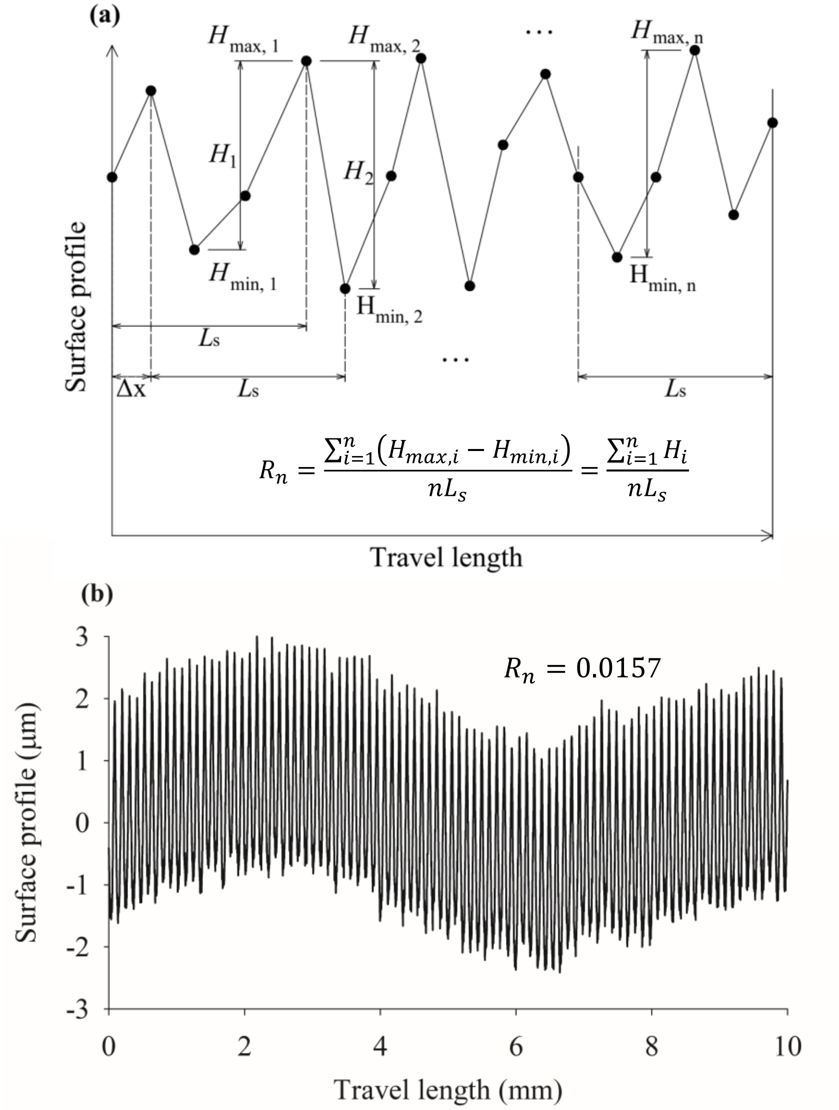

Fig. 3.3 Evaluation of normalized roughness $R_n$ of soil–foundation interface based on surface profile measurement: (a) definition (adopted from Han et al. 2018), (b) measured profile and result

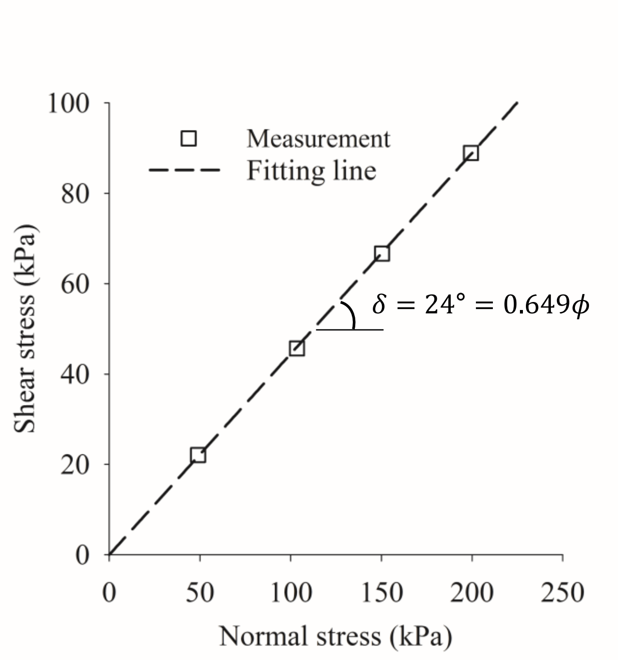

Fig. 3.4 Evaluation of soil−foundation interface friction angle ($\delta$) from direct shear tests

## 3.4 Test program and layout

The prototype structure of this study was a transmission tower supported by four square spread foundations. One of the major loads acting on the transmission tower is the overturning, which results in the compression and tension at the individual foundation. To simplify the problem in view of geotechnical engineering, the uplift behavior of a single spread foundation is investigated.

A displacement control procedure was adopted to uplift the spread foundation vertically with a velocity of 0.1 mm/s (Rattley et al., 2008).

The loading direction was controlled by introducing a hinge between the foundation shaft and the load cell. An actuator with a capacity of 100 kN was used to perform uplift tests. The uplift load transferring from the actuator to the spread foundation was measured by a load cell. The hinge was a pin connector; its hole was larger than that of the pin to eliminate the stress induced by the soil settlement during the initial spinning. The hole diameter was 12 mm, which was approximately three times larger than the expected ground settlement following the method of Janbu (1963).

During uplift loading, the load and displacement were measured to evaluate the uplift behavior of the spread foundation. The ground displacement was recorded to analyze the influence zone and verify the analysis with test results.

DSLR camera was used for taking images of soil movement through transparent window to analyze uplift failure mechanism. The specifications of the instrument used in centrifuge tests are summarized in Table 3.4.

Table 3.4 Specification of instrumentation used in this study

| Item | Load cell | Laser sensor | LVDT | 2D Profiler | Camera |
|---|---|---|---|---|---|
| Model name | TML<br>TCLK-20KNA | Keyence<br>IL-100 | Schaewitz MHR<br>500 MC | Keyence<br>LJ-X8400 | Cannon<br>70D |
| Range | ±20kN | 75~130 mm | ± 12.7mm | ± 34 mm | 20.0 MP |
| Linearity | 0.1% RO | ±0.15% F.S. | 0.15% RO | ±0.025% F.S. | |

### 3.4.1 Test layout of centrifuge test for the uplift behavior

Each centrifuge model consisted of three spread foundations, which were evenly distributed in an aluminum container with the dimensions of 1.40 × 0.65 × 0.50 m (width × length × height) for full model centrifuge test, as shown in Fig. 3.5. The distance between individual spread foundations was specified at least 2.46 $B_f$ to reasonably investigate the uplift behavior of each foundation. Three foundations of each centrifuge model were tested in sequence at the centrifugal acceleration of 50 g (Fig. 3.5).

A series of centrifuge test models on the spread foundation in dry silica sand with different relative densities was constructed in consideration of varying slab width $B_f$ (3.0, 3.5, 4.5, and 6.5 m) and embedment depth ratio $D_s/B_f$ (0.67–1.39), where $D_s$ is the embedment depth counting from the top of the slab to the ground surface (Fig. 1.2), as shown in Table 3.5.

The uplift displacement of the spread foundation was obtained by averaging the measurement of two linear variable differential transformers (LVDTs) at the top of the foundation, as shown in Fig. 3.5b. The uplift displacement of the ground surface in all centrifuge tests was measured by a 2D laser profiler to evaluate the influence zone with minimal interference to the soil–foundation system. In addition, a number of laser sensors, which were placed at intervals of approximately 28–40 mm (0.3–0.4 $B_f$), were used to verify the application of the 2D laser profiler.

As mentioned in Section 1.1 Background, the uplift bearing capacity under inclined loading conditions can be evaluated through vertical loading. The loading conditions in the test program were determined as vertical loading conditions through experimental study for loading conditions. The experimental results and analysis of vertical and inclined loading conditions are summarized in Appendix A.

To investigate the effect of various conditions on uplift bearing capacity and behavior, moreover, additional experiments were performed. In Appendices B, C, and D, the uplift bearing capacity and behavior were analyzed by changing the experimental conditions of excavation angle, ground slope, and different diameter of foundation shaft.

Table 3.5 Test cases for full model (in prototype scale)

| Case | $D_r$ (%) | $B_f$ (m) | $D_f$ (m) | $B_s$ (m) | $t$ (m) | $D_s$ (m) | $D_f/B_f$ | $D_s/B_f$ | $B_s/B_f$ |
|---|---|---|---|---|---|---|---|---|---|
| 1 | 40 (Loose) | 3.0 | 3.0 | 1.2 | 0.75 | 2.25 | 1.0 | 0.75 | 0.40 |
| 2 | | 3.0 | 3.9 | 1.2 | 0.75 | 3.15 | 1.3 | 1.05 | 0.40 |
| 3 | | 3.0 | 4.8 | 1.2 | 0.75 | 4.05 | 1.6 | 1.35 | 0.40 |
| 4 | | 3.5 | 3.5 | 1.2 | 0.75 | 2.75 | 1.0 | 0.79 | 0.34 |
| 5 | | 3.5 | 4.55 | 1.2 | 0.75 | 3.80 | 1.3 | 1.09 | 0.34 |
| 6 | | 3.5 | 5.60 | 1.2 | 0.75 | 4.85 | 1.6 | 1.39 | 0.34 |
| 7 | | 4.5 | 4.50 | 2.0 | 0.75 | 3.00 | 1.0 | 0.67 | 0.44 |
| 8 | | 4.5 | 5.85 | 2.0 | 1.50 | 4.35 | 1.3 | 0.97 | 0.44 |
| 9 | | 4.5 | 7.20 | 2.0 | 1.50 | 5.70 | 1.6 | 1.27 | 0.44 |
| 10 | | 6.5 | 6.50 | 2.0 | 1.50 | 5.00 | 1.0 | 0.77 | 0.31 |
| 11 | | 6.5 | 8.45 | 2.0 | 1.50 | 6.95 | 1.3 | 1.07 | 0.31 |
| 12 | 80 (Dense) | 3.5 | 5.60 | 1.2 | 0.75 | 4.85 | 1.6 | 1.39 | 0.34 |
| 13 | | 4.5 | 4.50 | 2.0 | 1.50 | 3.00 | 1.0 | 0.67 | 0.44 |
| 14 | | 4.5 | 5.85 | 2.0 | 1.50 | 4.35 | 1.3 | 0.97 | 0.44 |
| 15 | | 6.5 | 6.50 | 2.0 | 1.50 | 5.00 | 1.0 | 0.77 | 0.31 |
| 16 | | 6.5 | 8.45 | 2.0 | 1.50 | 6.95 | 1.3 | 1.07 | 0.31 |

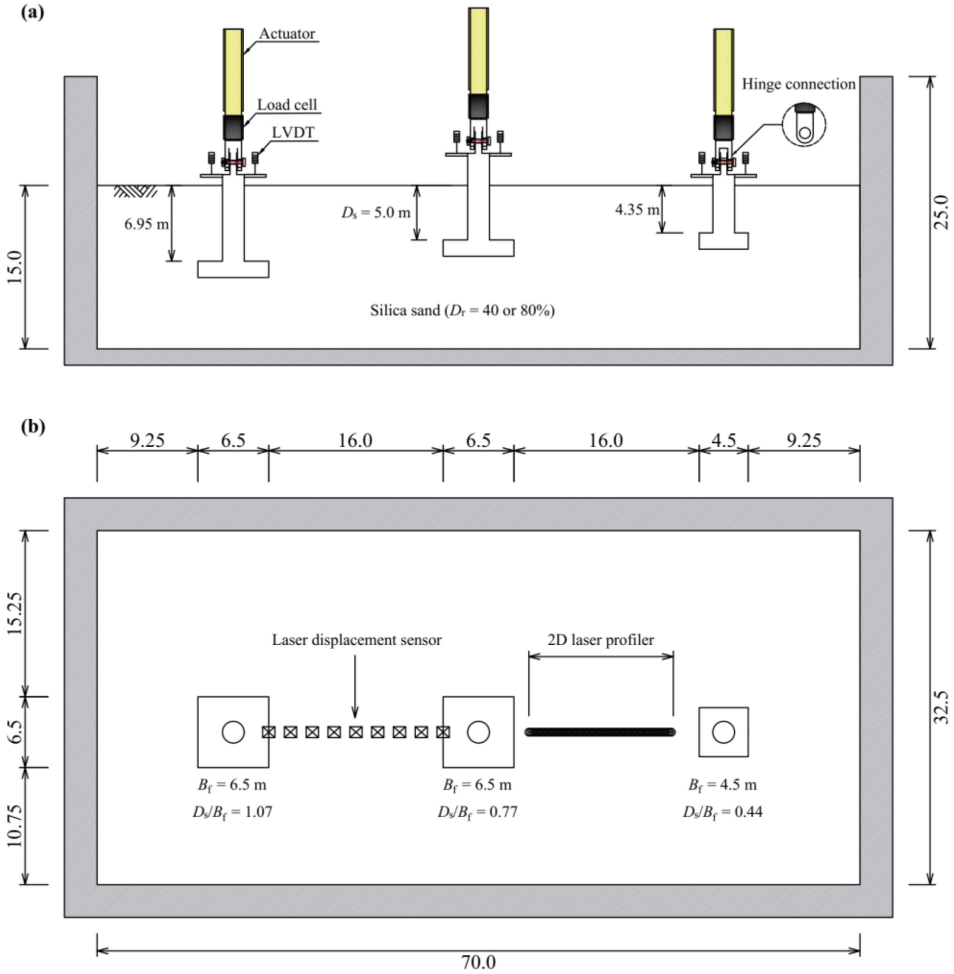

Fig. 3.5 Typical layout of centrifuge test for the uplift behavior: (a) front view, (b) plan view (dimensions in prototype scale and units in m)

### 3.4.2 Test layout of centrifuge test for the uplift failure mechanisms

Four spread foundations were located in soil box with the dimensions of 1.08 × 0.60 × 0.30 m (width × length × height) in each centrifuge model. The distance between individual spread foundations was specified at least 2.92 $B_f$ to reasonably capture the uplift failure mechanism of each foundation in Fig. 3.6. Four foundations of each centrifuge model were tested in sequence at the centrifugal acceleration of 50 g (Fig. 3.6). The foundation is installed on the transparent window with no gap and moves along the guide rail. The digital image of soil movement was taken by DSLR cameras for PIV analysis.

A series of centrifuge test models on the spread foundation in dry silica sand with different relative densities was prepared in consideration of varying slab width $B_f$ (3.5, 4.5, and 6.5 m) and embedment depth ratio $D_s/B_f$ (0.67–1.07), as shown in Table 3.6.

The uplift displacement of the spread foundation was measured as same as method explained above using LVDTs at the top of the foundation, as shown in Fig. 3.6 b and c. The uplift displacement of the ground surface was obtained by a series of LVDTs in line to verify the results of PIV analysis.

**(a)**

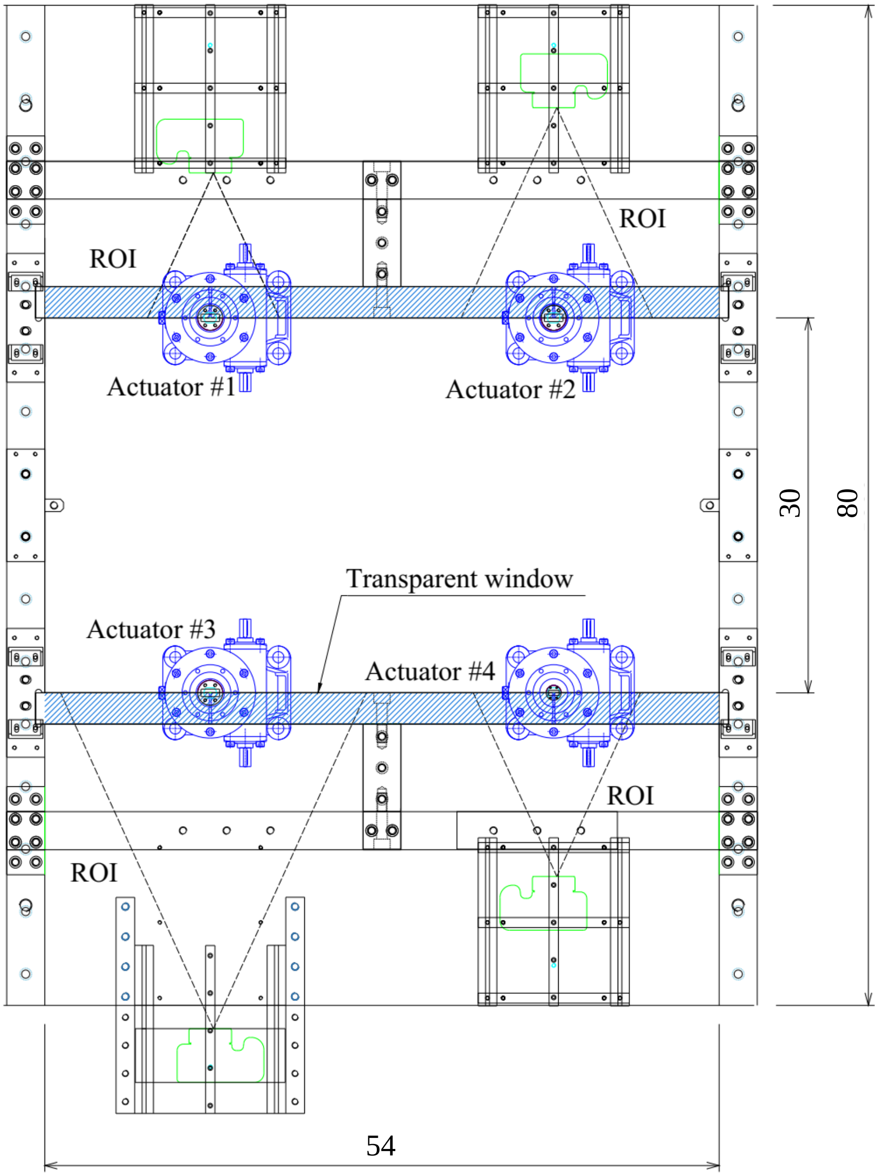

Fig. 3.6 Test layout of centrifuge test for the uplift failure mechanisms: (a) plan view; (b) front view; (c) side view (dimensions in prototype scale and units in m)

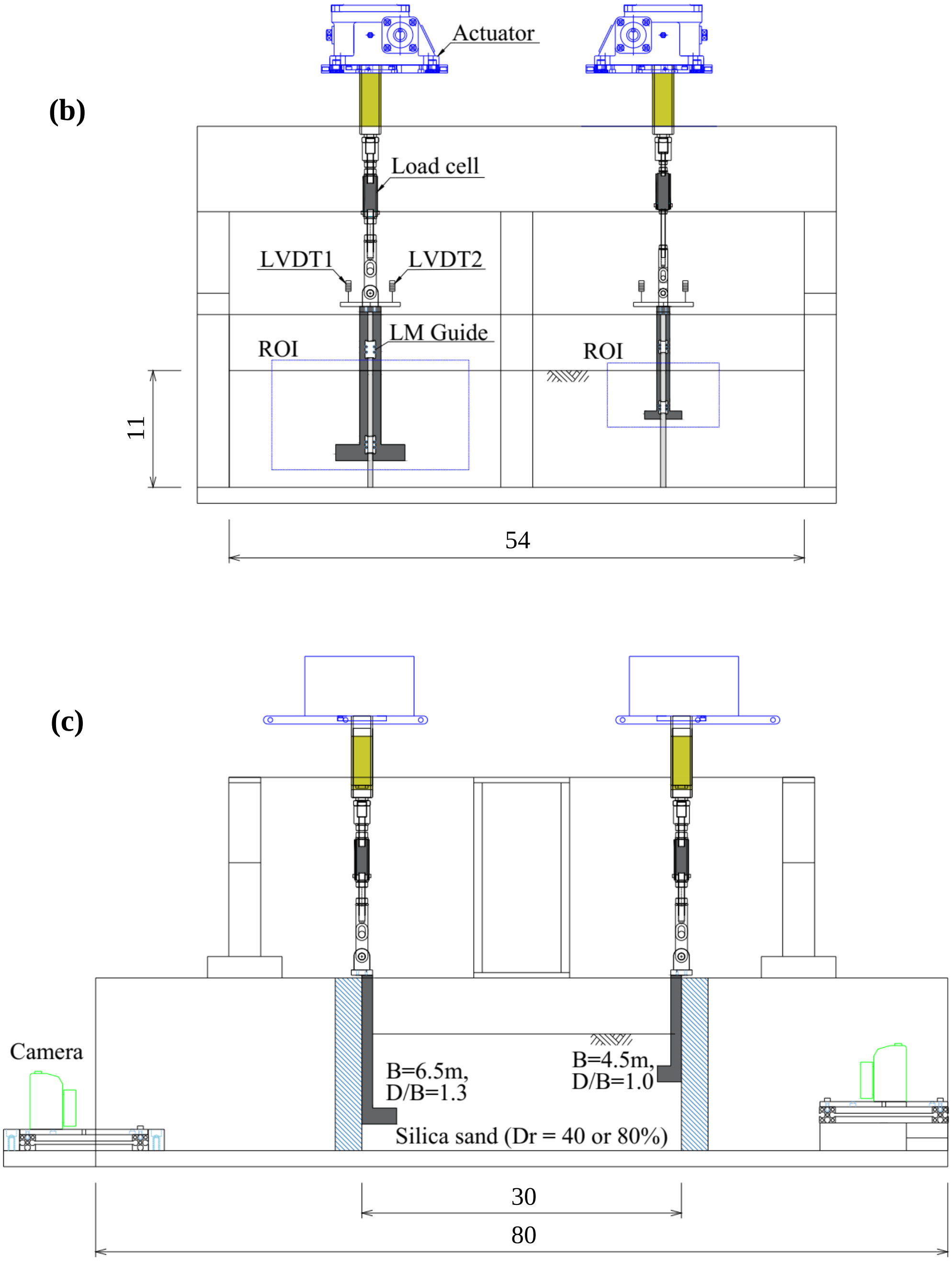

Fig. 3.6 (continued) Test layout of centrifuge test for the uplift failure mechanisms: (a) plan view; (b) front view; (c) side view (dimensions in prototype scale and units in m)

Table 3.6 Test cases for half-cut model (in prototype scale)

| Case | $D_r$ (%) | $B_f$ (m) | $D_f$ (m) | $B_s$ (m) | $t$ (m) | $D_s$ (m) | $D_f/B_f$ | $D_s/B_f$ | $B_s/B_f$ |
|---|---|---|---|---|---|---|---|---|---|
| 17 | 40<br>(Loose) | 3.5 | 4.55 | 1.2 | 0.75 | 3.80 | 1.3 | 1.09 | 0.34 |
| 18 | | 4.5 | 4.50 | 2.0 | 0.75 | 3.00 | 1.0 | 0.67 | 0.44 |
| 19 | | 6.5 | 8.45 | 2.0 | 1.50 | 6.95 | 1.3 | 1.07 | 0.31 |
| 20 | 80<br>(Dense) | 3.5 | 4.55 | 1.2 | 0.75 | 3.80 | 1.3 | 1.09 | 0.34 |
| 21 | | 4.5 | 4.50 | 2.0 | 1.50 | 3.00 | 1.0 | 0.67 | 0.44 |
| 22 | | 4.5 | 5.85 | 2.0 | 1.50 | 4.35 | 1.3 | 0.97 | 0.44 |
| 23 | | 6.5 | 8.45 | 2.0 | 1.50 | 6.95 | 1.3 | 1.07 | 0.31 |

### 3.4.3 Genetic Programming

a new empirical formula was developed by adopting a machine learning technique with the use of genetic programming for symbolic regression. Machine learning technique to derive a general solution which can represent the relationship between the input and output values. The genetic analysis was mainly performed using the gplearn package available in the Python library. In genetic programming, it is expressed in the form of a tree structure with various sizes and shapes composed of functions and terminals.

To depict a relationship between known independent variables and their dependent variable targets in order to predict new data, genetic programming a population of naive random formulas. Then, by choosing the population's fittest sets to undergo genetic operations, each succeeding generation of programs is developed from the one that came before it.

In genetic programming, it is expressed in the form of a tree structure with various sizes and shapes composed of functions and terminals. Function is various mathematical operators used to combine solutions, boolean operators, conditional operators, iteration operator, recursive functions, and user-defined functions. A terminal consists of a special variable term, a number, or a Boolean constant required to represent a solution. Figure 3.7 is a solution expressed in a tree structure. Terminal and function are basic components used in function expression, and two characteristics must be satisfied: (1) a function is a 'closure' that the given arguments must be well-defined for all combinations; (2) It is 'sufficiency' that the solution of the problem is expressed with a high reliability.

Operators used in genetic programming include selection, crossover and mutation: (1) selection: modeling the phenomenon of natural selection; (2) crossover: introduction of the concept in which new individuals are created by reproduction in the natural world; (3) mutation: Performs the process of restoring genetic traits lost as an individual goes through the process of evolution.

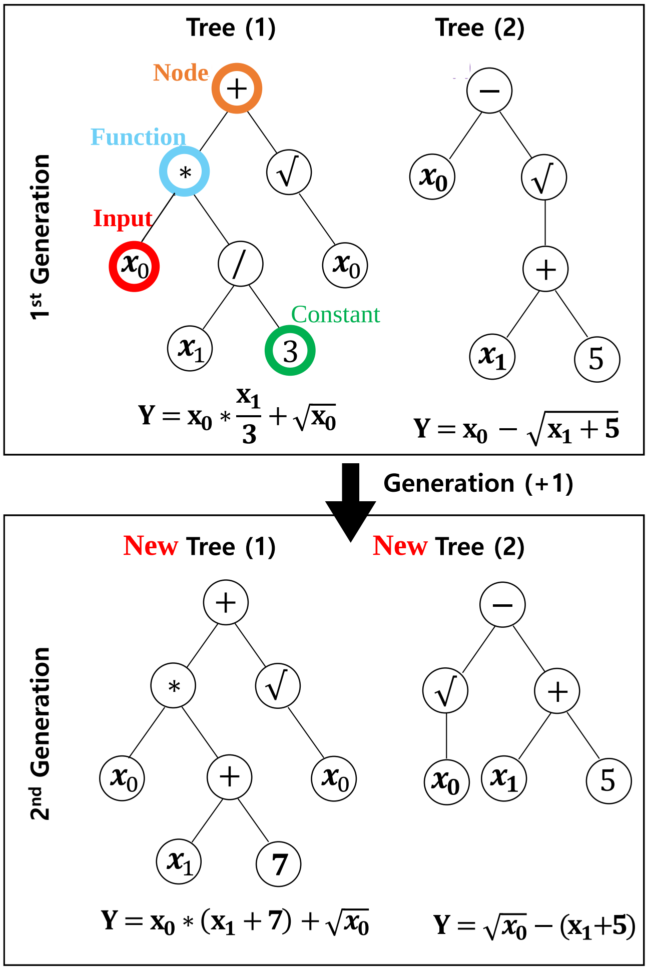

Fig. 3.7 Tree structure of genetic programming

### 3.4.4 Particle Image Velocimetry (PIV)

In this study, half-cut model centrifuge tests were conducted to capture soil movement during uplift of the foundation. A series of images are photographed through a transparent wall to interpret the soil movement using the DSLR camera. Particle image velocimetry (PIV) technique was developed to measure the deformation of a target object in the field of solid mechanics or to measure the speed of a moving object in the field of fluid mechanics. GeoPIV was developed based on the MATLAB module that implements PIV analysis in a way that is appropriate for geotechnical testing.

A sequence of photos is used to trace the texture of the soil in an image as part of the GeoPIV analysis process. PIV test patches are used to create a mesh out of the original image. First procedure is assigning the coordinates of one of these test patches are ($u_1$,$v_1$) in Fig. 3.8 The next step is used to locate this patch's relocated location in a later image. A larger patch taken from the same area of image 2 (time = $t_2$) is compared to the patch taken from image 1 (time = $t_1$) to determine their correlation. The patch's displacement position is shown by where the strongest correlation is found ($u_2$,$v_2$). By fitting a bicubic interpolation around the greatest integer peak, the correlation peak's location is determined with sub-pixel accuracy. To create complete trajectories for each test patch, this technique is repeated for the whole mesh of patches in the image and then repeated for each image in the series.

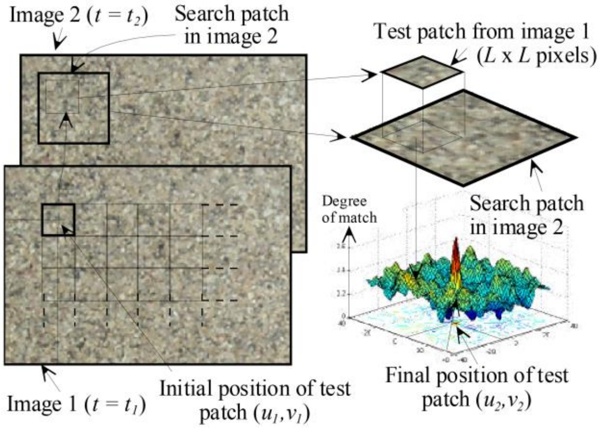

Fig. 3.8 Principles of PIV analysis (adopted from White and Take, 2002)

# Chapter 4.Uplift behavior of spread foundation

## 4.1 Introduction

As mentioned in Chapters 1 and 2, uplift behavior is main design consideration for foundations supporting transmission towers. Reduced-scale model tests under 1g conditions have been mainly performed. It has been reported that when applied to a prototype model using the results of 1g experiment, the uplift bearing capacity may be overestimated due to the scale effect.

In this chapter, the results of full foundation model test in centrifuge and the analyses of uplift behavior of shallow spread foundations were presented. The scale effect was investigated by adopting the uplift resistance factor. The influence factors to the uplift bearing capacity and the corresponding displacement at peak load were identified. Using the genetic analysis for symbolic regression, the empirical equations of uplift resistance factor and peak displacement were proposed. Also, the influence zone was suggested based on the vertical displacement of ground surface. Influence zone would be a reference to estimate the failure surface.

## 4.2 Uplift load displacement curves

Figure 4.1 illustrates the uplift load–displacement curves obtained from the centrifuge model tests. The uplift load–displacement curve consisted of three components corresponding to the uplift displacement magnitude: (1) linear elastic, (2) hardening, and (3) softening segments similar to those reported by Murray & Geddes (1988) and Dickin (1988). Within the elastic segment, the uplift load increased linearly with the uplift displacement at a relatively high rate. Subsequently, the increasing rate of the uplift load was reduced at the hardening segment until the peak load defined as $Q_u$. Finally, the uplift load decreased with further increase in the uplift displacement because of the reduction in the soil weight in the failure surface and the resistance along the failure surface. Huang et al. (2015) indicated that the failure surface narrowed down after the peak load was achieved. In reference to the findings of PIV analysis by Cheuk et al. (2008), the soil surrounding the foundation flowed downward in the post-peak stage and consequently reduced the soil weight and resistance. In addition, the soil behavior might exhibit the critical state after experiencing the peak state Cheuk et al., (2008). The foundations in dense sand showed a stiffer load–displacement curve compared with those in Loose sand.

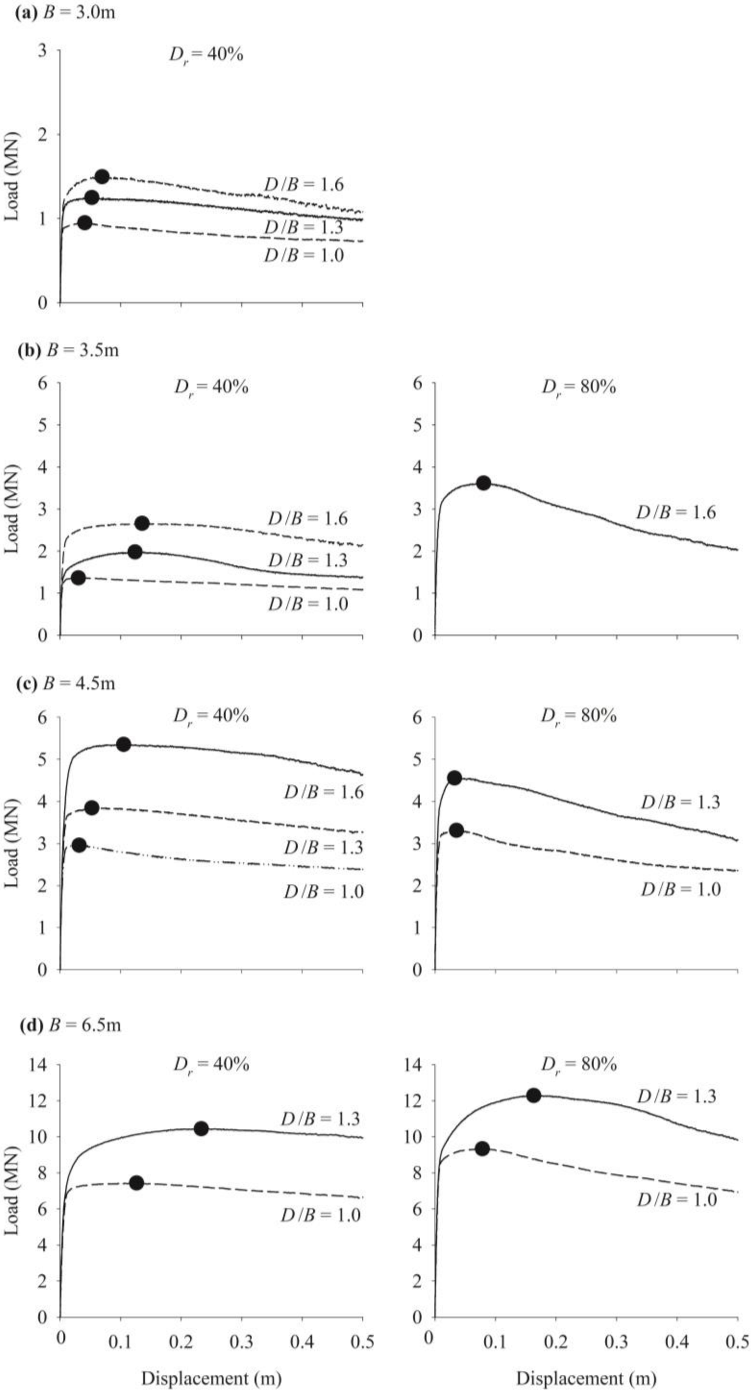

Fig. 4.1 Load–displacement curves obtained from centrifuge tests with different slab width $B_f$

## 4.3 Uplift bearing capacity

Several methods, such as maximum curvature and tangent intersection, have been developed to determine the bearing capacity of foundations. In this study, a numerical peak appeared and after that the curve showed the softening behavior (Fig. 4.1). Thus, the peak point was determined as the maximum uplift load and the corresponding uplift displacement. This method has been adopted by several researchers in the analysis of foundations under uplift loading (Dickin, 1988; Dickin & Leung, 1992; Ilamparuthi et al., 2002; Kulhawy et al., 1987). Nevertheless, a comprehensive study on the movement of soil particles and failure mechanism is necessary to define precisely the uplift bearing capacity and the corresponding uplift displacement.

The net uplift bearing capacity $Q_{\mathrm{net}}$, which was obtained by subtracting the foundation weight from the gross uplift bearing capacity $Q_{\mathrm{u}}$, was considered in further analysis. The foundation weight can be obtained from either measurement or calculation by determining the foundation dimensions and the unit weight. Table 4.1 summarizes the net uplift bearing capacity $Q_{\mathrm{net}}$ and the corresponding uplift displacement $w_{\mathrm{p}}$ of this study. The spread foundation embedded at a deeper depth showed a higher value according to the increase in the mobilized soil strength as well as the soil weight within the failure surface (Dickin, 1988; Ovesen, 1981). An increase in the slab width, i.e., the bearing area, induced an increase in $Q_{\mathrm{net}}$. For example, $Q_{\mathrm{net}}$ of the spread foundation with a slab width of 4.5 m in Loose sand was approximately 6%–16% larger than that with a slab width of 3.5 m. Considering the same slab width and embedment depth, the value of $Q_{\mathrm{net}}$ of the spread foundation in dense sand was approximately 20%–30% larger than that in the Loose sand because of the difference in the soil strength and stiffness. The behavior of $w_{\mathrm{p}}$ showed the same manner as $Q_{\mathrm{net}}$, considering the variation in the slab width and embedment depth ratio. Similar experimental observations at smaller slab widths could be found in the reports of Ovesen (1981), Dickin (1988), and Tagaya et al. (1988).

Figure 4.2 depicts the comparison of $Q_{\mathrm{net}}$ obtained from the present centrifuge test and calculation following the previously suggested formula. The wedge method recommended by Das & Jones (1982) and the shear method proposed by Matsuo, 1967 evaluated $Q_{\mathrm{net}}$ with and without accounting for the resistance along the failure surface, respectively. The shear method produced a better estimation of $Q_{\mathrm{net}}$ with an average difference of approximately 13%. However, both suggested formulas overestimated the net bearing capacity, especially at large slab widths, because these methods were developed mostly on the basis of 1g model test results. The stress state and strength of the ground might not be simulated appropriately in the 1g model tests and thereby leading to overestimation of $Q_{\mathrm{net}}$. This issue has been defined as the scale effect pointed out by Ovesen (1981), Dickin (1988), and Sakai & Tanaka (2007).

Table 4.1 Uplift bearing capacity and corresponding uplift displacement (in prototype scale)

| Case | $D_r$ (%) | $B_f$ (m) | $D_s$ (m) | $Q_u$ (MN) | $Q_{net}$ (MN) | $w_p$ (mm) |
|---|---|---|---|---|---|---|
| 1 | 40<br>(Loose) | 3.0 | 2.25 | 0.95 | 0.51 | 41 |
| 2 | | 3.0 | 3.15 | 1.25 | 0.79 | 52 |
| 3 | | 3.0 | 4.05 | 1.50 | 1.01 | 69 |
| 4 | | 3.5 | 2.75 | 1.36 | 0.85 | 30 |
| 5 | | 3.5 | 3.80 | 1.98 | 1.51 | 123 |
| 6 | | 3.5 | 4.85 | 2.66 | 2.05 | 135 |
| 7 | | 4.5 | 3.00 | 2.96 | 1.61 | 31 |
| 8 | | 4.5 | 4.35 | 3.84 | 2.39 | 52 |
| 9 | | 4.5 | 5.70 | 5.35 | 3.73 | 104 |
| 10 | | 6.5 | 5.00 | 7.43 | 5.06 | 126 |
| 11 | | 6.5 | 6.95 | 10.44 | 7.91 | 233 |
| 12 | 80<br>(Dense) | 3.5 | 4.85 | 3.62 | 2.98 | 80 |
| 13 | | 4.5 | 3.00 | 3.31 | 1.94 | 35 |
| 14 | | 4.5 | 4.35 | 4.55 | 3.10 | 32 |
| 15 | | 6.5 | 5.00 | 9.33 | 6.82 | 78 |
| 16 | | 6.5 | 6.95 | 12.28 | 9.75 | 163 |

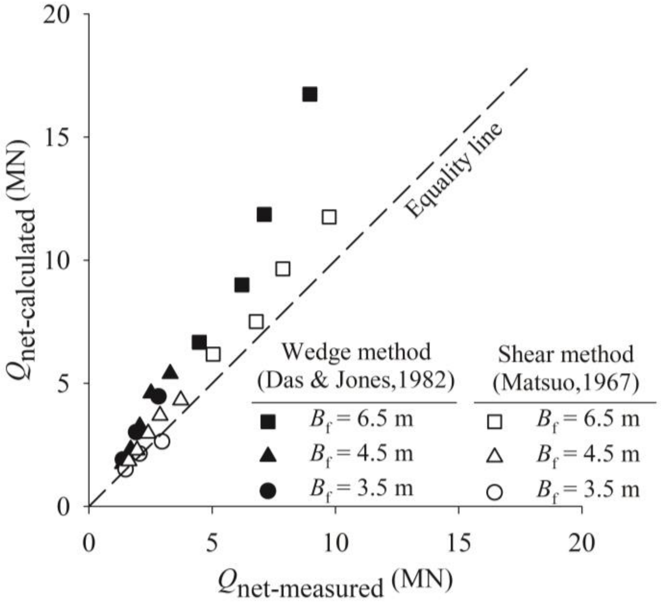

Fig. 4.2 Comparison of $Q_{net}$ between measurement and calculation by existing methods

The measured values of $Q_{net}$ of spread foundations included the side resistance of the foundation slab ($f_f$ in Fig. 1.2), which is different from those of anchor plates because of its negligible plate thickness. The side resistance unit can be calculated by the production of overburden pressure ($0.5\gamma(D_s+D_f)$), lateral earth pressure coefficient ($1-\sin\phi$), and friction coefficient ($\tan0.655\phi$, which followed Section 3.3). The side resistance, which is equal to the side resistance unit times the bearing area ($4tB_f$), was approximately 10% of the $Q_{net}$. If the side resistance was taken out of the measured $Q_{net}$ in Fig. xx. 8, then the difference between the measurement and calculation of the wedge method would increase.

### 4.3.1 Uplift resistance factor $N_q$

To provide a recommendation for practical design, the net bearing capacity is usually presented in the form of the uplift resistance factor, as follows:

$$N_q = \frac{Q_{\mathrm{net}}}{\gamma B_{\mathrm{f}}^2 D_{\mathrm{s}}} = \frac{Q_{\mathrm{u}} - W_{\mathrm{f}}}{\gamma B_{\mathrm{f}}^2 D_{\mathrm{s}}} \tag{4.1}$$

where $Q_u$=uplift bearing capacity, $Q_{net}$=uplift net bearing capacity, $W_f$=foundation weight, $B_f$=slab width, and $D_s$=embedment depth from the top of the slab to the ground surface (Fig. 1.2).

To support the analysis of $N_q$, the centrifuge test data along with the 1g model test results in dense sand were included in the interpretation of the present study, as shown in Fig. 4.3. Kananyan (1966) carried out a field test on equivalent square foundation with $B_f$ of 0.7 and $D_s/B_f$ of 1.4. The 1g model tests and centrifuge tests results were reported by Ovesen (1981), Dickin (1988), and Tagaya et al. (1988) for horizontal anchors with different widths and embedment depth ratio. Data reported by Das & Jones (1982) were obtained from experiments on rectangular anchors in sand with a base width of 50.8 mm and embedment depth ratios of 1–10. Ilamparuthi et al. (2002) investigated the uplift behavior of a circular anchor plate with a diameter of 0.1–0.4 m at several embedment depth ratios.

Figure 4.3 describes the variation in $N_q$ with respect to the slab width $B_f$ and embedment depth ratio $D_s/B_f$. Data selected from previous studies were limited to an embedment depth ratio of 3 for a comparative discussion. For the comparison, the diameter of a circular foundation of previous studies was converted to an equivalent width of a square foundation. The fitting curve included in the Fig. 4.3 represents the trend of change in $N_q$ at a certain $D_s/B_f$ (Fig. 4.3a) or $B_f$ (Fig. 4.3b). The values of $N_q$ increased with the increase in embedment depth ratio, which is similar to the previous studies. On the contrary, $N_q$ reduced with large slab width considering the same embedment depth ratio. Thus, the scale effect still existed at shallow depth and became significant at deep depth.

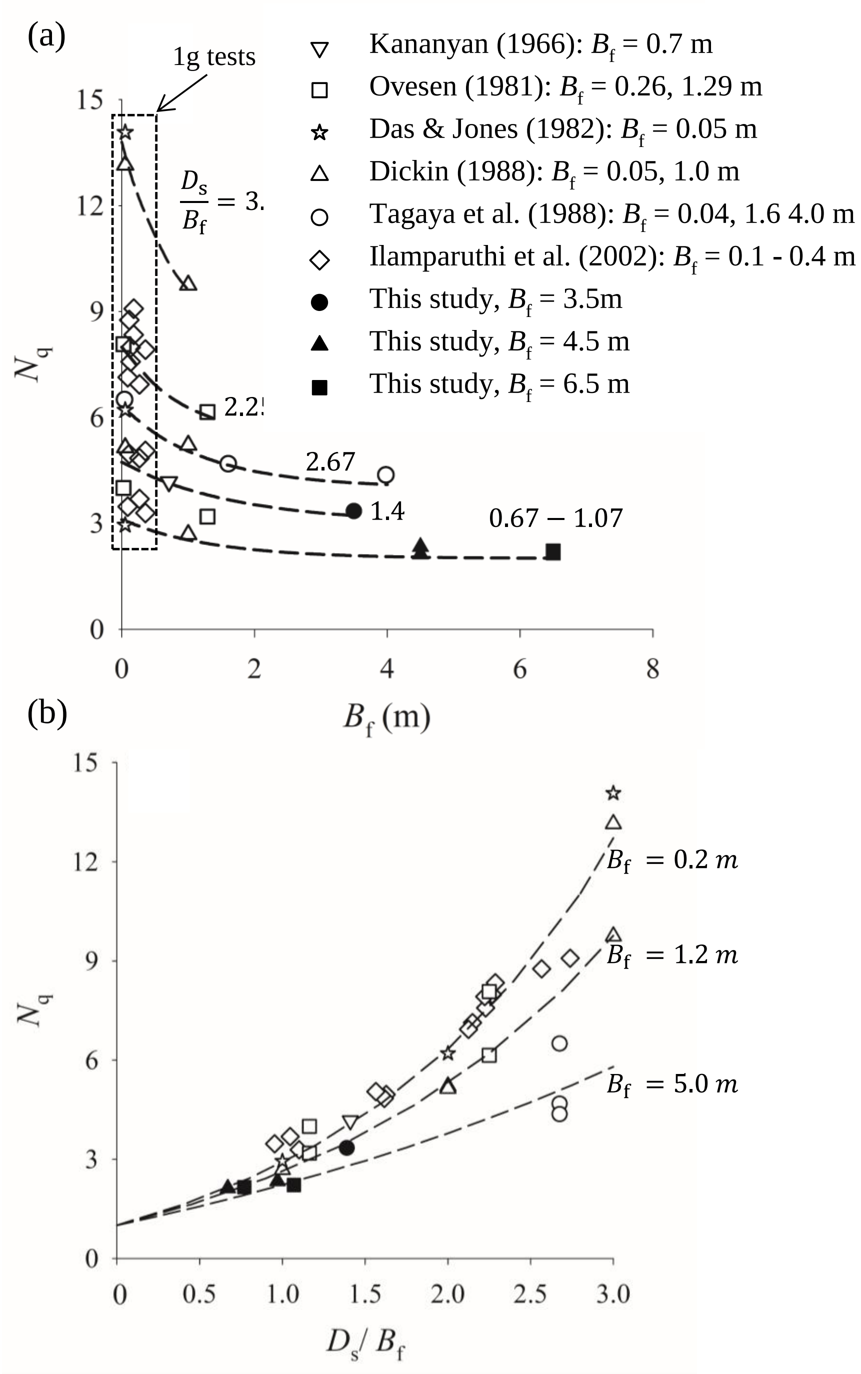

Fig. 4.3 Effect of (a) slab width B<sub>f</sub>, (b) embedment depth ratio $D_s/B_f$ on uplift resistance factor $N_q$ in dense sand.

To account for the scale effect in the determination of $N_q$, a new empirical formula was developed by adopting a machine learning technique with the use of genetic programming for symbolic regression. The genetic analysis was mainly performed using the gplearn package available in the Python library. The governing variables were specified on the basis of the input data, as shown in Fig. 4.4. Then, the genetic analysis was run after setting several symbolic regression parameters manually. A vast number of potential equations were produced at each run. The comparison between the expected and measured values was evaluated to assess the effectiveness of these equations. If the coefficient of determination of the comparison was larger than a reasonable value of 0.8, then the genetic analysis would be terminated with the corresponding equation preferred. Otherwise, the solution was iterated by isolating the insensitive combination forms of the governing variables from a potential equation, which was identified according to the engineering judgment.

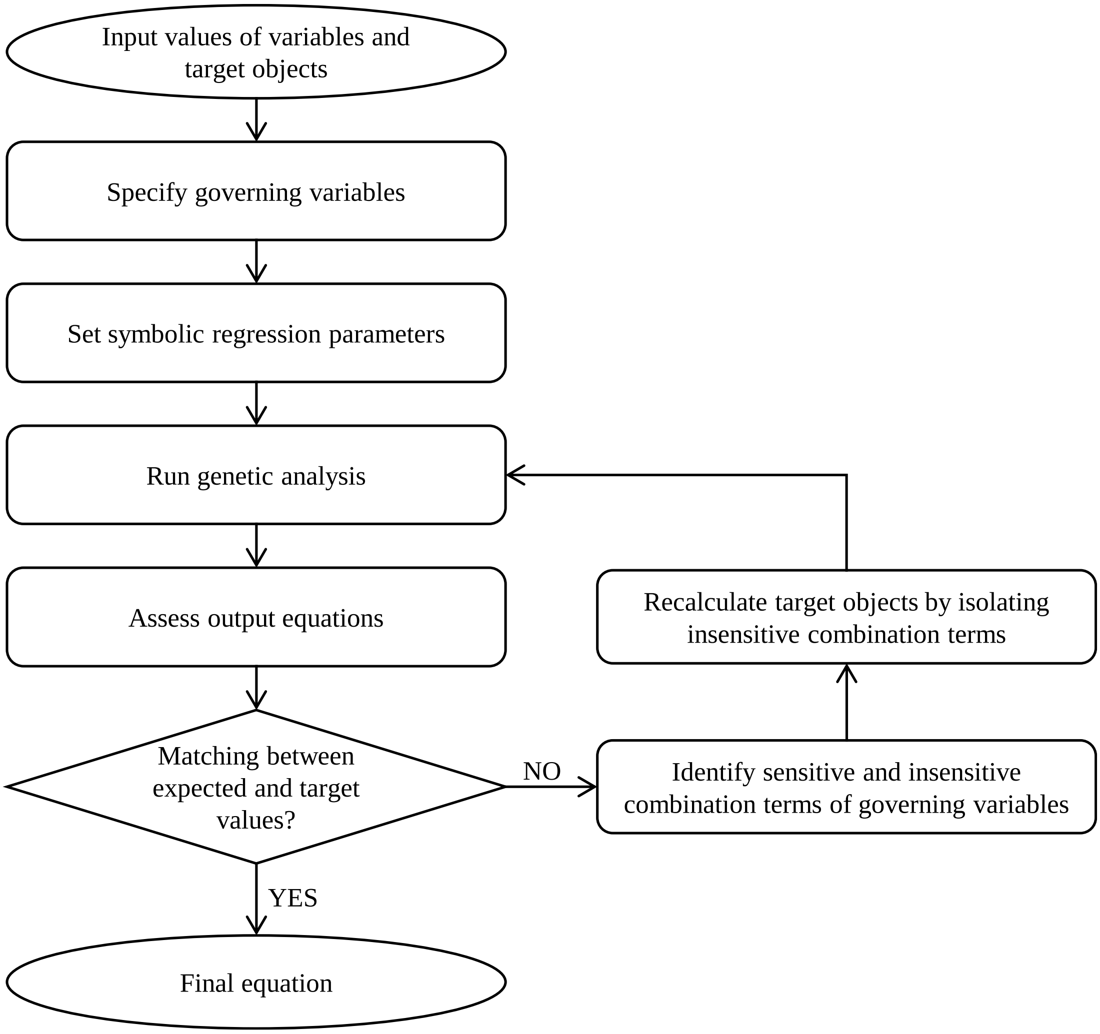

Fig. 4.4 Procedure for developing empirical equation of target object ($N_q$) using genetic programming

The variables governing the behavior of $N_q$ included the slab width $B_f$, embedment depth $D_s$, and strength parameter of soil (friction angle for cohesionless soil) based on the discussion above. As reported by many existing studies, a potential formulation to calculate $N_\mathrm{q}$ might be expressed as follows Das & Jones (1982) and Murray & Geddes (1988):

$$N_\mathrm{q} = 1 + \lambda \frac{D_\mathrm{s}}{B_\mathrm{f}} \tan\phi \tag{4.2}$$

where $\lambda$ is the empirical factor derived from the genetic analyses given as follows:

$$\lambda = \sin\phi + \frac{[D_\mathrm{s}]^{0.75}}{B_\mathrm{f}} \tan\phi \tag{4.3}$$

where $D_\mathrm{s}$ and $B_\mathrm{f}$ in Eqs. (4.2) and (4.3) should be in m.

Figure 4.5 shows the applicability of the proposed equation to estimate the uplift resistance factor by comparing it with the data obtained from the present and previous studies. The average error in estimating $N_\mathrm{q}$ using the proposed equation was approximately 9.5% (data of the current study) and 21% (data of previous studies). The high value of the coefficient of determination of 0.93 in Fig. 4.5 indicated that the estimated $N_\mathrm{q}$ was in reasonable agreement with the measured one considering various conditions of the foundation width, embedment depth, and soil type.

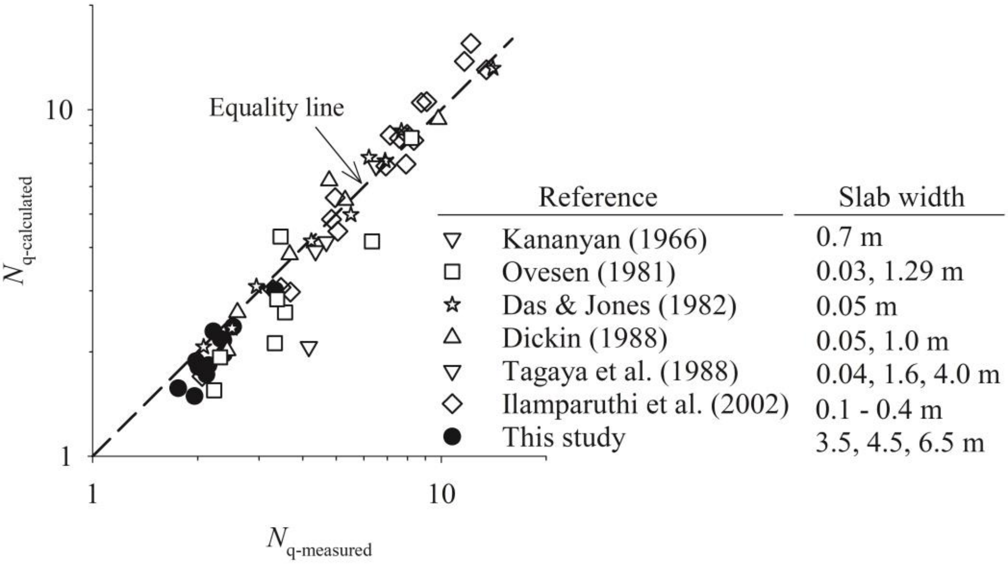

Fig. 4.5 Comparison of $N_q$ between measurement and calculation by proposed equations

Caution is required when applying the suggested equation for $N_q$ to field conditions because the results of this study were obtained from experiments on uniform sandy soil.

## 4.4 Influence zone

Prior to evaluating the uplift bearing capacity, the failure surface should be defined appropriately. The theoretical analysis proposed the shape of the failure surface mostly based on the 1g model tests in which a half-cut model or post-excavation analysis was performed with the use of thin colored layer (Balla, 1961; Ilamparuthi et al., 2002). Recently, a technique of particle image velocimetry (PIV) has been applied to virtually capture the development of the failure surface during uplift loading at 1 g condition (Liu et al., 2012; Zhang et al., 2019; Zhuang et al., 2021). As discussed above, the 1g model tests might fail to simulate the in-situ stress and associated strength of the ground. As discussed above, the 1g model test might be hard to simulate the in-situ stress associated strength of the ground. The set-up of the PIV technique in the centrifuge model remains a challenge in geotechnical research. Therefore, this study attempted to indirectly characterize the failure surface through a concept of influence zone, which was an outer boundary of the failure surface (Liu et al., 2012).

In this study, the influence zone was defined as the soil range from the center of the spread foundation to a certain extent, where the ground surface displacement under uplift loading was negligible. Figure 4.6 shows a typical ground surface displacement measured by the 2D laser profiler for a spread foundation with a slab width of 6.5 m and embedment depth ratio of 1.3 The measurement of the 2D laser profiler was in excellent agreement with that of the laser displacement sensor (several points), thereby confirming its applicability in reasonably capturing the ground surface displacement. The heaving of the ground surface was maximum at and reduced far away from the center foundation. The range of diminishing the ground surface heaving, which indicated the influence zone, was dependent on the magnitude of the uplift load.

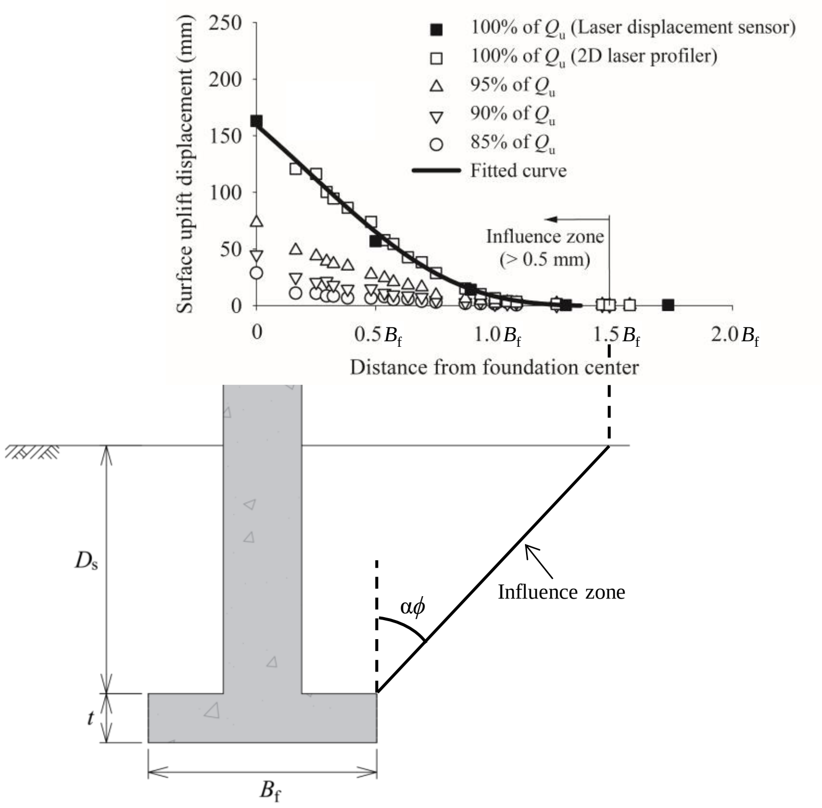

Fig. 4.6 Evaluation of influence zone based on measurement of surface uplift displacement for Case 12 with $B_f$=6.5 m, $D_s/B_f$=1.07, and $D_r$=80%.

The upper boundary of the influence zone at the peak load $Q_u$ was found approximately from 1.0 $B_f$ to 1.5 $B_f$ at which the ground surface heaving was less than 0.5 mm in the prototype scale (Fig. 4.6). This criterion was selected in consideration of the measurement repeatability of all tests and the precision of the

2D laser profiler. The lower boundary of the influence zone was assumed to be the top outermost of the slab. Finally, the suggested influence zone was established by simply connecting the lower to the upper boundary. In this analysis, the ground surface heaving at the center of the foundation was set the same as the uplift displacement of the foundation.

Figure 4.7 presents the simplified empirical influence zone against variation in the soil density, slab width, and embedment depth. The angle of the influence zone relative to the vertical line for Loose sand was approximately 0.9 $\phi$ regardless of the foundation dimensions, whereas that for dense sand increased from 0.8 $\phi$ to 1.2 $\phi$ together with the increase in the embedment depth (Fig. 4.7a and 4.7b). Table 4.2 shows the values of $\alpha$ for all cases of this study ($\alpha$=0.8–1.2). The change in the influence zone for dense sand can be the effect of volume expansion induced by high confinement pressure at deep depth. Therefore, the simplified empirical influence zone can be expressed in terms of the production of a constant $\alpha$ and soil friction angle $\phi$, i.e. $\alpha\phi$. An average value of $\alpha$ can be considered at approximately 0.9 for different types of sand. The field results of Kananyan (1966) with the slab width less than 1.2 m showed that an average of $\alpha$ was approximately 0.7. Experimental results at 1 g condition of Liu et al. (2012) revealed $\alpha$ of approximately 0.5 from the analysis of digital image correlation. The previous findings of $\alpha$ were lower than the suggested values because their experiments with the small slab width at the 1 g condition might not reasonably simulate the stress state, stress dependency, and the progressive failure of the prototype problem.

In the process of designing and maintaining soil structures that may experience uplift forces, it is imperative to consider the extent of the zone of influence on the stability of neighboring structures.

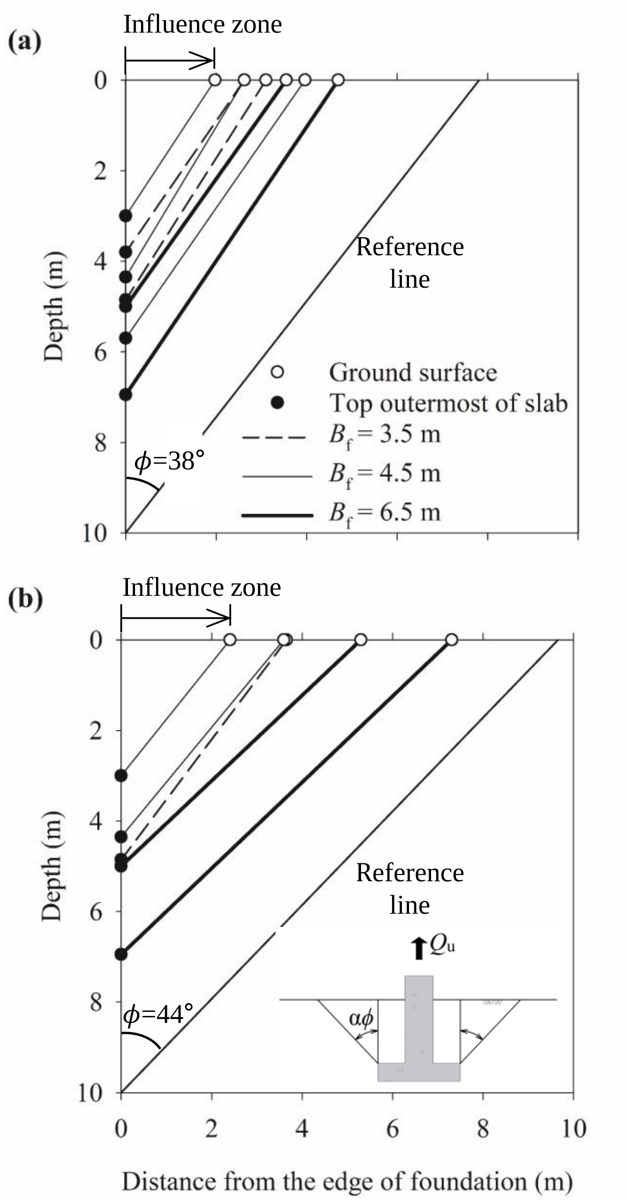

Fig. 4.7 Simplified empirical influence zone: (a) medium sand, (b) dense sand

Table 4.2 Values of constant α in the determination of influence zone

| Case | $D_r$ (%) | $B_f$ (m) | $D_s$ (m) | $\alpha$ |
|---|---|---|---|---|
| 1 | 40<br>(Loose) | 3.5 | 3.80 | 0.91 |
| 2 | | 3.5 | 4.85 | 0.86 |
| 3 | | 4.5 | 3.00 | 0.88 |
| 4 | | 4.5 | 4.35 | 0.81 |
| 5 | | 4.5 | 5.70 | 0.92 |
| 6 | | 6.5 | 5.00 | 0.94 |
| 7 | | 6.5 | 6.95 | 0.89 |
| 8 | 80<br>(Dense) | 3.5 | 4.85 | 0.84 |
| 9 | | 4.5 | 3.00 | 0.87 |
| 10 | | 4.5 | 4.35 | 0.90 |
| 11 | | 6.5 | 5.00 | 1.06 |
| 12 | | 6.5 | 6.95 | 1.05 |

Fig. 4.8 illustrates the position of the simplified empirical influence zone relative to the failure surface as recommended by existing studies. The influence zone and failure surface have different shapes because of their distinct concepts. The failure surface provided by Meyerhof & Adams (1968) showed approximately a straight line because it represented the case of shallow failure mode. The failure surface was proposed as a spiral curve by Balla (1961) and Matsuo (1967) and Meyerhof and Adams (1968) showed a close correlation to the proposed influence zone of this study. However, the near-ground surface segment of the failure surface recommended by Matsuo (1967) lied outside of the simplified empirical influence zone because Matsuo assumed a straight line at the upper part of the failure surface. Nevertheless, all recommended failure surfaces mostly lied within the simplified

empirical influence zone, indicating that the suggested influence zone could be used as a reference for predicting the failure surface of the spread foundation under uplift loading.

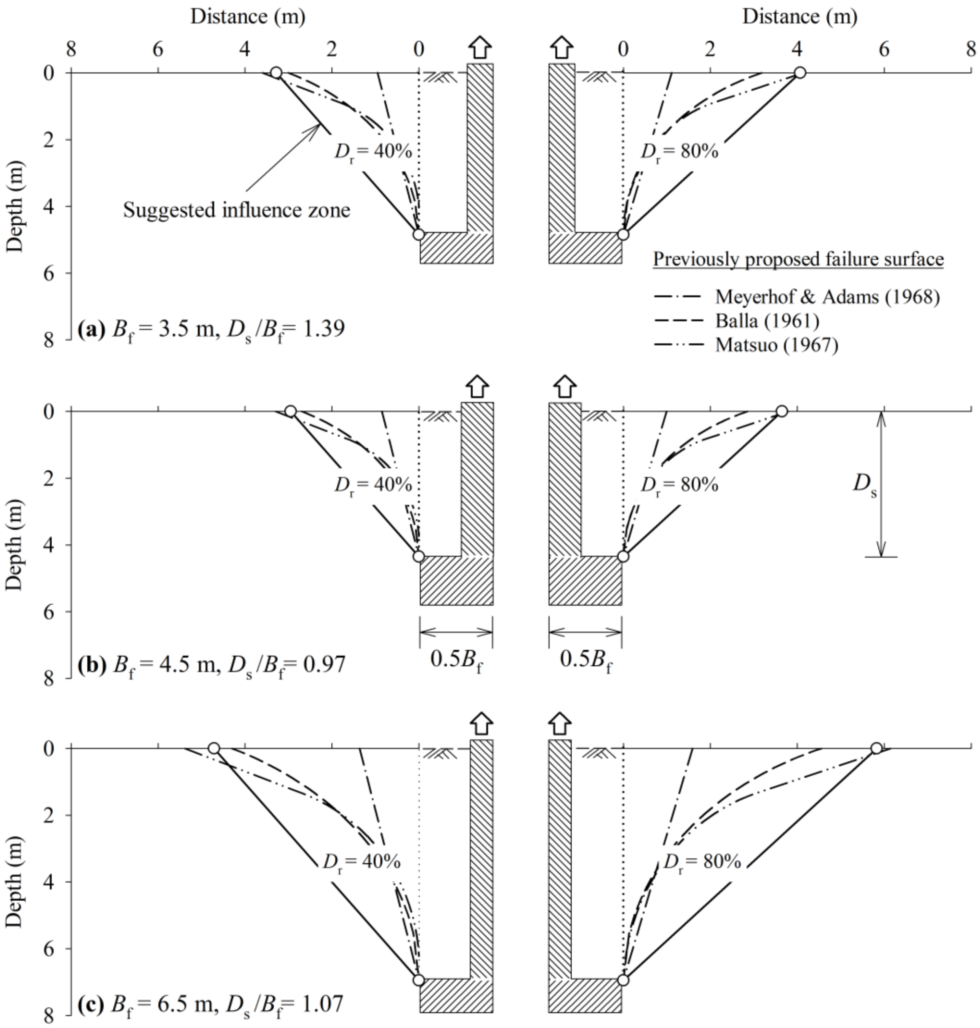

Fig. 4.8 Relationship between simplified empirical influence zone and failure surface recommended by existing studies ($D_r$ = 40% at left side and $D_r$ = 80% at right side, foundation dimensions not to scale)

## 4.5 Peak displacement

Regarding the performance criteria of the transmission structures supported by spread foundations, the uplift displacement $w_p$ at peak load $Q_u$ is one of the most important considerations in the general limit state design (IEEE, 2001). The uplift bearing capacity of the spread foundation might be mobilized within a relatively low level of the uplift displacement. Therefore, the failure and damage limit of the transmission structures should be appropriately defined on the basis of the input of $w_p$ and $Q_u$ to satisfy the stability in terms of strength and deformation. The behavior of $w_p$ is presented in this section.

Fig. 4.9 illustrates the ratio of the uplift displacement to the slab width $w_p/B_f$ with respect to the relative shaft diameter $B_s/B_f$ in dense sand. The same data sets of Dickin (1988) and Ilamparuthi et al. (2002) are included in the Fig. 4.9 for comparison. Results of centrifuge tests on 0.89 m equivalent square bell piles by Dickin & Leung (1992) were also adopted. The fitting curves of $w_p/B_f$ at a certain embedment depth ratio were derived according to the trend of the collected data. The values of $w_p/B_f$ decreased with the increase in $B_s/B_f$. This relationship was more pronounced at deep depth due to large mobilized strength as reported by Dickin & Leung (1992). The justification for the reason of this phenomenon requires further studies. Moreover, $w_p/B_f$ increased with large $B_f$ according to the large bearing area. In addition, the values of $w_p/B_f$ obtained from 1 g tests were considerably smaller than those from the centrifuge results because the sandy soil shows a “dense state” behavior at the low confining stress. As shown in Section 4.2, $w_p/B_f$ for dense sand was lower than that in the medium sand (Fig. 4.1).

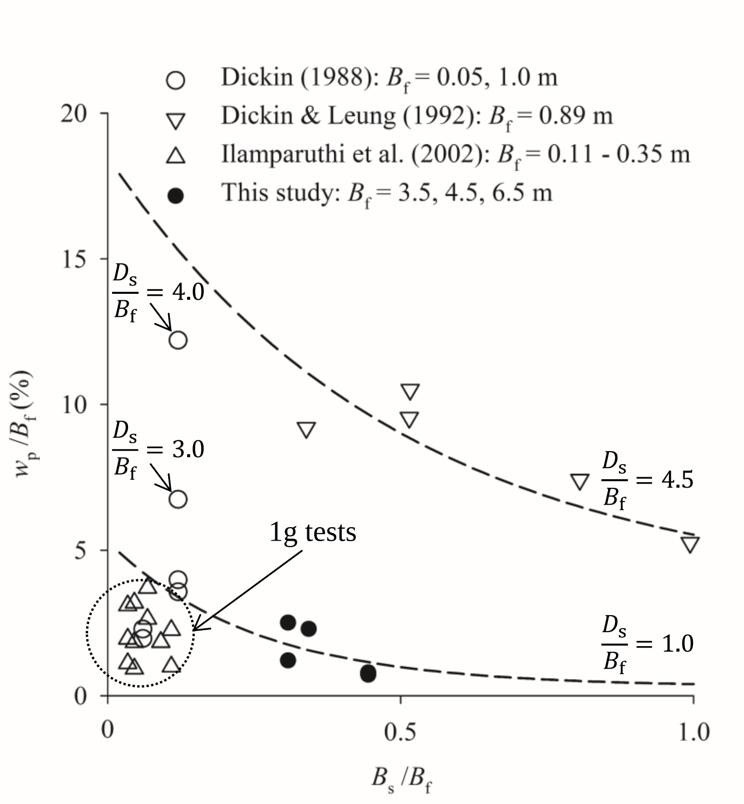

Fig. 4.9 Effect of relative shaft diameter $B_s/B_f$ on dimensionless uplift displacement $w_p/B_f$ at peak load $Q_u$ in dense sand

The preceding discussion indicates that the variables governing the behavior of $w_p$ could be the embedment depth, slab width, and shaft width. The genetic analysis was therefore applied to propose an empirical formulation of calculating $w_p$ with respect to these governing variables, as follows:

$$w_p = 1.6(N_w)^{0.9} \tag{4.4}$$

$$N_w = \frac{B_\mathrm{f}}{B_\mathrm{s}}\left(\frac{D_s}{D_{ref} \times \tan\phi}\right)^2 \tag{4.5}$$

where $N_\mathrm{w}$ is the functional displacement factor, $B_\mathrm{s}$ is the diameter of the shaft, and $D_\mathrm{ref}$ is the reference depth of 1 m.

The proposed formula of $w_p$ was verified with previous data provided by Ilamparuthi et al. (2002) and Dickin (1988) in which the embedment depth ratio was less than 3. Another set of field data of the uplift displacement could be found in the study of Trautmann & Kulhawy (1988). However, their data were derived using a tangent method by which the determined uplift displacement was incomparable with those of this study. Fig. 4.10a shows the relationship between $w_\mathrm{p}$ and $N_\mathrm{w}$. Parameters required to determine $N_\mathrm{w}$ (Eq. (4.5)) were $B_\mathrm{s}$, $B_\mathrm{f}$, $D_\mathrm{s}$, and $\phi$, which were adopted directly from the existing studies. The coefficient of determination in Fig. 4.10a is approximately 0.92, indicating a high correlation of exponential relationship between $w_p$ and $N_w$ as suggested by Eq. (4.4). In addition, the calculated value of $w_p$ was in a reasonable agreement with the measured one, thereby verifying the proposed equations of $w_p$, as shown in Fig. 4.10b.

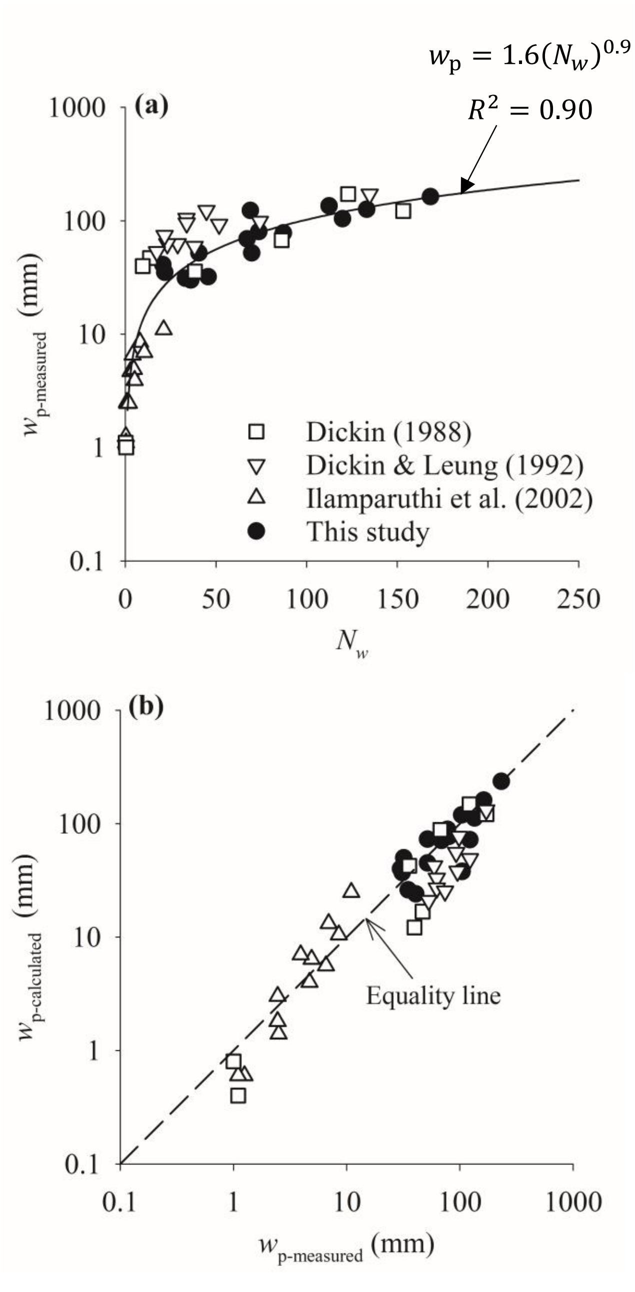

Fig. 4.10 Verification of developed formulation to estimate the uplift displacement $w_p$ at peak load $Q_u$

## 4.6 Summary

This study analyzed the uplift behavior of spread foundations in sandy soil through a series of centrifuge tests. The uplift bearing capacity and the corresponding uplift displacement were evaluated in terms of the slab width, embedded depth, and soil density. The scale effect was extensively explored by adopting the previously reported data mostly under 1g model test condition. Suggestions on the uplift bearing capacity, uplift resistance factor, and uplift displacement were provided for practical design. Some major conclusions are as follows.

1. The uplift load–displacement curve obtained from centrifuge tests by means of a displacement controlling method showed hardening behavior within a relatively small displacement and softening behavior after attaining a peak. The uplift bearing capacity $Q_u$ determined a peak point increased with larger slab width, deeper embedment depth, and denser sandy soil. The existing methods were not successful in estimating the net uplift bearing capacity $Q_{net}$ of the spread foundations tested in this study due to the scale effect.
2. By reasonably simulating the in-situ stress conditions, the uplift resistance factor Nq of the spread foundation were observed to become smaller with large slab width at a certain embedment depth ratio compared with the 1g model test results. Dimensionless uplift

displacement $w_p/B_f$ decreased with the increase in the relative shaft diameter $B_s/B_f$. These phenomena were more pronounced at large embedment depth ratios.

3. Empirical formulations of $N_q$ and $w_p$ were proposed by adopting genetic programming for symbolic regression. The scale effect was covered in these empirical equations by analyzing the governing variables independently, such as the slab width, embedment depth, shaft width, and soil friction angle. The proposed equations were capable of estimating the values of $N_q$ and $w_p$ under various conditions reported in the literature and thereby verifying their high applicability in the preliminary design consideration of spread foundations.
4. A simplified empirical influence zone was proposed on the basis of the measurement of the ground surface displacement. The proposed influence zone was a straight line connecting the top outermost of the slab to the point at the ground surface with negligible heaving. Generally, the empirical influence zone made an angle of approximately 0.9 $\phi$ (where $\phi$ is the soil friction angle) relative to the vertical line. It was proved that the proposed influence zone could be

considered a significant reference for predicting the failure surface of the spreading foundation under uplift loading.

# Chapter 5. Analysis of failure mechanisms using PIV

## 5.1 Introduction

As mentioned in Chapter 2, the failure surface is essential to evaluate the uplift bearing capacity. The failure surface is formed according to the confining pressure, soil density, and the geometry of the foundation. Half-cut model experiments, which the PIV technique was applied are performed for failure surface analysis.

In this chapter, a series of half-cut model tests in centrifuge were performed to characterize the failure surface. The test results of half-cut foundation model tests in centrifuge and the analyses of uplift failure mechanisms of shallow spread foundations were presented. The uplift behavior of half-cut model test is similar with full model tests by comparing with vertical displacement of the ground surface. Failure surface was determined from the development of vertical displacement using PIV methods. In order to simplify the identified failure surface, it was expressed in a bilinear form, and the empirical formulation for failure surface was proposed through machine learning by analyzing influencing factors to the failure surface. Finally, the proposed failure surface was compared with the previously suggested failure surface.

## 5.2 Test results

### 5.2.1 Load-displacement curves

Figure 5.1 illustrates the uplift load–displacement curves obtained from the centrifuge half-cut model tests. The uplift load–displacement curve consisted of three components corresponding to the uplift displacement magnitude, namely, linear elastic, hardening, and softening segments similar with curves obtained from the centrifuge full model tests.

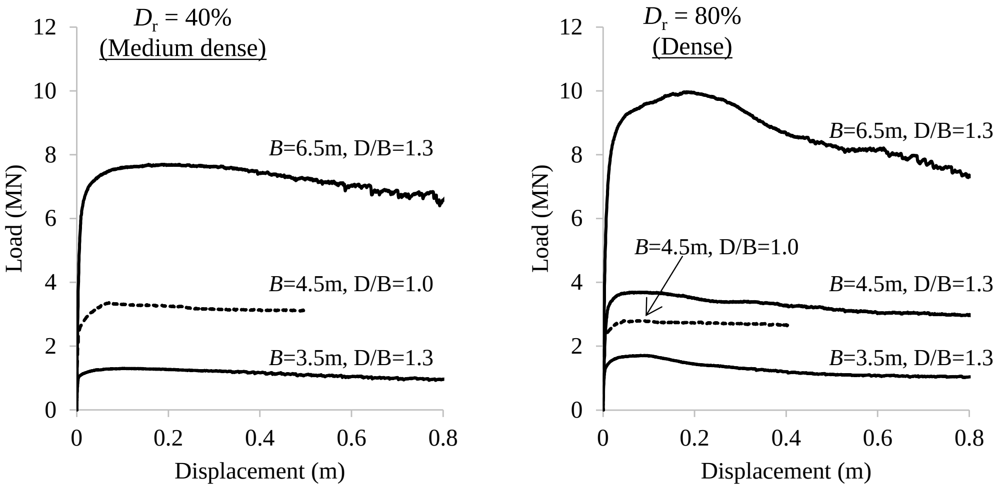

Fig. 5.1 Load-displacement curves of Half-cut model in centrifuge

### 5.2.2 Verification and comparison

The curves from the half cut-model and Full model tests results were plotted in Fig. 5.2. Half-cut model tests have similar shape of the curve with the full model test ($B_f$=3.5, $D_s/B_f$ =1.3, $D_r$ = 40%). However, the peak load of half-cut model results is much Higher than that of the full model. This discrepancy is because uplift resistance of half-cut model includes additional friction from that of window-soil and window-soil-foundation which increase with lateral earth pressure.

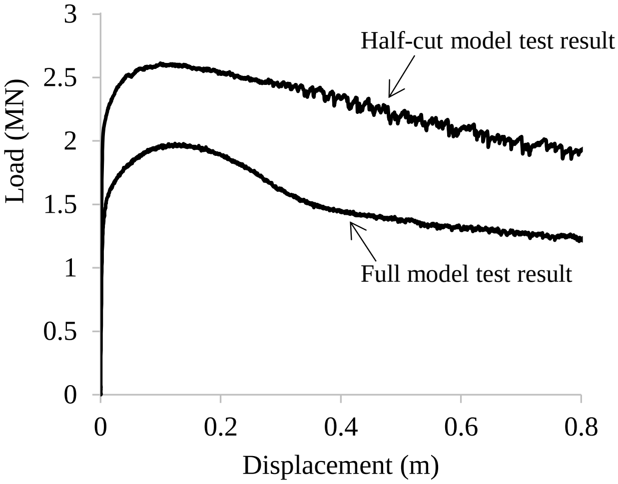

Fig. 5.2 Comparison with full model and half-cut model of load-displacement curves

In order to compare the experimental results of full model centrifuge tests and half-cut model, the ground profile was obtained by placing with a spacing of 1.35m (prototype) from the foundation edge. The results of the full model and the half-cut model under the same ground and foundation conditions are shown in Fig. 5.3. It shows the distribution of ground uplift vertical displacement similar to the ground displacement of the full model, and shows an approximately largest error of 10%.

Since the load-displacement curves are similar and the ground displacement at peak load is similar, it was concluded that the uplift behavior of the full foundation model can be simulated through the behavior of the half-cut model.

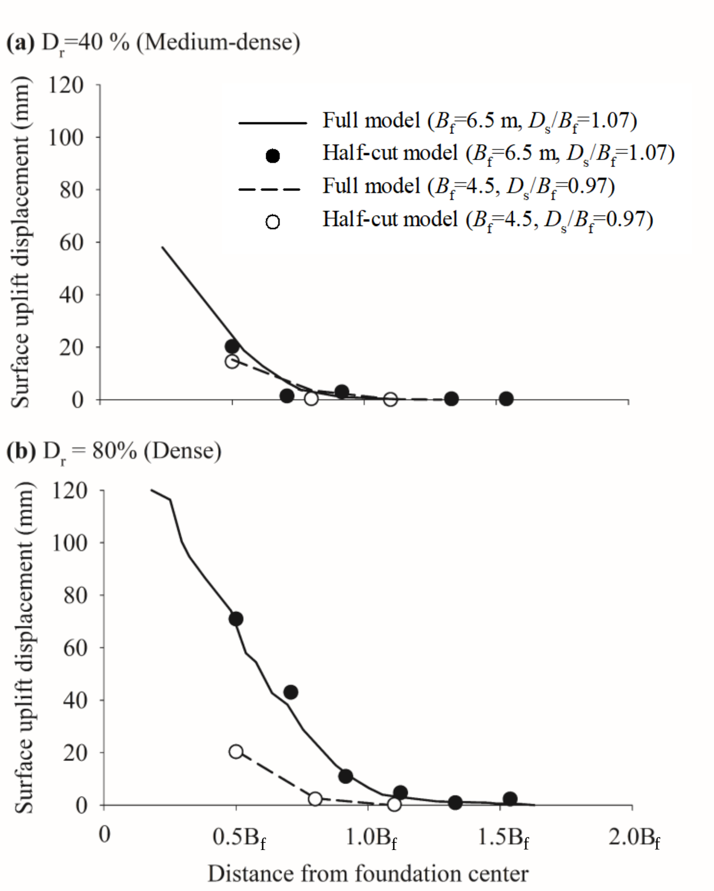

Fig. 5.3 Comparison with vertical displacement of full model and half-cut model in centrifuge

## 5.3 Failure surface

This section presents distribution of soil displacement during uplift in uniform silica sands. The purpose of this image analysis using GeoPIV software understands and analyzes the uplift failure mechanism. The value of the analysis is expressed in prototype scale.

Previous studies reported that a failure surface is mobilized from the edge of the foundation slab to the ground surface with different patterns of circular, logarithmic, and linear shapes (Balla, 1961; Deshmukh et al., 2010; Matsuo, 1967; Meyerhof & Adams, 1968). Precise analyses with the application of a PIV technique have demonstrated that the failure surface is nearly linear near the foundation slab and curves outward near the ground surface (Cheuk et al., 2008; Huang et al., 2015).

### 5.3.1 Characterization of failure surface

The boundary where the vertical displacement begins to decrease and ground displacement does not occur is defined as the shear zone. (Cheuk et al., 2008). Ilamparuthi et al. (2002) and Yang et al. (2020) defined the point where no displacement occurs as the failure surface. The boundary of the shear zone by Cheuk et al. (2008) can be represented by connecting the approximate average 10% of the maximum vertical displacement at the corresponding depth, and that point becomes the point that connects the inflection point where the rate of decrease of vertical displacement changes. In this experiment, the experimental results with a foundation width of 3.5 m and a depth-width ratio of 1.3 are shown in the vertical displacement distribution at each depth in Fig. 5.4. The failure surface was determined by using the vertical displacement distribution at different depths, based on the research results of Ilamparuthi et al. (2002) and Cheuk et al. (2008). Normalized the maximum vertical displacement to the foundation displacement and scaled it to 0.5m to describe the vertical movement. The profile of vertical displacement for every 0.5m depth is shown in Fig. 5.4. The ground vertical displacement decreases as the distance from the center of the foundation increases.

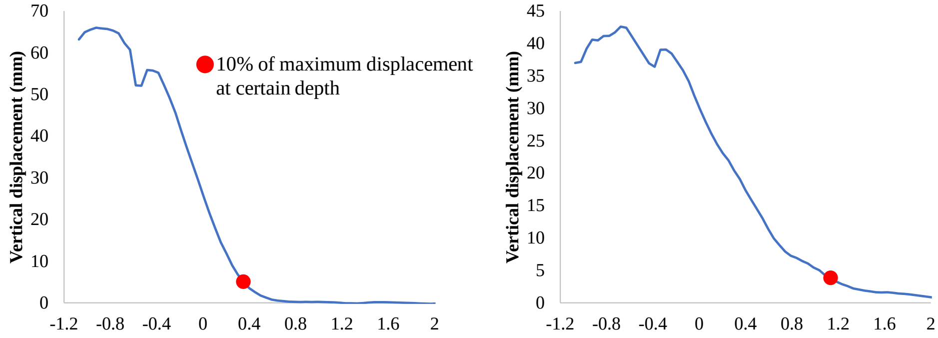
(a) at 1.0m height, Dense

(b) at 3.6m height, Dense

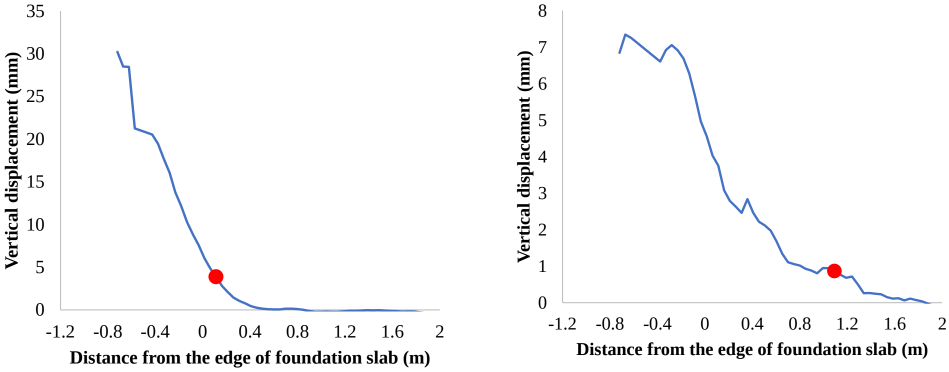
(c) at 1.0m height, Loose

(d) at 3.6m height, Loose

Fig. 5.4 Determination of failure surface based on vertical displacement profile from Case 13 and 16 with $B_f$=3.5 m, $D_s/B_f$=1.09, and $D_r$=40 and 80%.

### 5.3.2 Bilinear failure surface

As shown in Fig. 5.5, lines representing the point corresponding to 10% of the maximum vertical displacement at each depth and the profile of the vertical displacement at each depth are depicted. Lines are defined as failure surface and could be roughly simplified into a bilinear form. The failure surface near the foundation slab is linear and close to vertical, and it becomes wider as it approaches the ground surface.

Matsuo (1967) divided into two section of failure surface according to the earth pressure acting on the failure surface: (1) vicinity of foundation slab; (2) region of ground surface. The angle between the destructive surface and the surface of the earth has been proposed at $45-\phi/2$ (Balla, 1961; Matsuo, 1967).

Based on Analysis of Matsuo (1967), the failure surface is shown on the foundation, and the failure surface is expressed as an angle by $\theta_a$, which represents the active failure surface, and $\theta_p$, which represents the passive failure surface. These angles of bilinear failure surface were average values of left side and right side of the foundation and summarized in Table 5.1.

The failure surface near the slab is defined as an active failure surface, while the failure surface near the ground surface is defined as a passive failure surface. Based on analysis of bilinear failure surface, the failure surface is shown on the foundation, and the failure surface is expressed as an angle by $\theta_a$, which represents the active failure surface, and $\theta_p$, which represents the passive failure surface.

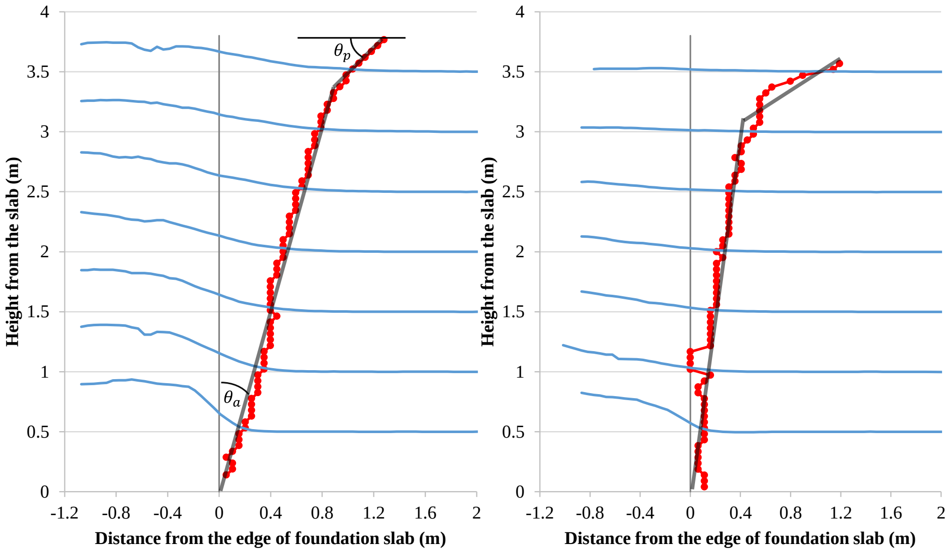
(a) $B_f$=3.5m, $D_f/B_f$=1.3, Dense

(b) $B_f$=3.5m, $D_f/B_f$=1.3, Loose

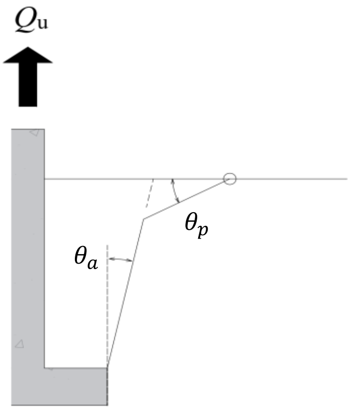
(c) angle of active and passive failure surface

Fig. 5.5 Defined failure surface based on the vertical displacement from Case 13 and 16 with $B_f$=3.5 m, $D_s/B_f$=1.09, and $D_r$=40 and 80 %.

The $\theta_a$ is formed between 7.5 and 15 degrees from the vertical near the slab of foundation, which is defined as active failure surface. The $\theta_p$ is similar to a 45- $\phi$/2, which is similar to the angle of passive failure of the ground and the analysis of Matsuo (1967). These angles of bilinear failure surface were average values of left side and right side of the foundation and summarized in Table 5.1.

Table 5.1 The active and passive failure surface angle

| Case | $D_r$ (%) | $B_f$ (m) | $D_s$ (m) | $D_s/B_f$ | $\theta_a$ (°) | $\theta_p$(°) |
|---|---|---|---|---|---|---|
| 1 | 40<br>(Loose) | 3.5 | 3.80 | 1.09 | 5.9 | 24.9 |
| 2 |  | 4.5 | 3.00 | 0.67 | 7.8 | 25.5 |
| 3 |  | 6.5 | 6.95 | 1.07 | 4.4 | 32.5 |
| 4 | 80<br>(Dense) | 3.5 | 3.80 | 1.09 | 13.1 | 45.0 |
| 5 |  | 4.5 | 3.00 | 0.67 | 10.7 | 20.9 |
| 6 |  | 4.5 | 4.35 | 0.97 | 10.4 | 23.4 |
| 7 |  | 6.5 | 6.95 | 1.07 | 9.38 | 26.9 |

$D_r$=40% and 80% of $\theta_p$ were 26.5° and 23.5 °, respectively

### 5.3.3 Failure surface for analytical solution

Values of the empirical constant $\beta$ were calculated using Eq. (5.1), and the corresponding angle $\theta_a$ increased with high internal friction angles but reduced with large embedment depths. This behavior of $\theta_a$ was consistent with the experimental results of Matsuo (1967).

$\theta_a$ varies according to depth and soil density, and the angle $\theta_a$ of the failure surface to the vertical direction was set to a multiple of the internal friction angle of soil $\beta\phi$. The passive failure surface intersected the ground surface at an angle $\theta_p$ of

45°–$\phi$/2 (Balla, 1961; Matsuo, 1967). In the case of $\theta_p$, the relative density of 40% tends to be smaller than the result of 80%, which is similar to the theoretical angle of 45-$\phi$/2 for passive failure state between the ground surface and the of passive failure surface. Since the angle $\theta_p$ is similar to the angle of the passive failure state proposed in the existing literature, 45-$\phi$/2 was used.

In order to be applied to various foundations and ground conditions, it is necessary to propose an empirical equation for predicting the failure surface. The angle of $\theta_a$ and $\theta_p$, and point P in Fig. 5.6 need to be determined to represent the failure surface theoretically.

A bilinear shape was suggested for the failure surface of the spread foundation in cohesionless soil to consider the recent update and effect of confining pressure at the prototype scale (Fig. 5.6). The bilinear surface was composed of two linear segments, namely, active AT and passive TP failure surfaces. The location of point A was set at the top outermost area of the foundation slab (Balla, 1961; Matsuo, 1967), while those of points T and P were unknown. The soil mass surrounding the foundation shaft moved upward in the vertical direction of the active zone. The lateral movement of the surrounding soil mass became noticeable in the passive zone because the suppression of confining pressure appeared decreasingly. The division of the bilinear failure surface was based on the suggestion of Matsuo (1967) regarding the difference in earth pressure conditions along the embedment depth.

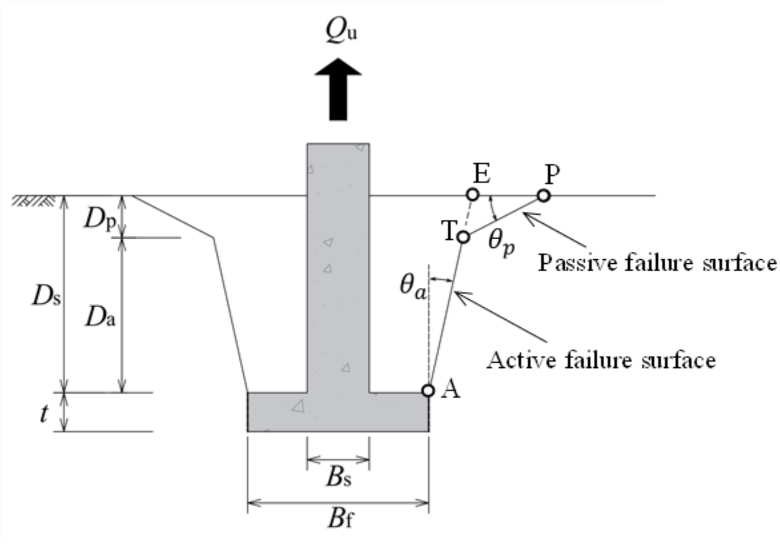

Fig. 5.6 Suggested bilinear failure surface.

The symbolic function of $\beta$ with respect to $D_s$ and $\phi$ was the target object of the genetic analysis given that the angle $\theta_a$ was previously expressed as $\beta\phi$. The final formula of $\beta$, which can yield a satisfactory estimation of $Q_{net}$ for various foundation dimensions, is expressed as follows:

$$\beta = \frac{D_s^{0.4}}{1.5D_s + \sin\phi}\tan\phi \tag{5.1}$$

The active failure surface was then formed by connecting point A to point E. Values of β ranged from 0.18 to 0.51 due to the change in foundation dimensions and soil relative densities, as presented in Table 5.2.

Table 5.2 Comparison of $\theta_a$ with calculated and measured value

| Case | $B_f$ (m) | $D_s/B_f$ | $\beta$ | $\theta_{a\text{-calculated}}$ (°) | $\theta_{a\text{-measured}}$ (°) |
|---|---|---|---|---|---|
| 1 | 3.5 | 1.09 | 0.204 | 8.0 | 5.9 |
| 2 | 4.5 | 0.67 | 0.229 | 9.0 | 7.8 |
| 3 | 6.5 | 1.07 | 0.148 | 5.8 | 4.4 |
| 4 | 3.5 | 1.09 | 0.249 | 10.7 | 13.1 |
| 5 | 4.5 | 0.67 | 0.279 | 12.0 | 10.7 |
| 6 | 4.5 | 0.97 | 0.233 | 10.0 | 10.4 |
| 7 | 6.5 | 1.07 | 0.182 | 7.84 | 9.4 |

In the case of $\theta_a$, the angle increases as the relative density increases, and $\theta_a$ tends to decrease as the depth of the foundation increases. Finally, the empirical constant $\beta$ was determined at an average value of 0.22. Meyerhof and Adams (1968) suggested a similar value of 0.33 according to a small-scale study on the uplift response of circular footings in sand.

Finally, the determination of the position point on the surface of the passive failure surface. Liu et al. (2012) experimentally confirmed that the failure surface was within the influence range, and the results of this experiment showed similar results. As a result of the PIV analysis, when Point P is expressed as an angle, the result is 0.5 to 0.6 phi from the vertical.

As shown in the Fig. 5.10, it was confirmed through the result analysis that Point P exists in the middle of the point a extending the active failure surface from the surface to the surface and the influence zone. Therefore, we determined that the point is located in the center of the point a and the influence zone boundary.

On the basis of the active failure surface derivative, point P of the passive failure surface was assumed located at the center of line EI (Fig. 5.7). The horizontal distance $x_\mathrm{P}$ from the edge of foundations to point P can be calculated as follows:

$$x_\mathrm{P} = \frac{D_\mathrm{s}(\tan\theta_\mathrm{a} + \tan\alpha\phi)}{2} \tag{5.2}$$

where $\theta_\mathrm{a}$=0.35$\phi$ and $\alpha$=0.9.

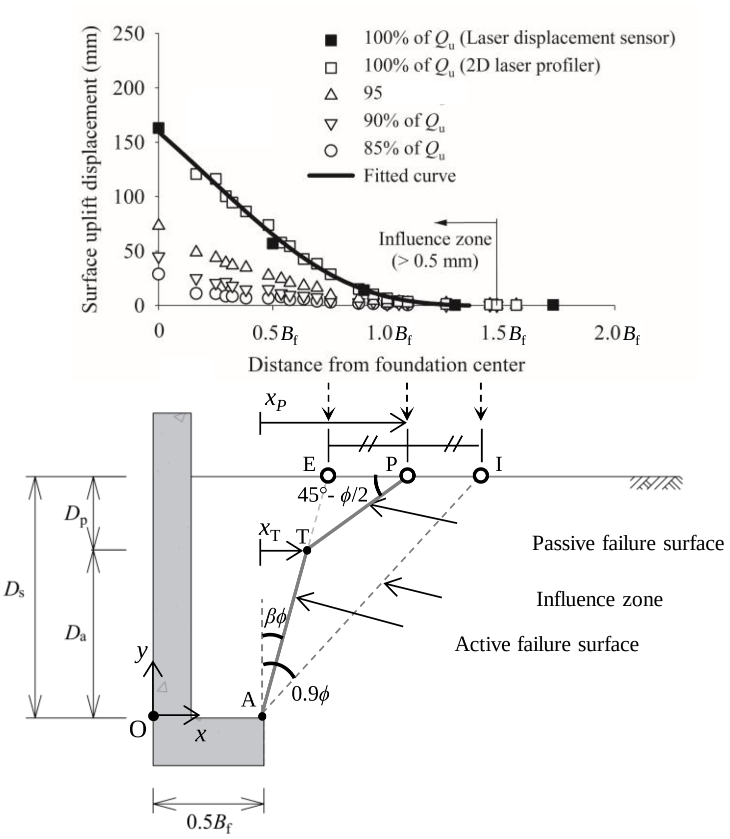

Fig. 5.7 Derivative of suggested bilinear failure surface.

The transition point T between active and passive failure surfaces can be expressed as follows:

$$x_T = \frac{D_s - \tan\theta_p \, x_P}{\tan(45° - \theta_a) - \tan\theta_a} \tag{5.3}$$

$$y_T = \tan(45° - \theta_a) \, x_T \tag{5.4}$$

where $\theta_p$=45°–$\phi$/2.

## 5.4 Comparison with previous researches

The proposed bilinear failure surface was compared with previous recommendations, including the linear curve by Meyerhof and Adams (1968), circular curve by Balla (1961), and composite shape by Matsuo (1967), as shown in Fig. 5.8. The failure surface at the active zone suggested in this study was less steep than existing curves, while the proposed passive failure surface was bounded by these curves. On the basis of the typical small-scale test by Balla (1961), an angle $\theta_a$ of approximately 0.5 $\phi$, was calculated using Eq. (5.1) and observed at the active zone (Fig. 5.8a) similar to the findings of Ilamparuthi et al. (2002). The majority of analytical solutions yielded a satisfactory estimate of $Q_{net}$, except for the method of Matsuo (1967). The value of the suggested angle $\theta_a$ based on large-scale test results was approximately 0.18 $\phi$ (Fig. 5.8b), which was relatively steeper than that recommended in existing studies. This difference may be attributed to the inconsistency of the analysis condition, that is, existing analytical solutions are typically derived from experiments on foundations with dimensions smaller than those applied in this study. Hence, the net capacity $Q_{net}$ estimated by the proposed semi-analytical solution was reasonable compared with other existing methods (Fig. 5.8b).

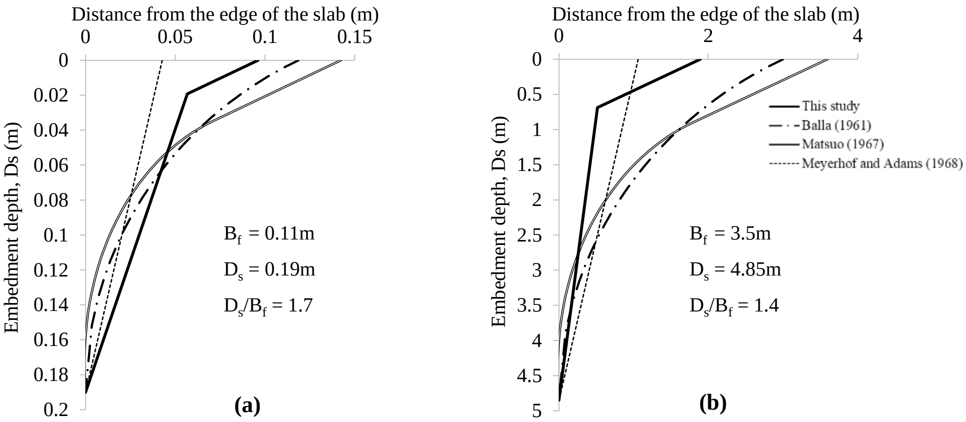

Fig. 5.8 Comparison of failure surface and $Q_{net}$ between the proposed and existing analytical solutions: (a) small-scale test of Balla (1961) and (b) large-scale of this study.

## 5.5 Summary

In this chapter, the uplift failure mechanisms of shallow spread foundation were analyzed using the PIV method. The uplift behavior of the full foundation model can be simulated through the behavior of the half-cut model. The curved failure surface which used to estimate the uplift bearing capacity was identified. Bilinear shape of failure surface was characterized. The main conclusion can be summarized as follows.

1. Since the shape of the load-displacement curves and the vertical displacement on the ground surface under peak loads were similar, it was concluded that the uplift behavior of the half-cut model describes the full foundation model properly.
2. The failure surface was determined from the vertical displacement profile at each depth and by connecting the points where the maximum vertical displacement was 10%. The failure surface curves near the foundation slab and near the ground surface were almost linear lines which have different inclination. The higher the density of the ground and the deeper embedment depth of the foundation, the greater the angle formed with the vertical line. The failure surface near the surface of the ground was similar to the inclination of the angle in the passive failure mode.
3. The suggested bilinear failure surface based on the measured uplift displacement of the ground surface was capable of capturing different failure mechanisms along the depth of the spread foundation, including a

passive mode near the ground surface and an active mode downward. Therefore, the failure surface was expressed in a bilinear form. Determination of parameters to characterize the bilinear failure surface was enhanced when a genetic programming method based on a symbolic regression technique was adopted.

# Chapter 6.Semi-Analytical solution of uplift bearing capacity

## 6.1 Introduction

As mentioned in Chapter 2, the curved surface method is realistic approach to estimate uplift bearing capacity in design. The methods suggested by previous researchers were developed based on the 1g reduced-scale model tests. Considering scale effect, the estimated uplift bearing capacity be preciously suggested could overestimate.

In this chapter, the semi-analytical solution for the uplift bearing capacity was derived based on the test results of Chapter 4 and 5. The slice method was adopted to calculate the shear resistance along the failure surface. The suggested solution was verified with the current centrifuge tests results and previously performed tests results.

## 6.2 Semi-analytical solution

In the present study, the semi analytical solution for the net uplift bearing capacity will be proposed based on centrifuge test results and suggested bilinear failure surface, as shown in Fig 6.1. The followings are assumed in the proposed analytical solution (Balla, 1961; Matsuo, 1967; Meyerhof & Adams, 1968):

1) The failure surface is symmetrical
2) A trapezoid failure surface was assumed

3) The frictional force does not occur along the shaft of the foundation.

Most analytical and semi analytical solution assumed symmetrical failure surface and trapezoid failure surface surrounding the foundation. In addition, the shear resistance on the shaft is ignored (Balla, 1961; Matsuo, 1967; Meyerhof and Adams, 1968).

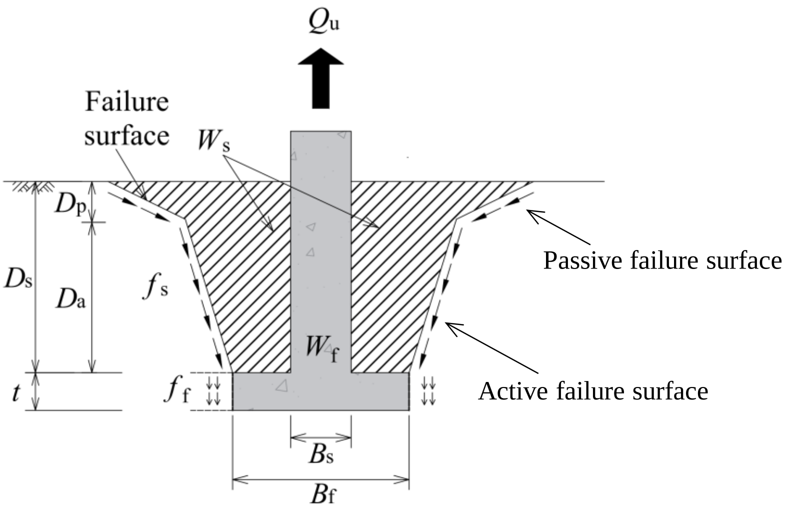

Fig. 6.1 Proposed bilinear Failure mechanism

The gross uplift bearing capacity $Q_u$ consists of the following components: (1) side resistance of the foundation slab $f_f$, (2) shear resistance along the failure surface $f_s$, (3) soil weight within the failure surface $W_s$, and (4) foundation weight $W_f$.

$$Q_u = W_f + W_s + f_s + f_f \tag{6.1}$$

Where, $W_f$ : Weight of the foundation

$W_s$ : Weight of soil above slab of foundation and wedge failure surface

$f_s$ : Shear resistance on wedge failure surface

$f_f$ : Side resistance between the soil and foundation

The net uplift bearing capacity $Q_{net}$ was obtained by subtracting the foundation weight from the gross uplift bearing capacity $Q_u$

$$Q_{net} = Q_u - W_f \tag{6.2}$$

## 6.2 Side shear resistance of foundation slab, $f_f$

Side shear resistance $f_f$ at the side of the foundation slab should be considered because the slab thickness relative to the foundation width is substantial. The resistance $f_f$ was calculated using the product of the unit shear resistance $\tau_s$ and the side area of the slab $A_s$. Side shear resistance $f_f$ is assumed to be constant since it is not affected by failure surface. Mohr–Coulomb failure criterion was applied to determine the unit resistance $\tau_s$, which is proportional to the horizontal stress at the midpoint of the slab and the soil–foundation interface angle $\delta$. The lateral earth pressure acting on the side of the slab was calculated by applying at-rest earth pressure. The shear resistance is calculated by the following procedure.

The at-rest earth pressure can be expressed as $K_0 = 1 - \sin\phi$ (Jaky, 1944). $f_\mathrm{f}$ is given as follows:

$$f_\mathrm{f} = \tau_\mathrm{s} A_\mathrm{s} = 2tB_\mathrm{f}\gamma(D_\mathrm{f} + D_\mathrm{s})K_0 \tan\delta \tag{6.3}$$

where $\gamma$=soil unit weight and $\delta$=soil–foundation interface angle.

The shear stress on the foundation slab $\tau_s$ is

$$\tau_s = \sigma_h \tan\phi \tag{6.4}$$

Where, $\sigma_h$=the average of the lateral earth pressure

$$\sigma_h = \gamma \frac{D_f + D_s}{2} K_0 \tag{6.5}$$

$A_s$ is the area of the foundation slab and given as follows:

$$A_s = 4tB_f \tag{6.6}$$

## 6.3 Soil weight of failure zone, $W_\mathrm{s}$

The amount of soil weight $W_\mathrm{s}$ within the failure surface above the foundation slab was considered a substantial portion of the net capacity $Q_\mathrm{net}$. The soil weight $W_\mathrm{s}$ is equal to the product of the soil unit weight and the soil volume bounded by the failure surface in three dimensions (Fig. 6.1). $W_\mathrm{s}$ can be calculated as follows:

$$W_\mathrm{s} = \gamma\left(V_\mathrm{a} + V_\mathrm{p} - V_\mathrm{s}\right) \tag{6.7}$$

where $V_\mathrm{a}$=volume of the active zone, $V_\mathrm{p}$=volume of the passive zone, and $V_\mathrm{s}$=volume occupied by the foundation shaft.

These volumes were calculated by applying the trapezoidal rule as follows:

$$V_\mathrm{a} = B_\mathrm{a}^2 D_\mathrm{a} - \frac{2B_\mathrm{a}D_\mathrm{a}^2}{\tan\theta_\mathrm{a}} + \frac{4D_\mathrm{a}^3}{3\tan^2\theta_\mathrm{a}}, \tag{6.8}$$

$$V_\mathrm{p} = B_\mathrm{p}^2 D_\mathrm{p} - \frac{2B_\mathrm{p}D_\mathrm{p}^2}{\tan\theta_\mathrm{p}} + \frac{4D_\mathrm{p}^3}{3\tan^2\theta_\mathrm{p}}, \tag{6.9}$$

$$V_\mathrm{s} = \frac{\pi}{4} B_\mathrm{s}^2 D_\mathrm{s} \tag{6.10}$$

where $D_\mathrm{a} = y_T = \tan(45° - \theta_\mathrm{a})\, x_\mathrm{T}$, $B_\mathrm{a} = B_\mathrm{f} + 2x_\mathrm{T}$, $D_\mathrm{p} = D_\mathrm{s} - D_\mathrm{a}$, and $B_\mathrm{p} = B_\mathrm{a} + 2D_\mathrm{p}/\tan\theta_p$. Parameters $D_\mathrm{a}$ and $D_\mathrm{p}$ are heights of the soil mass bounded by active and passive failure surfaces, respectively.

The trapezoidal volume of failure zone can be expressed by following equations from the numerical method of integration.

$$\begin{aligned} \mathrm{V} &= \int \left(\mathrm{B} - \frac{2\mathrm{z}}{\tan\theta}\right)^2 dz \\ &= \int \left(\mathrm{B}^2 - \frac{4\mathrm{Bz}}{\tan\theta} + \frac{4\mathrm{z}^2}{\tan^2\theta}\right) dz \\ &= \mathrm{B}^2\mathrm{z} - \frac{2\mathrm{Bz}^2}{\tan\theta} + \frac{4\mathrm{z}^3}{3\tan^2\theta} \end{aligned} \tag{6.11}$$

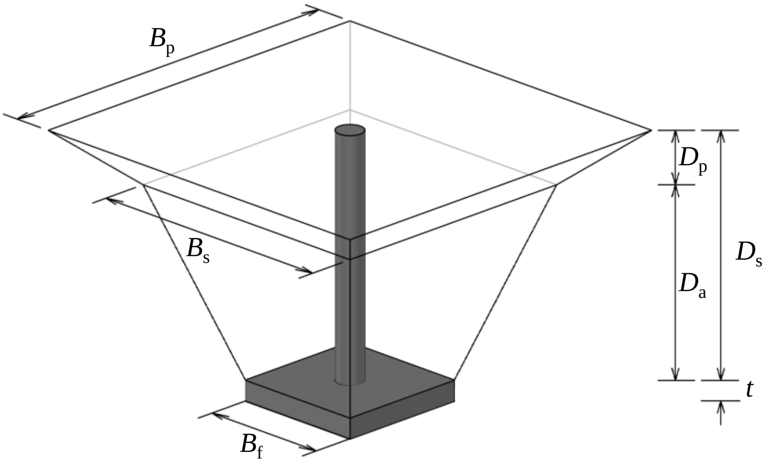

Fig. 6.2 Soil mass bounded by the suggested bilinear failure surface in three dimensions.

## 6.4 Shear resistance on failure surface

This study adopted the limit equilibrium method and Coulomb's theory to determine the shear resistance along the suggested bilinear failure surface $f_s$, which is a key important factor in the calculation of the net uplift bearing capacity. As suggested the shape of the failure surface, it is assumed that the shear strength is mobilized along the failure surface. The shear strength of the ground along the failure surface was assumed to be fully mobilized at the ultimate state. The direction of the resistance $f_s$ was likely to change along the failure surface, as shown in Fig. 6.3.

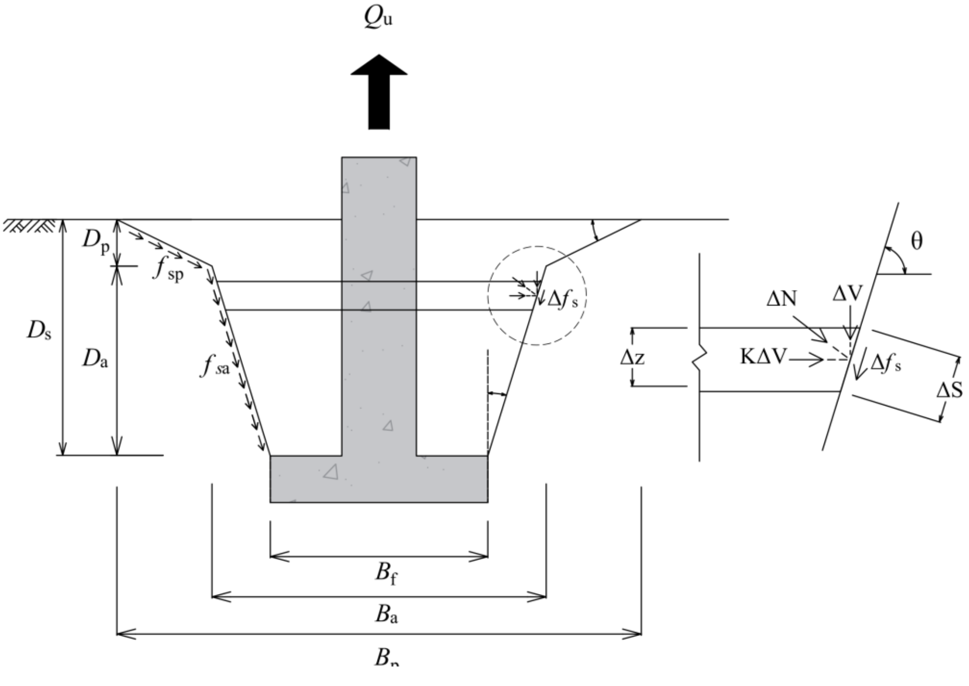

Fig. 6.3 Forces acting on the failure surface of a typical slice of the soil mass.

Matsuo (1967) stated that the earth pressure acting on the active failure surface was in a semi-active state. The infilling process may induce the loosening behavior of the ground near the foundation slab. This study applied semi-active earth pressure $K_{\text{semi-a}}$ an arithmetic average between at-rest and active earth pressure coefficients to the suggested active failure surface to account for these phenomena, and the at-rest earth pressure can be expressed as $K_0 = 1 - \sin\phi$ (Jaky 1944). Rankine's theory was adopted to calculate the active earth pressure as follows: $K_{\text{a}} = \tan^2(45° - \phi/2)$. The selection of the earth pressure coefficient of the active failure surface is examined in the later section.

The coefficient of the earth pressure acting on the passive failure surface was calculated according to Rankine's theory as $K_{\text{p}} = \tan^2(45° + \phi/2)$. The shear resistance of the passive zone can be calculated by following procedure.

The only vertical component of $f_s$ contributed to the resistance against the vertical uplift loading because the horizontal component canceled out according to the assumption of a symmetrical failure surface. The vertical component of $f_s$ can be determined as follows.

$$f_{\text{sv}} = f_{\text{sa}} \sin(90° - \theta_{\text{a}}) + f_{\text{sp}} \sin\theta_{\text{p}} \tag{6.12}$$

where $f_{sv}$=vertical component of $f_s$, $f_{sa}$= $f_{sv}$ along the active failure surface, and $f_{sp}$= $f_{sv}$ along the passive failure surface.

A slice procedure was adopted to compute the vertical component $f_{\mathrm{ccv}}$ at a considered failure surface (Fig. 6.1), which can be expressible as follows.

$$f_{\mathrm{cc}} = \int p_{\mathrm{cc}}\,\mathrm{d}f_{\mathrm{cc}} \tag{6.13}$$

where $p_{\mathrm{cc}}$=perimeter of the soil mass bounded by the considered failure surface and $\mathrm{d}f_{\mathrm{cc}}$=$f_{\mathrm{sv}}$ of a certain slice of the soil mass bounded by the considered failure surface.

Considering a slice with a thickness of $\Delta z$ (Fig. 6.3), the value of $\mathrm{d}T_{\mathrm{ccv}}$ was calculated as a product of the unit shear resistance $\Delta f_{\mathrm{s}}$ and the perimeter $\Delta S$. The resistance $\Delta T$ was determined by obeying Coulomb's theory as follows.

$$\Delta f_{\mathrm{s}} = \Delta N \tan\phi \tag{6.14}$$

where $\Delta N$ is the resultant stress acting at the failure surface of the considered slice as expressed as follows.

$$\Delta N = \Delta V \cos\theta + \Delta H \cos\theta \tag{6.15}$$

where $\theta$=inclination of the failure surface of the slice and $\Delta V$, $\Delta H$ =vertical and horizontal stresses acting at the failure surface of the considered slice, respectively. These forces can be calculated using the weight of the slice and the earth pressure coefficient $K$. The final expression of $\Delta N$ can be found as follows.

$$\Delta \mathrm{s} = \frac{\Delta z}{\sin\theta} \tag{6.16}$$

$$\Delta \mathrm{N} = \left(\gamma\left(z+\frac{\Delta \mathrm{z}}{2}\right)\cos\theta + K\gamma\left(z+\frac{\Delta \mathrm{z}}{2}\right)\sin\theta\right)\frac{\Delta z}{\sin\theta}$$

$$= \gamma\left(\frac{1}{\tan\theta}+K\right)\left(z+\frac{\Delta \mathrm{z}}{2}\right)\Delta z \qquad (6.17)$$

$$\Delta f_{\mathrm{s}} = \Delta \mathrm{N}\tan\phi = \gamma\tan\phi\left(\frac{1}{\tan\theta}+K\right)\left(z+\frac{\Delta \mathrm{z}}{2}\right)\Delta z \qquad (6.18)$$

In limit state on simplification

$$\mathrm{d}f_{\mathrm{s}} = \gamma\tan\phi\left(\frac{1}{\tan\theta}+K\right)z\,dz \qquad (6.19)$$

$$\mathrm{d}f_{\mathrm{cc}} = df_s dS = \gamma\tan\phi\left(\frac{1}{\tan\theta}+K\right)zdz \qquad (6.20)$$

The perimeter $p_{\mathrm{cc}}$ of the soil mass bounded by the active and passive failure surface is respectively given as follows.

For the calculation of perimeter acting on the failure surface,

$$P_{cc} = 4(B-\frac{2}{\tan\theta}z)$$

where *P*= perimeter of the considered component; *B*= large width of the considered component; and *z*=height of the considered component relative to the origin.

$$P_{cc-a} = 4\left(B_a - \frac{2}{\tan(90° - \theta_a)}z\right) \qquad (6.21)$$

$$P_{cc-p} = 4\left(B_p - \frac{2}{\tan\theta_p}z\right) \qquad (6.22)$$

Substituting Eqs. (6.20)–(6.22) into Eq. (6.13), it can be obtained as follows.

$$\mathrm{d}f_{\mathrm{sa}} = 4\gamma \tan\phi \left(\frac{1}{\tan(90°-\theta_a)} + K\right)\left(B_{\mathrm{a}} - \frac{2}{\tan(\ 90°-\theta_a)} D_{\mathrm{a}}\right) z dz \qquad (6.23))$$

$$\mathrm{d}f_{\mathrm{sp}} = 4\gamma \tan\phi \left(\frac{1}{\tan\theta_p} + K\right)\left(B_{\mathrm{p}} - \frac{2}{\tan\theta_p} D_{\mathrm{p}}\ \right) z dz \qquad (6.24)$$

After the integration and contraction, the vertical components $f_{\mathrm{sa}}$ and $f_{\mathrm{sp}}$ along the active and passive failure surface can be respectively presented as follows.

$$\begin{aligned} f_{\mathrm{sa}} &= 2\gamma \tan\phi \left(\frac{1}{\tan(90°-\theta_a)} + K_{semi-a}\right) \\ &\times \left(B_a D_a^2 - \frac{4}{3\tan(90°-\theta_a)} D_a^3\right) \end{aligned} \qquad (6.25)$$

$$f_{\mathrm{sp}} = 2\gamma \tan\phi \left(\frac{1}{\tan\theta_p} + K_p\right) \times \left(B_p D_p^2 - \frac{4}{3\tan\theta_p} D_p^3\right) \qquad (6.26)$$

## 6.5 Verification and comparison

### 6.5.1 Verification with experimental data

The semi-analytical solution proposed in proceeding sections was used to estimate the net uplift bearing capacity $Q_{net}$ obtained from centrifuge tests of this study. Fig. 6.4 illustrates that the proposed solution can obtain an acceptable estimation of $Q_{net}$ for spread foundations with a slab width of 3.0–6.5. Fig. 6.4 shows consistency between the measured net capacity $Q_{net}$ and those calculated by the proposed semi-analytical solution after updating the angle $\theta_a$.

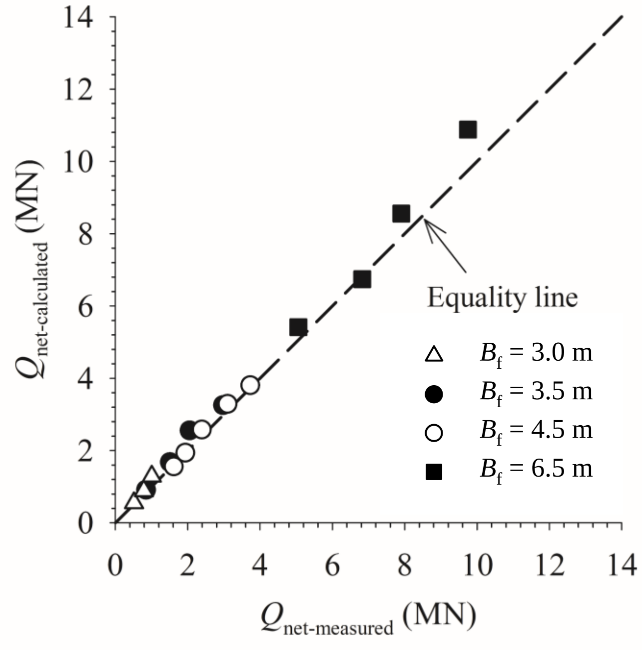

Fig. 6.4 Calculation of $Q_{net}$ with $\theta_a$ determined by genetic analysis (a) in comparison with measured data and (b) Spearman correlation test on the model factor ($M=Q_{net\text{-}measured}/Q_{net\text{-}calculated}$) against embedment depth $D_s$.

The proposed semi-analytical solution was used to predict the net capacity $Q_{\mathrm{net}}$ of experiments reported in the literature for further verification. Small- and full-scale uplift tests on horizontal anchors, which may appear similar to the spread foundation problem, were conducted by Dickin (1988) and Tagaya et al. (1988) with consideration for varying widths from 0.5 m to 4.0 m and embedment depth ratios. Data of 1 g uplift experiments on anchor plates by Das and Jones (1982) and Ilamparuthi et al. (2002) were also adopted although their anchor widths were smaller than 0.35 m. Fig. 6.5 depicts that the proposed solution can reasonably estimate $Q_{\mathrm{net}}$ values compared with existing data under various conditions, including different foundation widths, embedment depths, and test scales. Note that an equivalent rectangular foundation for all data was considered in the comparison presented in Fig. 6.5.

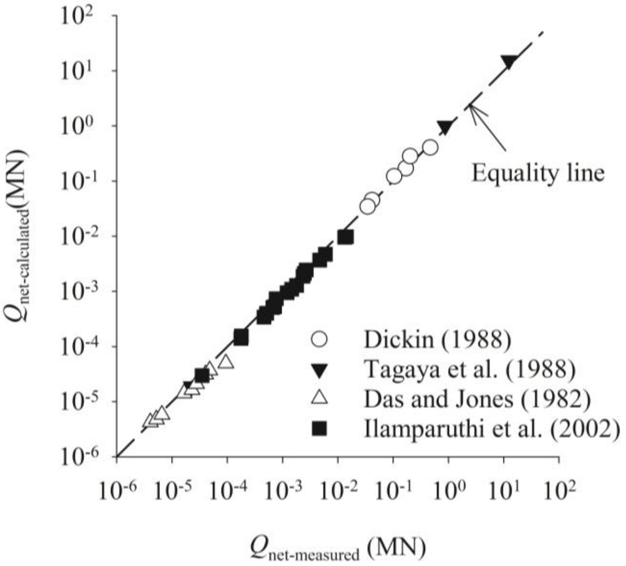

Fig. 6.5 Comparison of $Q_{\mathrm{net}}$ between previously published data and calculation by proposed semi-analytical solution.

### 6.5.2 Comparison with existing analytical solutions

Comparison of the net capacity $Q_{net}$ between the measurement and estimation is presented in Fig. 6.6 while considering various conditions of foundation dimensions and soil densities. Although the scale effect on the estimate of the large net capacity $Q_{net}$ has been ignored in the literature, the proposed semi-analytical solution can reasonably minimize it.

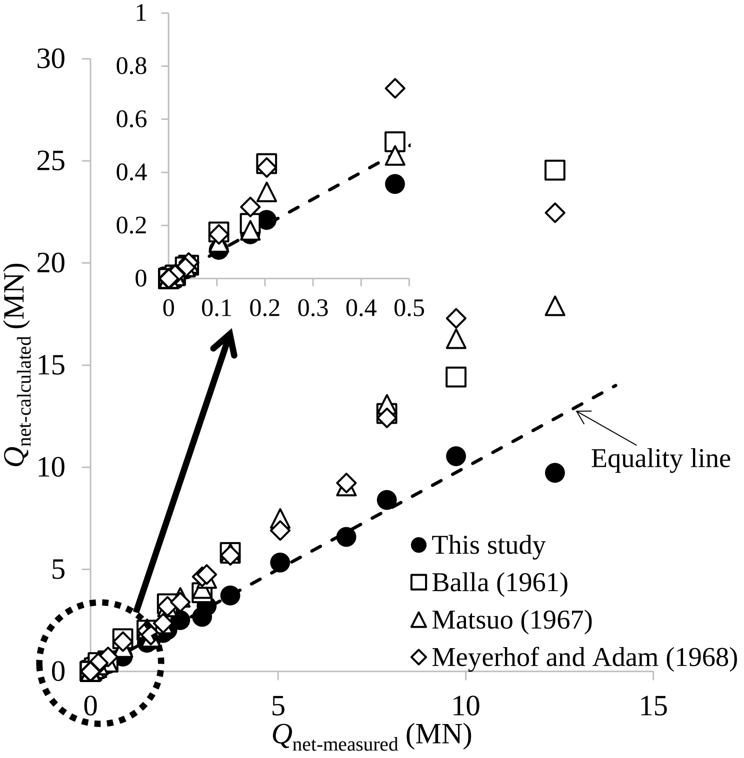

Fig. 6.6 Comparisons with theoretical results proposed by other researchers

### 6.5.3 Variation of uplift resistance factor

The net uplift bearing capacity $Q_{\mathrm{net}}$ is commonly converted to a factor called the uplift resistance factor in design practice. The uplift resistance factor can be expressed as follows:

$$N_{\mathrm{q}} = \frac{Q_{\mathrm{net}}}{\gamma B_{\mathrm{f}}^{2} D_{\mathrm{s}}} \tag{6.27}$$

Fig. 6.7 shows the variation of $N_{\mathrm{q}}$ with respect to the possible dimensions of a spread foundation and soil densities. The slab width varied from 1 m to 6 m, and the embedment depth ratio was set from 0.5 to 3.0. Das and Jones (1982) applied sandy soil in different states to investigate the behavior of $N_{\mathrm{q}}$. Loose, medium-dense, and dense sands presented unit weights of 14.8, 15.8, and 16.9 kN/m$^3$ and internal friction angles of 31°, 34°, and 40.5°, respectively. The factor $N_{\mathrm{q}}$ linearly increased with the embedment depth ratio $D_{\mathrm{s}}/B_{\mathrm{f}}$ given a constant value of $B_{\mathrm{f}}$ (Fig. 6.7a). The calculated factor $N_{\mathrm{q}}$ was relatively less than the findings of (Ovesen, 1981)and Dickin (1988) because their foundation size is considerably smaller than the one considered in this study. Meanwhile, values of $N_{\mathrm{q}}$ exponentially decreased with the large value of $B_{\mathrm{f}}$ at a certain embedment depth ratio and soil state according to the scale effect in Fig. 6.7b (Dickin, 1988; Ovesen, 1981; Tagaya et al., 1988).

The calculated factor $N_{\mathrm{q}}$ in Fig. 6.7 can be used as a reference for the preliminary design of a typical spread foundation embedded in cohesionless soil. The net capacity $Q_{net}$ of the design foundation trial can be conveniently determined using Eq. (6.27).

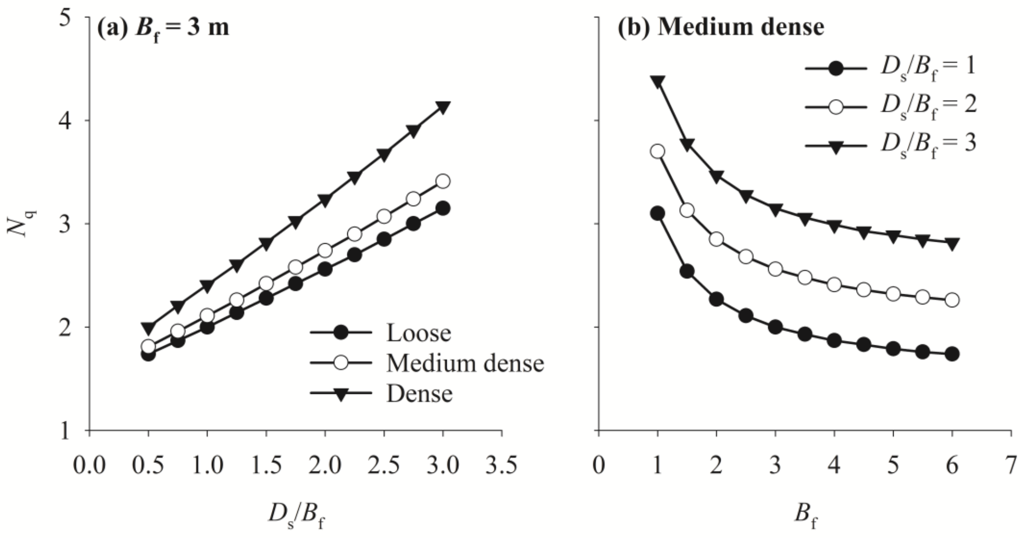

Fig. 6.7 Variation of uplift resistance factor $N_q$ with respect to foundation width $B_f$, embedment depth ratio $D_s/B_f$, and soil states.

## 6.6 Summary

A semi-analytical solution for the net uplift bearing capacity corresponding to the bilinear failure surface was proposed by adopting the limit equilibrium approach associated with the slice procedure. The comparison of current test results and previously published data verified the applicability of the proposed solution in the determination of net capacity. The proposed solution appeared more appropriate than existing analytical solutions in estimating the net capacity with consideration for the scale effect on the uplift behavior of a large spread foundation. The main conclusions can be summarized as follows.

(1) A semi-analytical solution for the net uplift bearing capacity corresponding to the bilinear failure surface was proposed by adopting the limit equilibrium approach associated with the slice procedure and verified with centrifuge and 1g laboratory test results.

(2) The semi-active earth pressure coefficient should be applied in the calculation of the shear resistance considering the uplift movement of the free ground above the failure surface.

(3) Active failure surface that is formed near the foundation slab due to the uplift loading varies with soil density and the geometry of foundation. The function of $\theta_a$ was proposed to determine the shear resistance and soil weight, which are important components of the uplift bearing capacity.

# Chapter 7. Conclusion and Recommendations

## 7.1 Conclusions

Uplift behavior and failure mechanisms of the shallow spread foundation in sand were extensively acquired through a centrifuge test program. The uplift behavior was confirmed through analysis of uplift bearing capacity according to various foundation geometry and ground conditions and vertical uplift displacement shown on the ground surface. The scale effect was extensively explored by adopting the previously reported data mostly under 1g model test condition. The half-cut model experiment was performed to analyze the failure surface subsurface soil, and the failure surface was characterized through image analysis. Major conclusions of the research work presented in this dissertation can be summarized as follows.

### *Uplift behavior*

- The uplift load–displacement curve obtained from centrifuge tests by means of a displacement controlling method showed hardening behavior within a relatively small displacement and softening behavior after attaining a peak. The uplift bearing capacity $Q_u$ determined a peak point increased with larger slab width, deeper embedment depth, and denser sandy soil. The existing methods were not successful in estimating the net uplift bearing capacity $Q_{net}$ of the spread foundations tested in this study due to the scale effect.

- The uplift resistance factor Nq of the spread foundation were observed to become smaller with large slab width at a certain embedment depth ratio compared with the 1g model test results by reasonably simulating the in-situ stress conditions. Dimensionless uplift displacement $w_p/B_f$ decreased with the increase in the relative shaft diameter $B_s/B_f$. These phenomena were more pronounced at large embedment depth ratios.
- Empirical formulations of $N_q$ and $w_p$ were proposed by adopting genetic programming for symbolic regression. The scale effect was covered in these empirical equations by analyzing the governing variables independently, such as the slab width, embedment depth, shaft width, and soil friction angle. The proposed equations were capable of estimating the values of $N_q$ and $w_p$ under various conditions reported in the literature and thereby verifying their high applicability in the preliminary design consideration of spread foundations.
- A simplified empirical influence zone was proposed on the basis of the measurement of the ground surface displacement. The proposed influence zone was a straight line connecting the top outermost of the slab to the point at the ground surface with negligible heaving. Generally, the empirical influence zone made an angle of approximately 0.9 $\phi$ (where $\phi$ is the soil friction angle) relative to the vertical line. It was proved that the proposed influence zone could be considered a significant reference for predicting the failure surface of the spreading foundation under uplift loading.

### *Failure mechanisms*

- The failure surface curves near the foundation slab and near the ground surface were almost linear lines which have different inclination. The higher the density of the ground and the deeper the penetration depth of the foundation, the greater the angle formed with the vertical line. The failure surface near the surface of the ground was similar to the inclination of the angle in the passive failure mode.
- The suggested bilinear failure surface based on the measured uplift displacement of the ground surface was capable of capturing different failure mechanisms along the depth of the spread foundation, including a passive mode near the ground surface and an active mode downward. Therefore, the failure surface was expressed in a bilinear form. Determination of parameters to characterize the bilinear failure surface was enhanced when a genetic programming method based on a symbolic regression technique was adopted.

### *Semi-analytical solutions*

- A semi-analytical solution for the net uplift bearing capacity corresponding to the bilinear failure surface was proposed by adopting the limit equilibrium approach associated with the slice procedure and verified with centrifuge and 1g laboratory test results.

- The semi-active earth pressure coefficient should be applied in the calculation of the shear resistance considering the uplift movement of the ground above the failure surface.
- Active failure surface that is formed near the foundation slab due to the uplift loading varies with soil density and the geometry of foundation. The function of $\theta_a$ was proposed to determine the shear resistance and soil weight, which are important components of the uplift bearing capacity.

## 7.2 Recommendations for the further studies

Experimental studies presented in this dissertation have contributed to the understanding of the uplift behavior of the shallow spread foundation in the dry cohesionless soil. Bilinear failure mechanisms were analyzed using PIV methods and machine learning technique Semi-analytical solution was proposed by performing a series of centrifuge model tests. Further researches on this subject can be conducted on the potential topic as follows.

- Another experimental study is conducting additional experiment in unsaturated or saturated soil which is similar field condition. The effect of the pore water on the uplift behavior of the shallow spread foundations is needed to consider since suction force attributes to the uplift behavior.
- Even though uplift force is the main design load to the foundations, the shallow spread foundations of the transmission tower were under the combined load caused by line breakage or wind load. It needs to check of applicability of estimated uplift bearing capacity to the transmission tower foundation system under combined loading.
- Finally, the semi-analytical solution is developed from reduced-scale model tests in centrifuge. Centrifuge test results and semi-analytical

solution should be verified with field tests results prior to the application of the practical design.

# List of References

Baker, W. H., & Konder, R. L. (1966). Pullout load capacity of a circular earth anchor buried in sand. *Highway Research Record*, *108*.

Balla. (1961). The resistance to breaking-out of mushroom foundations for pylons. *Proc. 5th. Int. Conf. Soil Mech. Found. Eng.*, 569–576.

Chattopadhyay, B. C., & Pise, P. J. (1986). Uplift capacity of piles in sand. *Journal of Geotechnical Engineering*, ***112*** No.9, 888–904. https://doi.org/10.1061/(ASCE)0733-9410(1986)112:9(888)

Cheuk, C. Y., White, D. J., & Bolton, M. D. (2008). Uplift Mechanisms of Pipes Buried in Sand. *Journal of Geotechnical and Geoenvironmental Engineering*, ***134*** No.2, 154–163. https://doi.org/10.1061/(asce)1090-0241(2008)134:2(154)

Das, B. M., & Jones, A. D. (1982). Uplift Capacity of Rectangular Foundations in Sand. *Transportation Research Record*, 54–58.

Das, B. M., & Shukla, S. K. (2013). *Earth anchors*. J. Ross Publishing.

Deshmukh, V. B., Dewaikar, D. M., & Choudhury, D. (2010). Analysis of rectangular and square anchors in cohesionless soil. *International Journal of Geotechnical Engineering*, ***4*** No.1, 79–87. https://doi.org/10.3328/IJGE.2010.04.01.79-87

Dickin, E. A. (1988). Uplift behavior of horizontal anchor plates in sand. *Journal* *of Geotechnical Engineering*, ***114*** No.11, 1300–1317.

Dickin, E. A., & Leung, C. F. (1992). The influence of foundation geometry on the uplift behaviour of piles with enlarged bases. *Canadian Geotechnical Journal*, ***29*** No.3, 498–505. https://doi.org/10.1139/t92-054

Ding, S., Cheng, Y., Zheng, H., Xue, F., Nie, Z., & Man, Y. (2021). Uplift Bearing Capacity of Transmission Tower Foundation in Reinforced Aeolian Sand Using Simplified Model Tests. *Advances in Civil Engineering*, ***2021***. https://doi.org/10.1155/2021/6630731

Huang, B., Liu, J., Ling, D., & Zhou, Y. (2015). Application of particle image velocimetry (PIV) in the study of uplift mechanisms of pipe buried in Loose sand. *Journal of Civil Structural Health Monitoring*, ***5*** No.5, 599–614. https://doi.org/10.1007/s13349-015-0130-y

IEEE. (2001). IEEE Guide for Transmission Structure Foundation Design and Testing. *IEEE Std 691-2001*, 1-194 (in Korean). https://doi.org/10.1109/IEEESTD.2001.93372

Ilamparuthi, K., Dickin, E. A., & Muthukrisnaiah, K. (2002). Experimental investigation of the uplift behaviour of circular plate anchors embedded in sand. *Canadian Geotechnical Journal*, ***39*** No.3, 648–664. https://doi.org/10.1139/t02-005

Jaky, J. (1944). No TitleThe coefficient of earth pressure at rest. *J. of the Society of Hungarian Architects and Engineers*, 355–358.

Janbu, N. (1963). Soil compressibility as determined by odometer and triaxial tests.

*Proc. Europ. Conf. SMFE,* ***1***, 19–25.

Kananyan, A. S. (1966). Experimental investigation of the stability of bases of anchor foundations. *Soil Mechanics and Foundation Engineering,* ***3*** No.6, 387–392.

Kang, J. G., Yasufuku, N., Ishikura, R., & Purnama, A. Y. (2019). Prediction of Uplift Capacity of Belled-type Pile with Shallow Foundation in Sandy Ground. *Lowland Technology International,* ***21*** No.2, 71–79.

Korea Electronic Power Corporation (KEPCO). (2013). Design Standard for Transmission Tower Foundation. In *DS-1110*.

Kulhawy, F. H., Trautmann, C. H., Beech, J. F., O'Rourke, T. D., McGuire, W., Wood, W. A., & Capano, C. (n.d.). *1983, Transmission Line Structure Foundations for Uplift-Compression Loading, report EL-2870. Electric power research institute, Palo Alto, California, p. 412*.

Kulhawy, F. H., Trautmann, C. H., & Nicolaides, C. N. (1987). Spread foundations in uplift: experimental study. *Foundations for Transmission Line Towers*, 96–109.

Lin, J. G., Hsu, S. Y., & Lin, S. S. (2015). The new method to evaluate the uplift capacity of belled piles in sandy soil. *Journal of Marine Science and Technology (Taiwan),* ***23*** No.4, 523–533. https://doi.org/10.6119/JMST-015-0511-2

Liu, J., Liu, M., & Zhu, Z. (2012). Sand Deformation around an Uplift Plate Anchor. *Journal of Geotechnical and Geoenvironmental Engineering*, ***138***

No.6, 728–737. https://doi.org/10.1061/(asce)gt.1943-5606.0000633

Matsuo, M. (1967). Study on the uplift resistance of footing (I). *Soils and Foundations*, ***7*** No.4, 1–37.

Matsuo, M. (1968). Study on the uplift resistance of footing (II). *Soils and Foundations*, ***8*** No.1, 18–48.

Meyerhof, G. G., & Adams, J. I. (1968). The ultimate uplift capacity of foundations. *Canadian Geotechnical Journal*, ***5*** No.4, 225–244.

Murray, E. J., & Geddes, J. D. (1987). Uplift of anchor plates in sand. *Journal of Geotechnical Engineering*, ***114*** No.12, 1461–1462. https://doi.org/10.1061/(ASCE)0733-9410(1988)114:12(1461)

Murray, E. J., & Geddes, J. D. (1988). Uplift of anchor plates in sand. *Journal of Geotechnical Engineering*, ***114*** No.12, 1461–1462. https://doi.org/10.1061/(ASCE)0733-9410(1988)114:12(1461)

Ovesen, N. K. (1981). Centrifuge tests of uplift capacity of anchors. *Proc. 10th. Int. Conf. on SMEE*, 717–722.

Pacheco, M. P., Danziger, F. A. B., & Pinto, C. P. (2008). Design of shallow foundations under tensile loading for transmission line towers: An overview. *Engineering Geology*, ***101*** No.3–4, 226–235. https://doi.org/10.1016/j.enggeo.2008.06.002

Rattley, M. J., Richards, D. J., & Lehane, B. M. (2008). Uplift Performance of Transmission Tower Foundations Embedded in Clay. *Journal of Geotechnical and Geoenvironmental Engineering*, ***134*** No.4, 531–540.

https://doi.org/10.1061/(asce)1090-0241(2008)134:4(531)

Roy, A., O’loughlin, C. D., Chow, S. H., & Randolph, M. F. (2021). Inclined loading of horizontal plate anchors in sand. *Geotechnique*, 0–2. https://doi.org/10.1680/jgeot.20.P.119

Roy, K., Hawlader, B., Kenny, S., & Moore, I. (2018). Uplift Failure Mechanisms of Pipes Buried in Dense Sand. *International Journal of Geomechanics*, ***18*** No.8, 04018087. https://doi.org/10.1061/(asce)gm.1943-5622.0001226

Sakai, T., & Tanaka, T. (1998). Scale effect of a shallow circular anchor in dense sand. *Soils and Foundations*, ***38*** No.2, 93–99. https://doi.org/10.3208/sandf.38.2_93

Sakai, T., & Tanaka, T. (2007). Experimental and Numerical Study of Uplift Behavior of Shallow Circular Anchor in Two-Layered Sand. *Journal of Geotechnical and Geoenvironmental Engineering*, ***133*** No.4, 469–477. https://doi.org/10.1061/(asce)1090-0241(2007)133:4(469)

Tagaya, K., Scott, R. F., & Aboshi, H. (1988). Scale effect in anchor pullout test by centrifugal technique. *Soils and Foundations*, ***28*** No.3, 1–12. https://doi.org/10.3208/sandf1972.28.3_1

Trautmann, C. H., & Kulhawy, F. H. (1988). Uplift load-displacement behavior of spread foundations. *Journal of Geotechnical Engineering*, ***114*** No.2, 168–184.

Vermeer, P. A., & Sutjiadi, W. (1985). The uplift resistance of shallow embedded anchors. *11th International Conference on Soil Mechanics and Foundation*

*Engineering*, 1635–1638. https://www.issmge.org/publications/publication/the-uplift-resistance-of-shallow-embedded-anchors

Zhang, X., Liu, J., & Liu, M. (2019). Experimental study on uplift behavior of group anchors in sand. *Geotechnical Testing Journal*, ***42*** No.3, 687–702. https://doi.org/10.1520/GTJ20170430

Zhuang, P.-Z., Yue, H.-Y., Song, X.-G., Yang, H., & Yu, H.-S. (2021). Uplift Behavior of Pipes and Strip Plate Anchors in Sand. *Journal of Geotechnical and Geoenvironmental Engineering*, ***147*** No.11, 04021126. https://doi.org/10.1061/(asce)gt.1943-5606.0002673

# Appendix A: Test results of inclined loading condition

As previously stated, the uplift bearing capacity of transmission tower foundations that receive loading below 10 degrees from vertical can be evaluated through vertical loading. To experimentally verify and determine the loading conditions, preliminary experiments were conducted to set the loading conditions. The load condition was performed according to the test layout in Section 3.4.1 and the load was applied as shown in Figure A1. A total of 4 additional experiments were performed under the conditions of loading inclination 10 degrees, relative density 40, 80%, foundation width 4.5, 6.5 m, and embedment depth ratio 1.3.

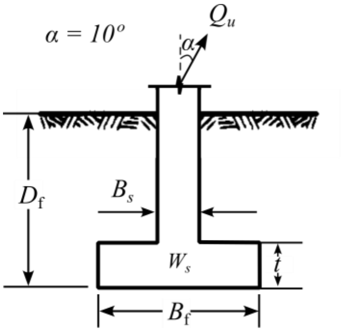

Fig. A1 Schematic diagram of inclined loading tests.

Load-displacement curves for all experimental cases were plotted in Fig. A2, regardless of the slope of the load. The same behavior was observed, with rapid increase of uplift load in initial phase, hardening behavior until the peak, and then softening behavior. However, the peak load and displacement tended to be larger compared to the vertical loading condition, which is likely due to the influence of horizontal load.

The uplift bearing capacity of the shallow spread foundation under the condition of vertical loading and loading inclined 10 degrees from vertical was compared, using the method applied by Roy et al. (2021). The vertical and horizontal components of pile bearing capacity were separated by using simple trigonometry. The vertical component of inclined loading conditions and the uplift bearing capacity of vertical uplift loading conditions were compared and analyzed for the interaction between horizontal loads and uplift bearing capacity in Table A1. The maximum and average error shown in the two loading conditions were 7% and 3.1%, respectively, indicating that the effect of horizontal load on uplift capacity is negligible.

Based on these preliminary experiment results, it was concluded that the uplift bearing capacity of transmission tower foundation under inclined load can be confirmed through vertical load.

**(a)** $B_f$ = 4.5m

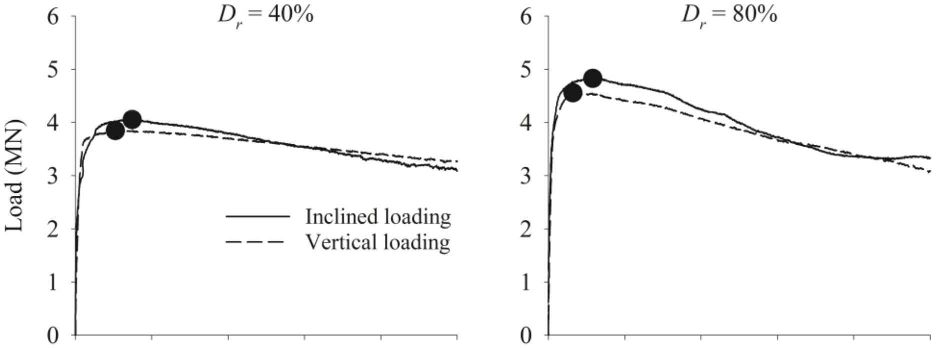

**(b)** $B_f$ = 6.5m

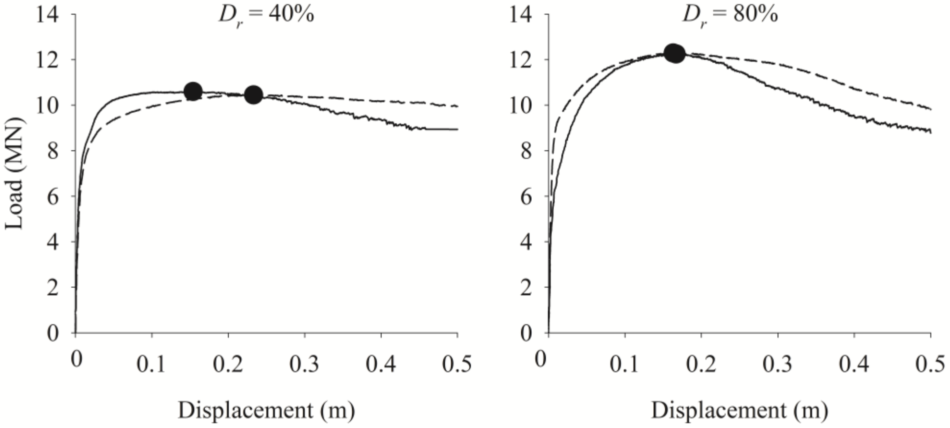

Fig. A2 Load-displacement curves under different loading direction

Table A1 Comparison of uplift bearing capacity with different loading inclination

| $B_f$ (MN) | $D_r$ (%) | $D_f/B_f$ | $Q_u$ (MN) | Comparison of net uplift load (MN) | |
|---|---|---|---|---|---|
| | | | | Inclined loading (vertical component) | Vertical loading |
| 4.5 | 40 | 1.3 | 4.05 | 2.56 | 2.39 |
| | | | | (+7.0%) | |
| 6.5 | 40 | 1.3 | 10.59 | 7.91 | 7.91 |
| | | | | (0.0%) | |
| 4.5 | 80 | 1.3 | 4.82 | 3.21 | 3.1 |
| | | | | (+3.4%) | |
| 6.5 | 80 | 1.3 | 12.24 | 9.53 | 9.75 |
| | | | | (-2.2%) | |

# Appendix B: Test results considering excavation

The basic steps in building a spread foundation for a transmission tower are roughly as follows: digging the foundation, installing the foundation, and backfilling.

It was assumed that the backfill to be looser than the original dense ground after excavation for installing a foundation.

The excavated surface was modeled as an aluminum reversed trapezoidal shaped box, as shown in Fig. B1. The roughness of the excavated surface(over 0.07 of $R_n$) was set to adequately simulate the roughness of the dense ground at the excavated surface. The compaction of the backfill soil was done using the same silica sand as in the section 3.4 of manuscript. The relative density of the compacted soil was set at 40%, and the relative density was prepared by gently tamping the soil every 1 cm of depth.

4 centrifugal experiments were carried out to investigate the influence of excavation slope angle on uplift bearing capacity and soil behavior. Experiments were conducted under the conditions of foundation width 3.0m, embedment depth ratio of 1.3 and 1.6, relative density of 40%, and excavation angles of 1:0.1, 1:0.3, and 1:0.5.

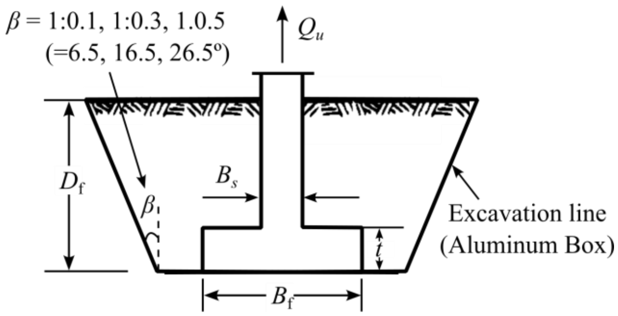

Fig. B1 Schematic diagram of loading tests considering excavation condition.

The load-displacement curves obtained through uplift tests with different excavation angle and embedment depth were shown in Fig. B2. It was found that the uplift bearing capacity increases as the embedment depth increases at the same excavation angle, and that the uplift bearing capacity increases slightly and the peak displacement increases as the excavation angle increases at the same embedment depth.

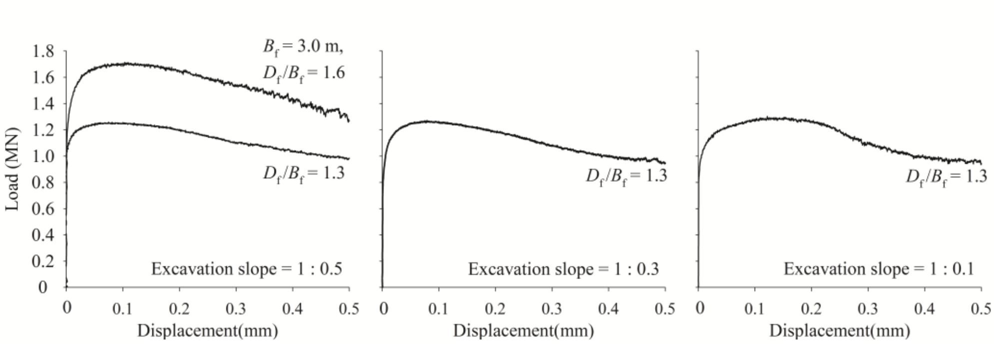

Fig. B2 Load-displacement curves of loading tests considering excavation condition

The excavated surface was compared with the ideal experimental condition of in-situ soil which is backfill soil is representative in-situ soil. As shown in Fig. B3 and Table B1, in relatively shallow embedment ratios with embedment ratio of 1.3, the load-displacement curve showed almost the similar curve for both conditions, indicating that the excavated surface leads to increase the peak load and displacement and had a slight effect on the experimental results. However, in the case of a relatively large embedment ratio of 1.6, the uplift bearing capacity difference increased by about 20% compared to the excavated surface simulation, and it was confirmed that the excavated surface has a definite effect on the support strength and soil behavior. This is because the failure surface is formed inside the backfilled soil as the foundation is uplifted, causing horizontal displacement, and it is judged that the excavated surface restrains the displacement, causing the difference to be shown.

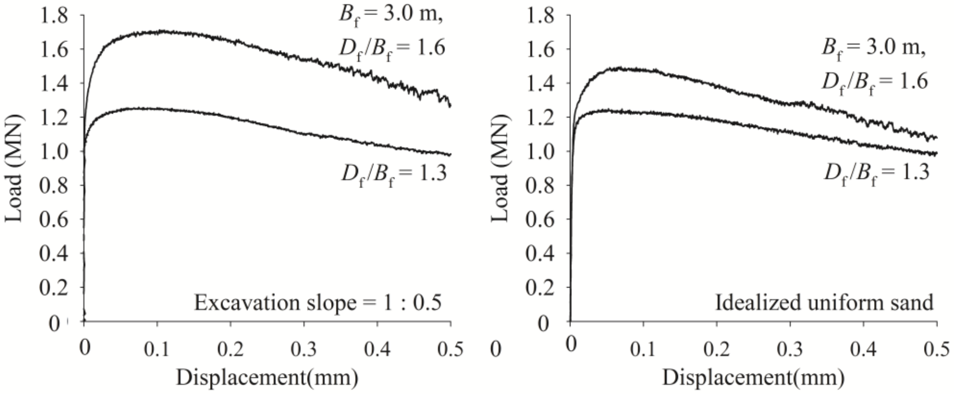

Fig. B3 Comparison of test results with different excavation condition in $D_r$ = 40%

Table B1 Comparison of uplift bearing capacity with simulation of excavated condition

| $B_f$ (m) | $D_f/B_f$ | Excavation slope | $Q_u$ (MN) | Comparison of net uplift load (MN) | |
|---|---|---|---|---|---|
| | | | | Excavated condition | Idealized in-situ condition |
| 3.0 | 1.3 | 1:0.1 (6.5°) | 1.30 | 0.839 | 0.786 |
| | | | | (+6.7%) | |
| 3.0 | 1.3 | 1:0.3 (16.5°) | 1.27 | 0.803 | 0.786 |
| | | | | (+2.2%) | |
| 3.0 | 1.3 | 1:0.5 (26.5°) | 1.26 | 0.795 | 0.786 |
| | | | | (+1.1%) | |
| 3.0 | 1.6 | 1:0.5 (26.5°) | 1.713 | 1.227 | 1.001 |
| | | | | (+21.9%) | |

# Appendix C: Test results of sloping ground

As mentioned in Section 1.1, transmission towers are built on mountainous areas, and often on sloped terrain. Centrifugal experiments were performed to investigate the effect of slope angle on the uplift bearing capacity of foundations. The experiments were conducted on a slope angle of 20 degrees with foundation widths of 3.5, 4.5, and 6.5m, embedment depth ratios of 1.0, 1.3, and 1.6, and relative densities of 40 and 80%. A total of 6 experiments were performed under sloping ground conditions. The load-displacement curves obtained from the experiments were plotted in Fig. B2.

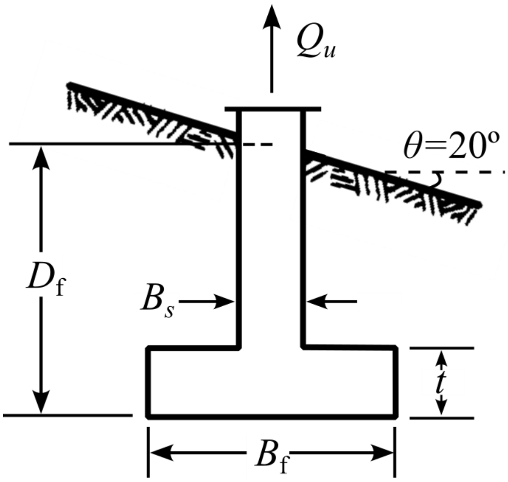

Fig. C1 Schematic diagram of tests on sloping ground.

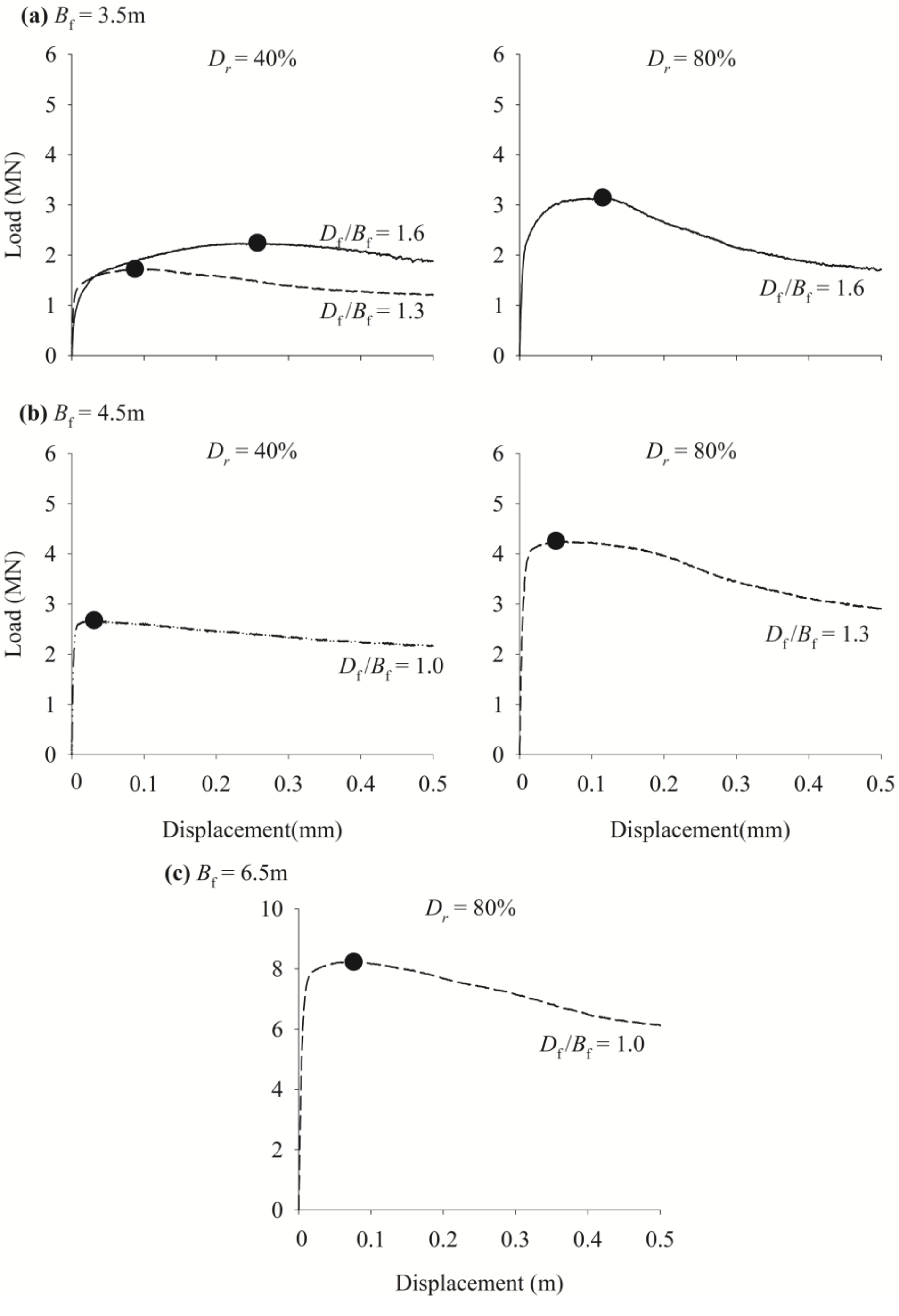

Fig. C2 Load-displacement curves of sloping ground.

The results of the horizontal and sloping ground (20 degree) centrifugal experiments were analyzed by comparing the results of the horizontal ground experiment corresponding to the sloping ground experimental conditions in FigC3 and Table C1. The load-displacement curves of the horizontal and inclined ground conditions generally showed similar curves. However, it was clearly confirmed that the uplift bearing capacity decreased in the sloping ground compared to the horizontal ground. When compared with the result of the horizontal ground centrifugal experiments, the uplift bearing capacity decreased by an average of 13.6%, ranging from 7.3% to 18.8%. This can be used as reference data when designing foundation in sloping ground condition.

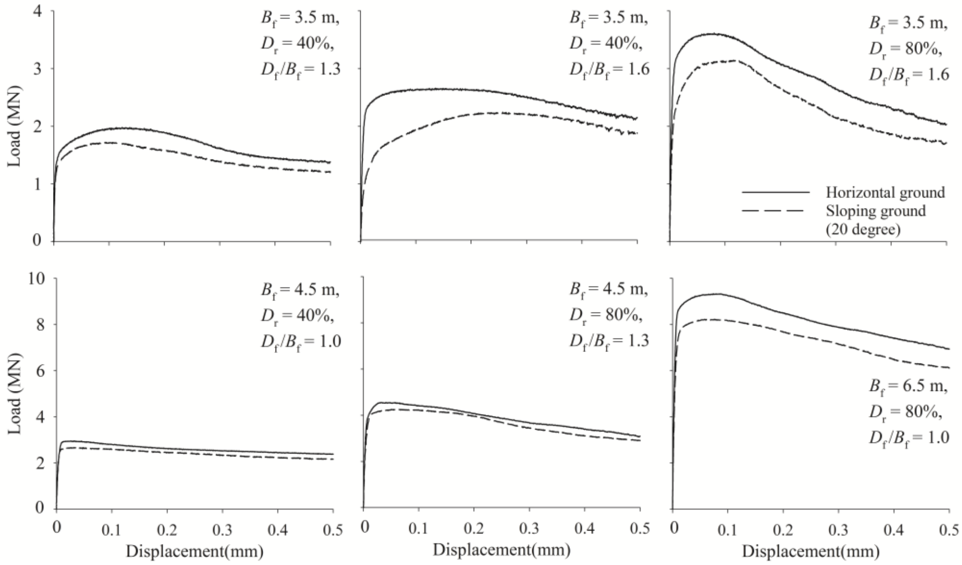

Fig. C3 Comparison of load-displacement curves with sloping and horizontal ground.

*Table C1* Comparison of uplift bearing capacity with different ground slope

| $B_f$ (MN) | $D_r$ (%) | $D_f/B_f$ | $Q_u$ (MN) | Comparison of net uplift load (MN) | |
|---|---|---|---|---|---|
| | | | | Inclined loading (vertical component) | Vertical loading |
| 3.5 | 40 | 1.3 | 1.72 | 1.22<br>(-18.8%) | 1.51 |
| 3.5 | 40 | 1.6 | 2.24 | 1.72<br>(-16.4%) | 2.05 |
| 4.5 | 40 | 1.0 | 2.67 | 1.40<br>(-13.2%) | 1.61 |
| 3.5 | 80 | 1.6 | 3.14 | 2.60<br>(-12.8%) | 2.98 |
| 4.5 | 80 | 1.3 | 4.26 | 2.88<br>(-7.3%) | 3.10 |
| 6.5 | 80 | 1.0 | 8.23 | 5.91<br>(-13.4%) | 6.82 |

# Appendix D: Test results of different diameter of shaft

To analyze the effect of the foundation shaft diameter on the uplift bearing capacity, 4 centrifuge model experiments were conducted by changing the foundation shaft diameter as shown in Fig D1.

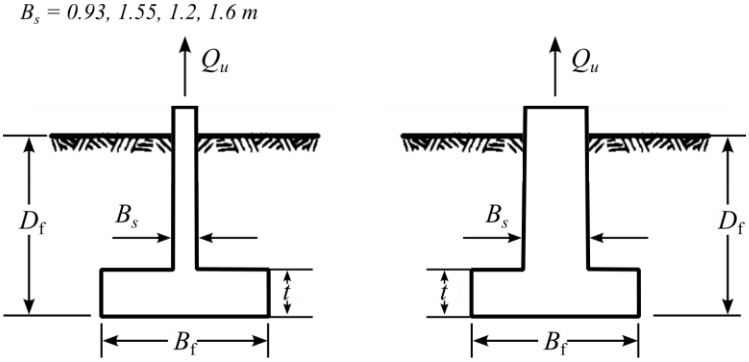

Fig. D1 Schematic diagram of tests for different diameter of foundation shaft.

The foundation widths were 3.5 and 4.5m, the embedment depth ratio was 1.0, and the foundation shaft diameter ratios ($B_s/B_f$) were 0.27, 0.35, and 0.44 to make the experiments comparable. The load-displacement curves obtained from the centrifuge model experiments were plotted in Fig. D2 according to the foundation width and foundation shaft diameter.

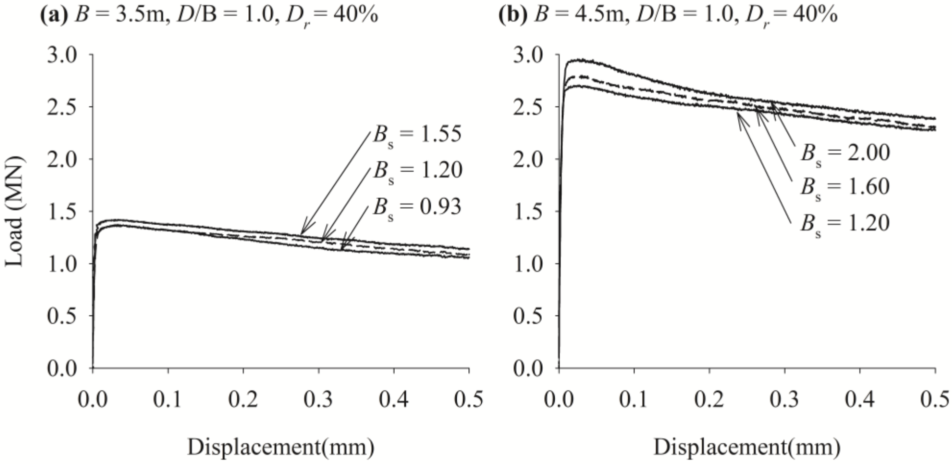

Fig. D2 Load-displacement curves with different diameter of shafts including Case 4 and 7.

The results of the two experiments, Case 3 and 7, have been added to Fig. D2 in order to demonstrate the variation in uplift resistance with regards to the foundation shaft diameter ratios. The results indicate a slight increase in uplift resistance as the foundation shaft diameter ratio increases, however, there is minimal change. It is believed that the diameter of the shaft can be disregarded in its impact on uplift resistance within the range of foundation shaft diameter ratios from 0.26 to 0.44.

To analyze the change in uplift bearing capacity and peak displacement with respect to the foundation shaft diameter ratios, Figs. D3 and D4 has been plotted. The peak displacement shows a slight increase with changes in the column diameter, but further experiments are required for a more thorough analysis of the peak displacement with respect to the foundation shaft diameter ratios. However, it can be seen that the peak displacement increases significantly as the embedment depth ratio increases, even with the same foundation dimensions and the peak displacement is affected more by the embedment depth ratio than by the foundation shaft diameter ratios.

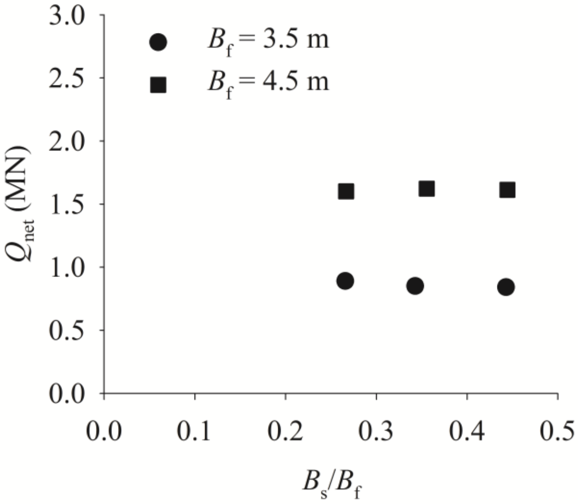

Fig. D3 net uplift bearing capacity with different foundation shaft diameter ratios.

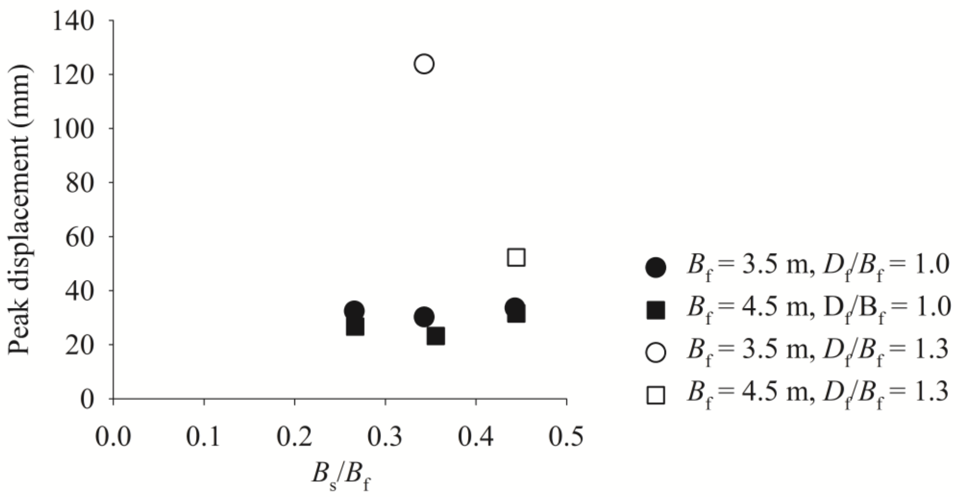

Fig. D4 peak displacement with different foundation shaft diameter ratios.

Table D1 Test results of with different foundation shaft diameter ratios.

| $B_f$ (MN) | $B_s$ (m) | $D_f/B_f$ | $Q_u$ (MN) | $Q_{net}$ (MN) | $w_p$ (mm) |
|---|---|---|---|---|---|
| 3.5 | 0.93 | 1.0 | 1.37 | 0.89 | 32.4 |
| 3.5 | 1.55 | 1.0 | 1.42 | 0.84 | 33.5 |
| 4.5 | 1.2 | 1.0 | 2.70 | 1.60 | 26.7 |
| 3.5 | 1.6 | 1.0 | 2.80 | 1.62 | 23.2 |

# 초 록

**구교영**

**건설환경공학부**

**서울대학교 대학원**

송전 철탑을 지지하는 얕은 확대기초는 풍하중, 송전선의 단선 등의 이유로 인발하중을 받게 된다. 그리고 얕은기초의 인발지지력은 압축지지력에 비해 안전율의 여유가 크지 않으므로, 정확한 인발지지력 산정을 위한 연구가 중요하다. 그러므로, 본 연구에서는 다양한 정적 원심모형실험과 머신 러닝 기법을 이용한 기호 회기 분석을 수행하여 모래지반에 설치된 기초의 인발거동 및 인발파괴 메커니즘을 분석하였다.

국내의 송전 철탑은 주로 산지에 설치되고 접근성 및 시공성을 고려하여 얕은기초가 주로 적용되고 있다. 실제 시공조건을 고려하여 수평 모래지반에 얕게 근입된 기초조건에 대해 연구하였다. 기초 크기, 지반의 밀도 등을 변화시키며 다양한 조건의 전단면 기초를 이용한 원심모형실험을 수행하였다. 실험결과 기초가 인발하중을 받으면, 극한하중에 상대적으로

작은 인발변위에도 극한하중에 도달하게 되며, 극한하중 이후에 하중연화 거동을 보인다. 또한 기초의 크기에 따라서 지지력 및 인발변위가 크기효과를 받는 것을 확인하였으며, 근입비 및 지반밀도가 증가함에 따라서 인발지지력이 증가하였다. 인발에 따른 지표면 상승변위를 측정하여 분석하고 지반 내부마찰각을 이용하여 영향범위를 제안하였다.

이러한 인발지지 거동 특성을 분석하기 위하여, 반단면 조건의 원심모형실험을 수행하여 지반 내부의 파괴 메커니즘을 분석하였다. 반단면 기초의 지표면과 전단면 기초의 상승변위와 비교하여 두 실험조건이 동일한 인발거동을 갖는다고 판단하였다. PIV기법을 이용하여 기초 인발에 따른 지반의 전단 변형률 발현을 고려하여 지반의 파괴면을 분석하고, 두 직선형태의 파괴면을 제안하였다. 머신러닝 기법을 이용한 기호회기 분석법을 이용하여 기초 크기 지반 내부마찰각에 따른 파괴면을 제안하였다.

최종적으로, 전단면 및 반단면 원심모형실험 결과로부터 한계 평형 해석법을 적용한 인발지지력 산정식을 제안하였다. 파괴면에 작용하는 전단력은 절편법을 이용하여 산정하였다. 제안된 이론식은 본 연구에서 수행한 원심모형실험과 다른 연구자들에 의해 수행된 인발실험 결과를 이용하여 비교 검증하였다. 비교결과 기초 크기 및 지반 강도를 잘 반영하여, 지지력 잘 예측을 하는 것으로 나타났다. 본 연구의 결과를 통해 제안된 얕은기초의 인발지지력 산정식으로 기초의 인발하중지지 설계에

참고자료로서 이용될 것으로 판단된다.

**주요어:** 송전철탑 기초; 인발지지력; 원심모형실험; 파괴면; 전단저항력

**학 번:** 2018-34756

# 감사의 글

대학원에 입학해서 박사과정을 시작한지 엊그제 같은데, 이 글을 쓰고 있으니 감회가 새롭습니다. 지난 시기 동안 생각치도 못한 많은 발전을 이룰 수 있어서 제 인생에 큰 기쁨이었고 많은 도움을 받을 수 있어 행복했습니다.

이 논문을 쓸 수 있도록 많은 지원과 도움을 주신 교수님들과 선·후배 여러분께 깊이 감사드립니다.

제 실수를 많이 이해해주시고 기다려 주신 김성렬 교수님께 정말 감사드립니다. 그리고 부족한 저를 지도해주시고 어떻게 공부해야 하는지 가르쳐 주신 교수님 은혜에 보답할 수 있도록 항상 열심히 노력하겠습니다. 언제나 자상하게 말씀주시고 지도해주신 정충기 교수님께 감사드립니다. 그리고 항상 웃는 모습으로 제자를 지도해주신 박준범 교수님께도 감사드립니다. 그리고 바쁘신 와중에도 더 나은 논문이 될 수 있도록 세심하게 심사해주시고 지도해주신 김현기 교수님, 김재현 교수님께 감사드립니다.

같이 가장 많이 고생한 경선이, 재인이에게 따뜻하게 말한마디 잘 못하고 일만 시켜 미안한 말을 먼저하고 싶고, 같이 일하고 연구할 수 있어서 정말 좋은 시간이었고, 감사한 마음 전합니다. 부족한 선배때문에 고생 많았는데, 앞으로 두 사람 앞날에 좋은 일만 가득하길 바랍니다.

박사 입학할 때부터 많이 챙겨주신 선배님들께 감사드립니다. 항상 제 말에 귀기울여 주시고 항상 진심으로 대해주신 희준이형, 후배 잘 되도록 항상 좋은 말씀해주신 태영이형, 어떤 상황에서도 우뚝 서있어 언제든 기댈 수 있었던 승환이형, 처음 왔을 때 같이 실험하고 적응하는데 정말 많은 도움 주신 성하형과 규범이, 그리고 늘 관심 가져 주시고 조언해주신 민기형에게 감사인사 드립니다.

연구실에서 가장 많은 도움을 준 트란에게 정말 큰 감사의 말을 전하고 싶습니다. 트란의 도움이 없었다면, 정말 상상조차 할 수 없었던 연구실 생활이었을 텐데 많이 도와줘서 감사드립니다. 베트남에 돌아가서 부모님과 좋은 시간 보내고 하고자 하는 일 잘되길 바랍니다. 연구실에 같이 입학해서 처음엔 탈도 많았지만 서로 의지하고 연구실 이끌어 가서 좋았던 병수, 일이 생기면 항상 믿고 맡기던 성호, 병윤이에게 많이 못챙겨줘 미안하고 앞으로 잘 챙겨줄 수 있도록 노력할게! 많이 토의하고 의견나누고 의지했던 범희형, 믿는 구석 인현, 재규, 태훈이에게 덕분에 즐겁게 학교다닐 수 있어서 감사드립니다. 같이 졸업하는 영우와 라힘에게도 앞으로의 인생을 응원합니다! 멋진 후배 정현, 택규, 석준, 부, 준우, 아니스, 형석에게도 감사드립니다. 일본에서 와서 적응하는데 고생한 기안, 앞으로 행복하고 좋은 일 가득하고 건강하게 지내!

제가 잘될 수 있도록 도움되는 말씀과 사랑을 주신 우리 엄마 아빠 감사드립니다. 가까이 있어도 잘 못챙겨줬던 누나 매형께도 도움주셔서 감사드립니다. 우리 조카들 지우, 준영, 하진도 아프지 않고 밝게 자라길 바래. 마지막으로, 항상 물심양면으로 손자 잘 되도록 도와주신 할아버지 할머니에게 이 논문을 바칩니다. 사랑하는 할아버지 하늘에서 편히 쉬시길 바라고 할머니 항상 건강하시길 바랍니다.